A Transfer Matrix Approach to Studying the Entanglement Complexity of Self-Avoiding Polygons in Lattice Tubes

A Thesis Submitted to the
College of Graduate and Postdoctoral Studies
in Partial Fulfillment of the Requirements
for the degree of Doctor of Philosophy
in the Department of Mathematics and Statistics
University of Saskatchewan
Saskatoon

By

Jeremy Eng

Permission to Use

In presenting this thesis in partial fulfilment of the requirements for a Postgraduate degree from the University of Saskatchewan, I agree that the Libraries of this University may make it freely available for inspection. I further agree that permission for copying of this thesis in any manner, in whole or in part, for scholarly purposes may be granted by the professor or professors who supervised my thesis work or, in their absence, by the Head of the Department or the Dean of the College in which my thesis work was done. It is understood that any copying or publication or use of this thesis or parts thereof for financial gain shall not be allowed without my written permission. It is also understood that due recognition shall be given to me and to the University of Saskatchewan in any scholarly use which may be made of any material in my thesis.

Requests for permission to copy or to make other use of material in this thesis in whole or part should be addressed to:

Head of the Department of Mathematics and Statistics
142 McLean Hall, 106 Wiggins Road
University of Saskatchewan
Saskatoon, Saskatchewan
Canada
S7N 5E6

Or

Dean of the College of Graduate and Postdoctoral Studies
116 Thorvaldson Building, 110 Science Place
University of Saskatchewan
Saskatoon, Saskatchewan
Canada
S7N 5C9

Abstract

Self-avoiding polygons (SAPs) are a well-established useful model of ring polymers and they have also proved useful for addressing DNA topology questions. Motivated by exploring the effects of confinement on DNA topology, in this thesis, SAPs are confined to a tubular sublattice of the simple cubic lattice. Transfer matrix methods are applied to examine the entanglement complexity of SAPs in lattice tubes. Transfer matrices are generated for small tube sizes, and exact enumeration of knotting distributions are obtained for small SAP sizes. Also, a novel sampling procedure that utilizes the generated transfer matrices is implemented to obtain independent uniformly distributed random samples of large SAPs in tubes. Using these randomly generated polygons, asymptotic growth rates for the number of fixed knot-type SAPs are estimated, and evidence is provided to support a conjectured asymptotic form for the growth of the number of fixed knot-type polygons of a given size. In particular, the evidence supports that the entropic critical exponent goes up by one with each knot factor.

Additionally, a system consisting of two SAPs (called a 2SAP) in a tube is also studied to explore linking. New transfer matrices are generated for 2SAPs in small tube sizes, and exact enumeration of linking distributions are obtained for small 2SAP sizes. A sampling procedure similar to that developed for SAPs is implemented by using the 2SAP transfer matrices to obtain independent uniform samples of large 2SAPs in tubes. An asymptotic form for the number of fixed link-type 2SAPs is conjectured with some supporting evidence from the sampled 2SAPs.

All the evidence obtained supports the conclusion that the knotted parts in long polymers confined to tubular environments occur in a relatively localized manner. This is supported by the entropic critical exponent results, and by preliminary evidence that average spans of knot factor patterns are not growing significantly with polygon size. Similar evidence is obtained for the knotted parts in 2SAPs. The SAP study has also revealed further characteristics of knotting in tubes. For example, when the cross-sectional area of tubes are equal, evidence indicates that knotting is more likely in more symmetrical tubes as opposed to flatter tubes. Additionally, two types of knot pattern modes have been observed and strong evidence is provided that the so-called non-local mode is dominant for small tube sizes. These two modes

have also been observed in non-equilibrium simulations and in DNA nanopore experiments. The evidence for the characteristics of the linked part of 2SAPs in a tube is less conclusive but its study has opened up numerous interesting questions for further study.

In summary, the novelty of the contributions in the thesis include both computational and polymer modelling contributions. Computationally: transfer matrices, Monte Carlo methods, and a novel approach for knot identification for knots in tubes are developed and extended to larger tube sizes than ever before. Polymer modelling: strong numerical evidence supporting knot localization for polymers in tubes and the first evidence regarding characterising linking for polymers in tubes are obtained.

Acknowledgements

I would like to express my deepest gratitude towards my supervisor Dr. Chris Soteros for her expertise, unwavering support, and invaluable advice. I am so grateful to have had such a patient, understanding, and encouraging mentor during my Ph.D. journey. I would also like to thank my examining committee, Dr. Juxin Liu, Dr. Raj Srinivasan, Dr. Richard Bowles, and Dr. Andrew Rechnitzer, for taking the time to read my thesis and for their helpful suggestions and comments. Thank you to Dr. Nicholas Beaton for sharing his knowledge and his computer code, and thank you to Dr. Koya Shimokawa for his knot-theory expertise and for hosting me in Japan. To my friends Matthew Schmirler and Marla Cheston, thank you for your friendship and all of your help throughout the years. I also extend my thanks to Nicole Zolkavich and Rylan Smith for their contributions towards the results in this thesis.

I would like to acknowledge Compute Canada for the use of their high-performance computing network, and I would like to thank Rob Scharein for the use of his program Knotplot. Thanks to the Department of Mathematics and Statistics for their support over the years, and thank you to the Nutrien Kamskenow Science Outreach Program for not only their funding, but also for providing me the unique opportunity to lead fun, hands-on science activities for community school students. Last but not least, I would like to thank my family; my wife Elyse, my parents Bill and Pauline, and my sister Brittani; for always being there with unconditional and loving support.

Contents

List of Tables

List of Figures

1 INTRODUCTION

The focus of this thesis is on the examination of the entanglement complexity (knotting and linking) of lattice models of ring polymers under confinement. Knots and links are important in many areas of polymer physics and biology, as knotting and linking can significantly affect a polymer's properties and behaviour [41]. Consequently, there has been much interest and research on this topic through rigorous approaches, computational simulations, and laboratory experiments (see [39] for a review on DNA knotting). Several different useful models have been used by researchers to model ring polymers, such as lattice polygons, equilateral polygons, gaussian polygons, and wormlike chains (see [41] for a review). This thesis will focus on lattice polygon models of ring polymers; in particular, self-avoiding polygons (referred to as SAPs or just polygons) on the simple cubic lattice ($\mathbb{Z}^3$). SAPs were first introduced by Orr (1947) [42] and Flory (1949) [22] and are now the standard lattice model of ring polymers [60]. Lattice polygons have been a useful model for studying the entanglement of polymers. In the early 1960's, Frisch, Wasserman [23], and Delbruck [18] conjectured that sufficiently long ring polymers have a high probability of being knotted. This is known as the FWD conjecture. This conjecture was proven in 1988, when Sumners and Whittington [60] and independently Pippenger [43] proved it for a lattice polygon model.

Polymers are typically subject to spatial constraints [34]. For example, biopolymers such as DNA can be around 1 m long, but must fit inside a cell nucleus that has a diameter of approximately 10 μm [34]. Additionally, bacteriophage capsids, which are less than a micrometer in size, have been shown through experiments to contain DNA in a structured form, which up extraction form complex knots [35]. Also, driven translocation (movement) of DNA through solid state nanopores is used to sequence DNA [78], detect folded configurations[25], and unzip double-stranded DNA [47]. Confinement affects the conformational and physical properties of polymers, such as their entanglement complexity [38].

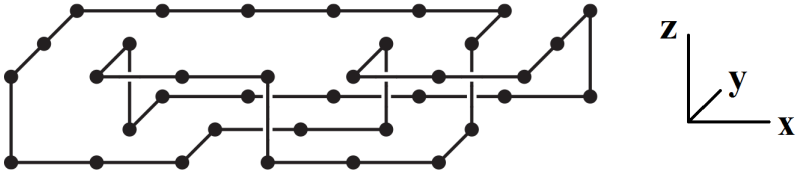

Figure 1.1: An example of a SAP confined in a $2 \times 1 \times \infty$ tube.

To model the confinement of polymers, there have been a variety of different models which have been studied; some with full confinement (sphere or box) or partial confinement (wedges, slabs, or tubes) (see [36, 39, 41, 67] for reviews). In this thesis, we restrict SAPs to a tubular sublattice of $\mathbb{Z}^3$, where the polygon is confined in two of the dimensions, but unconfined in the third dimension. See Figure 1.1 for an example of a polygon in $\mathbb{Z}^3$ confined to a $\infty \times 2 \times 1$ (2×1 for short) tube.

By constraining SAPs to a tube, the SAP can essentially only "grow" in one direction. This one-dimensional growth allows for the application of transfer matrix methods (reviewed in Section 2.3). The work in this thesis builds upon previous work from my Master's thesis [20], where exact results were obtained via transfer matrices for $L \times 1, L \leq 3$ tubes. As part of this Ph.D. thesis work, joint work with Beaton and Soteros [12], I extended my Master's results on knotting statistics to larger sized polygons in $L \times 1, L \leq 3$ tubes. Additionally, these larger SAPs were also used to examine the "localization" of knots in SAPs in tubes, and these results were published in [10]. This thesis also presents new transfer matrices for SAPs in the tube sizes: $L \times 1, L \leq 5$ and $L \times 2, L \leq 3$. These transfer matrices are used to generate SAPs in tubes, by exact enumeration and Monte Carlo methods, in order to examine knotting statistics and knot localization for SAPs in tubes. The previously published results of [12] and [10] are also updated using the transfer matrices for these additional tube sizes.

This thesis also examines the entanglement complexity (mainly linking) of two self-avoiding polygons in a tube, each with equal "span" in the x-direction (referred to as *2SAPs*). This builds on the work of Atapour et al. in [6]. Herein, novel transfer matrices are generated for 2SAPs in tube sizes $L \times 1, L \leq 4$ and 2×2. Utilizing these new transfer matrices, 2SAPs are generated through exact enumeration and Monte Carlo methods. New results regarding exact and estimated linking probabilities are obtained from these generated 2SAPs.

For both SAPs and 2SAPs, the generated transfer matrices are also used to directly calculate asymptotic properties of the numbers of SAPs and 2SAPs as their size increases to infinity. Using these results, along with generated SAPs and 2SAPs, the effect of knot-type and link-type on the asymptotics is examined. Supporting evidence is provided that the number of "factors" in a knot-type or link-type affect the knot-type or link-type's occurrence probability. Moreover, data obtained indicates that knotting occurs in a relatively localized manner, and the average spans of the "knotted factors" are not growing significantly with polygon size. Additionally, it has also been observed that the knotted factors can be classified into two different modes, and evidence indicates that the so called non-local mode is dominant for small tube sizes. These two modes have also been observed in non-equilibrium simulations [59] and in DNA nanopore experiments [44]. A better understanding of knotting and linking properties of confined SAPs and 2SAPs will lead to a better understanding of the entanglement complexity of confined polymers. This in turn could lead to better methods for knot and link detection, such as in nanopore sensing experiments [8], or an improved understanding of the topology simplification role of some enzymes acting on DNA [58].

This chapter serves as an introduction to the problems and questions that this thesis addresses. The remainder of the chapter is outlined as follows. Section 1.1 contains motivation for studying SAPs in tubes, and Section 1.2 contains details about the questions of interest that will be addressed in this thesis.

1.1 Motivation

A *polymer* is a long chain molecule consisting of a large number of repeated units (called monomers), which are held together by chemical bonds [71]. In dilute solution, monomers repel each other creating an "excluded volume" around the polymer, such that a polymer chain cannot intersect itself. A sufficiently long polymer can be self-entangled, and in the case of ring polymers (closed polymers) this entanglement can be trapped as a "knot", resulting in a knotted ring polymer. Similarly, two ring polymers can be mutually entangled, and this entanglement can be trapped in the form of a "link".

Knots and links are an important topic in polymer physics and biology. For example, on a

macroscopic scale, deoxyribonucleic acid (DNA) is a polymer, where the polymer's monomers can correspond to the DNA's base pairs. Entanglements in DNA can affect the efficiency of cellular processes such as replication and transcription [72]. In order for a bacterial cell to survive, its circular DNA must be replicated. However, if the DNA is knotted, then the two "daughter" molecules of the replication will be linked, and the cell cannot divide properly and will die [14]. The cell solves this problem via enzymes such as topoisomerases which act on the DNA by cutting it and performing local strand change operations [46]. Understanding how these enzymes perform this topology simplification so efficiently is an important open problem.

DNA molecules are typically enormously long and the probability of knotting in long polymers is expected to be high [41]. High knotting probability has been observed and proven in models of polymers. Examining the knotting probability of DNA has also been done experimentally. Shaw and Wang [51, 52] and Rybenkov et al. [45] took DNA molecules of different lengths (in different solutions) and determined their equilibrium knotting probability after ring closure. This is perhaps the most direct measurement of knotting probability that has been performed on DNA [41]. More recently, solid-state nanopores have been used to directly observe knots in DNA molecules of arbitrary length [44].

As mentioned earlier, polymers are typically subject to spatial constraints [34]. Circular bacterial DNA, which is about 1 mm long, is held inside cells whose size are about 1-2 μm in diameter [34]. Confinement affects the conformational and physical properties of polymers, such as their entanglement complexity [38]. The highest level of confinement occurs in viruses. DNA molecules confined to viral capsids (the shell of a virus) have a very high probability of being knotted and the distribution of "knot-types" (to be defined later in Section 2.4) is different from the knot distribution for free DNA in solution [3, 37]. Additionally, it is believed that knotting in unconfined polymers is quite "localized", while knotting in confined polymers appears to be more "non-local" [36]. Here, local knotting of a polymer chain refers to when the size of the knotted part of the chain is small relative to the whole length of the chain (See Section 3.5 for more details on this classification).

Recently there has been much interest involving the behaviour of polymers as they translocate through a nanopore or nanochannel. Such examples include DNA being packed in a viral

capsid [37], the transport of biopolymers through cell membranes [75], and driven translocation to examine polymer properties [78]. Simulations have been done to study knotting and other properties of polymers in nanochannels [38], as well as simulations of translocating links through nanopores [15]. Confining a polygon in a narrow tube, such as is done in this thesis, models the narrow confinement conditions a polymer experiences while in a nanopore or nanochannel. Motivated by these topics, this thesis addresses relevant questions of interest which arise when discussing polymers under confinement conditions. The goal is to better characterize the nature of the knotting and linking towards an improved understanding of experiments such as DNA in nanopores or enzyme-DNA interactions.

1.2 Questions of Interest

The overall goal of this thesis is to apply transfer matrix methods to SAPs in tubes in order to better understand the entanglement complexity of polymers under confinement. There are a variety of questions involving the entanglement complexity of polymers that are investigated in this thesis.

One main question of interest, inspired by the FWD conjecture, is how does a random polymer's knot distribution change as the size of the polymer varies, or as the confinement conditions change. Here we assume in the SAP model that every SAP in a tube with the same "size" is equally likely, and we examine how the knot distribution changes as the size of the SAP varies, or as the size of the confining tube varies. Calculating these knot distributions involves counting the number of SAPs of each knot-type (of a certain size); however, just counting SAPs by size (ignoring knot-type) is a very difficult problem. Currently, the best algorithms require exponential time and barely reach knotted configurations [16]. This exponential complexity limits the sizes where exact results can be obtained. This thesis addresses the knot distribution question for SAPs in lattice tubes by generating SAPs through exact enumeration (for small sizes) and Monte Carlo methods (for larger sizes).

SAPs are generated efficiently by utilizing transfer matrices. Transfer matrices are the main tool used by this thesis to examine entanglement complexity. Transfer matrices for small tube sizes were generated for my Master's Thesis [20]; for this PhD thesis, transfer

matrices for larger tube sizes have been generated by increasing the efficiency of the creation process and memory storage of the transfer matrices. More details on this process are given in Section 3.2.

For small SAP sizes, in small tubes, the knotting distribution question is addressed by exact enumeration, where the knot distribution is calculated exactly by generating (via transfer matrices) all SAPs of a certain small size. These generated SAPs then have their knot-type identified via the software Knotplot [49], which uses a knot invariant called the "HOMFLY polynomial" (discussed further in Section 2.4.3). This results in exact counts for SAPs by their size and knot-type, and the knot distribution is determined exactly for these small sizes. However, this exact enumeration process is limited by its computational complexity [28], as the number of SAPs increases exponentially with their size. This exact enumeration task is presented in Section 3.3.

For larger SAP sizes (but still small tube sizes), where exact enumeration is not feasible (due to computational restrictions), a Monte Carlo approach [12] is used to estimate the knotting distribution. Utilizing transfer matrix theory again, uniform samples of SAPs in tubes are generated via a sampling method that utilizes transition probabilities which are obtained from the transfer matrices. The knot-types of these samples are then identified and an estimate of the knot distribution is obtained. This process is covered in Section 3.4.

As mentioned earlier, polymers are typically very long molecules, and very long ring polymers can be modelled by very long SAPs. This thesis will also examine the asymptotic growth (size $\to \infty$) of the number of SAPs in tubes, as well as the asymptotic growth of the number of SAPs with a fixed knot-type. It is of interest to study how these growth rates vary according to knot-type. In this thesis, evidence is provided to support the conjecture that in a tube $\mathbb{T}$, the number of n-edge polygons with knot-type K ($p_{\mathbb{T},n}(K)$) has the asymptotic form:

$$p_{\mathbb{T},n}(K) \sim C_{\mathbb{T},K} n^{f_K} \mu_{\mathbb{T},0_1}^n \qquad \text{as} \quad n \to \infty, \tag{1.1}$$

where f_K is the number of "prime knot factors" and $\mu_{\mathbb{T},0_1}$ is the "growth constant" for unknotted polygons (0_1 represents the unknot). The exponent on n (f_K here) is called the *entropic critical exponent*. Note that in this thesis, for any two quantities $a(y), b(y)$ that

depend on some value y, we write $a(y) \sim b(y)$ as $y \to \infty$ if and only if $\lim_{y\to\infty} \frac{b(y)}{a(y)} = 1$.

This conjecture is consistent with what is believed to hold for unconfined SAPs [68]. It was proven by Soteros and Whittington [55] that the number of unknotted polygons in a tube grows at an exponential rate which is less than the exponential growth rate of the number of all SAPs in a tube ($\mu_{\mathbb{T},K} < \mu_{\mathbb{T}}$). This proves the FWD conjecture for polygons in tubes. It has been recently proven by Atapour et al. [5] that when $\mathbb{T}$ is the 2×1 tube, the growth rate of a fixed knot-type K is equal to that of the unknot ($\mu_{2\times1,K} = \mu_{2\times1,0_1}$). This is the first model where this aspect of the conjecture has been proven. In this thesis, the growth rates associated with these fixed knot-type SAPs are examined numerically via Monte Carlo methods; this gives an idea of how the knotting distribution changes as the size of the polymers get very large. It is also examined how the number of "factors" in a knot-type affect its knotting probability. The Monte Carlo evidence is presented in Section 3.4, and it strongly supports the conjectured form.

Lastly, this thesis examines the entanglement complexity for systems of two self-avoiding polygons (called 2SAPs). Equivalent questions to those that are asked above regarding the knotting of SAPs are asked for the linking of 2SAPs. New 2SAP transfer matrices are generated (Section 4.1), exact linking distributions are calculated (Section 4.3), and Monte Carlo results (Section 4.5) are obtained for 2SAPs.

To summarize, this thesis addresses each of the following questions for SAPs and 2SAPs in tubes:

- What is the exact knotting/linking distribution for small sized SAPs/2SAPs (in small tube sizes)?
- What are estimates of the knotting/linking distribution for large sized SAPs/2SAPs (in small tube sizes)?
- How does the knotting/linking distribution of SAPs/2SAPs change as the size of the SAPs/2SAPs change, or the size of the tube changes?
- What is the form of the asymptotic growth rate for the number of SAPs/2SAPs?
- What is the form of the asymptotic growth rate for the number of SAPs/2SAPs with a fixed knot/link-type?

- What constants in these asymptotic growth rates can be estimated by using transfer matrix and Monte Carlo methods?
- When confined to a narrow tube, how "localized" is the knotting or linking?

In terms of results in this thesis, exact knotting and linking distributions are calculated for small tube sizes and small spans (Tables 3.3, 3.4, 4.3, and 4.4). For larger spans, estimates for the knotting and linking distributions are calculated via Monte Carlo techniques, and they are summarized in Tables C.1, C.2, C.3, C.4. It is determined that as SAPs/2SAPs become larger, they are more likely to be knotted/linked. It is also discovered that when two tubes' cross-sections have the same number of vertices (e.g. 5×1 and 3×2), knotting is more common in the less narrow confinement (i.e. 3×2). The exponential growth rates for the number of SAPs and 2SAPs are calculated for small tube sizes from their transfer matrices and are presented in Tables 3.1 and 4.2. Conjectured asymptotic growth rates for the number of fixed knot-type SAPs (Section 3.4) and fixed link-type 2SAPs (Section 4.5) are presented, along with supporting evidence. It is also observed that two different modes of knot patterns occur (local and non-local), and strong evidence is provided that the non-local mode is dominant for small tube sizes. Additionally, results indicate that the average spans of the knot patterns do not increase significantly with polygon size.

In summary, the novelty of the contributions in the thesis include both computational and polymer modelling contributions. Computationally: transfer matrices, Monte Carlo methods, and a novel approach for knot identification for knots in tubes are developed and extended to larger tube sizes than ever before. Polymer modelling: strong numerical evidence supporting knot localization for polymers in tubes and the first evidence regarding characterising linking for polymers in tubes are obtained.

The remainder of this thesis is structured as follows. Chapter 2 contains relevant background information required to understand the work done in this thesis. This includes main definitions (Section 2.1), modelling polymers using statistical mechanics (Section 2.2), transfer matrix methods (Section 2.3), and basic knot theory (Section 2.4). Chapter 3 contains work done regarding self-avoiding polygons. This includes the model (Section 3.1), creating transfer matrices for larger tube sizes (Section 3.2), exact results (Section 3.3), and Monte Carlo results (Sections 3.4 and 3.5). Chapter 4 contains work done regarding systems of

two self-avoiding polygons. This includes creating new 2SAP transfer matrices (Section 4.1), calculating exponential growth rates of 2SAPs (Section 4.2), determining exact linking distribution and linking number results (Section 4.3), discussing the growth rates of some different types of 2SAPs, 4.4, and supporting evidence from the Monte Carlo results (Section 4.5). Lastly, Chapter 5 contains a summary of the work done in this thesis, conclusions, and potential future work.

2 BACKGROUND INFORMATION

In this chapter, background information relevant to this thesis is presented. First, the main definitions that are used throughout this document are presented. Second, the main ingredients in a polymer model are introduced, and some self-avoiding polygon models are discussed. Third, it is reviewed how the transfer matrix can be applied to SAPs in tubes, and how transfer matrices can be used to: obtain counts of SAPs; obtain growth rates; generate all SAPs; and obtain transition probabilities for generating random samples of SAPs. The Monte Carlo method used to obtain independent, uniform, random samples of polygons by utilizing transfer matrices is also explained. Lastly, some basic knot theory is presented which defines mathematical knots and links, as well as knot- and link-types.

2.1 Main Definitions

Unless stated otherwise, the definitions in this chapter are from [54]. This notation is considered standard for lattice models of polymers.

Definition 2.1.1 (Simple cubic lattice [7])**.** The *simple cubic lattice* is defined to be the infinite graph embedded in $\mathbb{R}^3$ with vertex set $\mathbb{Z}^3$ and edge set $\{\{u, v\} | u, v \in \mathbb{Z}^3, ||u-v|| = 1\}$, where $|| \cdot ||$ is the Euclidean norm.

Depending on the context, $\mathbb{Z}^3$ will be used to represent either the simple cubic lattice or its vertex set. Similarly for V, a set of vertices in $\mathbb{Z}^3$, V will be used to represent either the vertex set V or the subgraph of $\mathbb{Z}^3$ induced by this vertex set. That is, V may represent the subgraph with vertex set V and edge set $\{\{u, v\} | u, v \in V, ||u - v|| = 1\}$.

Definition 2.1.2. An n-edge *self-avoiding polygon* (SAP) in $\mathbb{Z}^3$ consists of a set of n distinct lattice edges $\{u_0, u_1\}, \{u_1, u_2\}, \ldots, \{u_{n-2}, u_{n-1}\}, \{u_{n-1}, u_0\}$ and a corresponding set of n distinct lattice vertices $\{u_0, u_1, \ldots, u_{n-1}\}$, such that the vertices $u_i \in \mathbb{Z}^3$ for $i = 0, \ldots, n-1$.

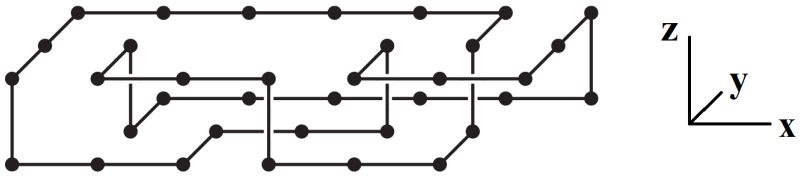

Figure 2.1: An example of a SAP in a tube. This SAP is in the 2×1 tube, has 36 edges, and has a span of 6.

A SAP is called "self-avoiding" because it it does not intersect itself (i.e. each vertex has degree two). It is assumed a SAP has at least 4 edges. See Figure 2.1 for an example of a SAP.

Definition 2.1.3. The *length* of a SAP ω is the number of edges (or vertices) in ω, denoted by $|\omega|$.

Note that the length of a SAP n must be even, and thus n is assumed to be even when discussing SAPs. This includes limits, where for example $\lim_{n\to\infty}$ should be interpreted as a limit through even values of n only (when referring to SAPs). This thesis will mainly be focussed on studying SAPs that are confined to lattice tubes. We will call these tubes $L \times M$ tubes as defined next:

Definition 2.1.4. For non-negative integers L, M, an $L \times M$ *tube* is defined to be the sublattice of $\mathbb{Z}^3$ induced by the vertex set $\{(x, y, z) \in \mathbb{Z}^3 | x \geq 0, 0 \leq y \leq L, 0 \leq z \leq M\}$.

See Figure 2.1 for an example of a SAP in an $L \times M$ tube with $L = 2$ and $M = 1$. We will assume that a SAP in $\mathbb{T}$ occupies at least one edge in the plane $x = 0$, and we will assume without loss of generality that $L \geq M$. Also, we will use the symbol $\mathbb{T}_{L\times M}$ to represent the $L \times M$ tube, or just $\mathbb{T}$ when the dimensions are fixed.

Definition 2.1.5. The *span* s of a SAP in an $L \times M$ tube is defined to be the maximal x-coordinate reached by any of its vertices.

See Figure 2.1 for a SAP with span 6. Lastly, we are also interested in the subset of SAPs in $\mathbb{T}$ which occupy every vertex in a $s \times L \times M$ box. We call these SAPs *Hamiltonian SAPs*.

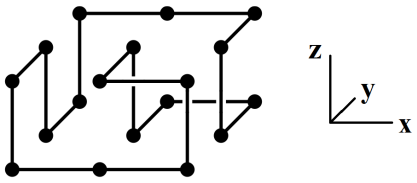

Figure 2.2: An example of a Hamiltonian SAP, which occupies every vertex in a $2 \times 2 \times 1$ box. This Hamiltonian SAP is in the 2×1 tube and has a span of 2.

Definition 2.1.6. A span-s *Hamiltonian SAP* in an $L \times M$ tube is a SAP that occupies every vertex in an $s \times L \times M$ subtube of $\mathbb{T}$.

See Figure 2.2 for an example of a Hamiltonian SAP.

2.2 Modelling Polymers in a Dilute Solution using Statistical Mechanics

In this section, three main ingredients to a statistical mechanics model of a polymer in dilute solution will be presented (based on [64]). It is also explained how self-avoiding polygons (SAPs) on the simple cubic lattice ($\mathbb{Z}^3$) (and SAPs confined to lattice tubes) fit into this statistical mechanics framework. The overall goal of using a statistical mechanics model is to derive average macroscopic polymer solution properties, by ensuring the model follows the laws which govern the behavior of the individual parts [64]. In the case of this thesis, we are interested in examining the average entanglement complexity of confined polymers in solution.

2.2.1 Ingredients for Modelling a Polymer in Dilute Solution

The focus is on modelling polymers in a dilute solution; that is we are considering a polymer solution which consists of polymer molecules dissolved in a solution made of solvent molecules, but where the concentration of polymers in the solution is sufficiently low, such that it is highly unlikely that two different polymer molecules will interact.

For a statistical mechanics model of a polymer solution, one first needs to define the set

Γ of all possible "conformations" of the polymer solution. Note that these conformations include both the polymer molecules as well as the solvent molecules. For the dilute solution case, one assumes that an individual polymer in the solution is isolated from the others and that a "conformation" $S \in \Gamma$ of the solution can be described in terms of the specific "configuration" of the individual polymer, relative to its surrounding solvent molecules. That is, essentially the solution consists of a single polymer molecule interacting only with itself and nearby solvent molecules. Thus, the size of the system is assumed to be determined by the "size" of the single polymer. Note that, depending on the model, Γ could be a continuous or discrete state space. For the case of interest in this thesis, SAPs in $\mathbb{Z}^3$ are used to model the configurations of ring polymers, and thus, Γ is discrete.

Secondly, each element $S \in \Gamma$ has a potential energy associated with it. This is determined by a *Hamiltonian* function, denoted by $\mathcal{H}(S)$. This Hamiltonian should reflect the underlying physics of the system. For model SAPs in $\mathbb{Z}^3$, many useful Hamiltonians can be chosen. Some examples are given shortly in Sections 2.2.2 and 2.2.3.

Finally, there is an equilibrium distribution (denoted $\mathbb{P}$) for the conformations in Γ, based on the Hamiltonian $\mathcal{H}$. If Γ is continuous, then $\mathbb{P}$ is a probability density function; if Γ is discrete, then $\mathbb{P}$ is a probability mass function. Since this thesis will be dealing with model SAPs in $\mathbb{Z}^3$, let us focus for simplicity's sake on the case where Γ is discrete. Thus, if $\Gamma = \{S_1, S_2, \ldots\}$ is a discrete state space, then the equilibrium distribution is a vector $\mathbb{P} = [\mathbb{P}(S_1), \mathbb{P}(S_2), \ldots]$, where $\mathbb{P}(S_i)$ is the probability of conformation S_i (which is based on $\mathcal{H}$) at equilibrium.

In statistical mechanics, the assumed equilibrium distribution for a conformation $S_i \in \Gamma$, is given by [64]:

$$\mathbb{P}(S_i) = \frac{e^{-\beta \mathcal{H}(S_i)}}{\sum_j e^{-\beta \mathcal{H}(S_j)}}, \tag{2.1}$$

where the distribution depends on the Hamiltonian $\mathcal{H}$ and the absolute temperature T through $\beta = \dfrac{1}{k_b T}$ (k_b is the Boltzmann constant). This distribution is referred to as the *Boltzmann distribution* or *Gibbs distribution*, and the denominator is the canonical partition function. Note that the probability of a conformation S is proportional to $e^{\frac{-\mathcal{H}(S)}{k_b T}}$.

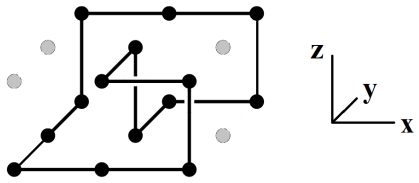

Figure 2.3: An example of a SAP which models a polymer solution. The SAP represents the configuration of the polymer, and the unoccupied vertices represent solvent molecules.

2.2.2 Modelling a Polymer in Dilute Solution as a SAP in $\mathbb{Z}^3$

As stated previously, this thesis uses SAPs in $\mathbb{Z}^3$ to model dilute polymer solution conformations; more specifically dilute ring polymer solution conformations. In this case, the standard measure used for the size of the system is to use the number of edges in a SAP. Consider the set of all n-edge SAPs in $\mathbb{Z}^3$ (up to translation). This set (call it $\mathcal{P}_n$) can be used to model the conformations of a ring polymer in dilute solution. Here, a SAP (its vertices and edges) represents the configuration of a ring polymer and empty vertices around the SAP represent solvent molecules. See Figure 2.3 for an example. This is the first ingredient in the framework for a statistical mechanics model of a polymer in dilute solution (our set of conformations Γ is $\mathcal{P}_n$ in this case).

For the second ingredient, we must define a Hamiltonian function on $\mathcal{P}_n$. As mentioned previously, there are many useful Hamiltonians that can be chosen (and have been studied), depending on which polymer questions one wishes to address. Here I will give an example of a useful Hamiltonian that has been used to model the effects of solvent quality on polymer solution properties.

A *good solvent* is effective at dissolving a polymer, and thus the polymer's monomers prefer to be surrounded by solvent molecules instead of other monomers [74]. On the contrary, in a *poor solvent* monomers are less attracted to the solvent molecules but are still dissolved. Thus, polymers in a good solvent have a greater excluded volume and are generally more "swollen" than those in a poor solvent. If solvent quality decreases from a good solvent to a poor solvent (e.g. due to a temperature drop), in very dilute and high molecular weight solutions, a collapse transition occurs [41] (called the θ temperature) to where the polymer

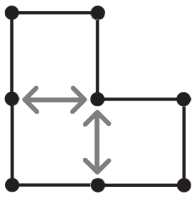

Figure 2.4: A contact occurs when two unbonded vertices are unit distance apart. Here there are two contacts, represented by grey arrows.

is very "globular" (the monomers are closer together and excluded volume reduces).

Define a *contact* in a SAP ω to occur when two unbonded vertices are unit distance apart (see Figure 2.4). The solvent quality can be modelled by using a Hamiltonian based on the number of contacts in ω, denoted by $C(\omega)$. Note that this Hamiltonian is the second ingredient in our statistical mechanics polymer model. Using this Hamiltonian and the Boltzmann distribution, the equilibrium probability of an n-edge SAP ω is then given by:

$$\mathbb{P}(\omega) = \frac{e^{C(\omega)v}}{\sum_{\omega^* \in \mathcal{P}_n} e^{C(\omega^*)v}}. \tag{2.2}$$

This probability distribution depends on the choice of v, which is a model parameter related to solvent quality [69], and its value determines the Hamiltonian and the temperature. This distribution is the final ingredient to our statistical mechanics model. Notice that a larger value of v leads to an increased probability for SAPs with more contacts; that is the model has an increased equilibrium probability for monomers to be surrounded by other monomers, instead of solvent molecules. Numerical evidence for this model indicates that a collapse transition occurs at a critical value of v, which has been estimated to be $v_c = 0.2782 \pm 0.007$ [61] for $\mathbb{Z}^3$. Note that v_c is lattice dependent. If $v > v_c$, the model is referred to as being in the *poor solvent regime*, and if $v < v_c$, the model is referred to as being in the *good solvent regime*. If $v = v_c$, the model is referred to as being in a *θ-solvent*.

When modelling polymers under the dilute solution and good solvent assumptions (using SAPs), it is standard to assume that all conformations of SAPs with the same length are equally likely [64]. This assumption is represented in the above example, by using the Hamiltonian where $v = 0$. Since various properties (e.g. radius of gyration, critical exponent) are expected to be the same for all values of v in the good solvent regime, the $v = 0$ case is

considered to be representative of this regime. When $v = 0$, the equilibrium probability of an n-edge SAP ω simplifies to

$$\mathbb{P}(\omega) = \frac{1}{\sum_{\omega^* \in \mathcal{P}_n} 1} = \frac{1}{p_n}, \tag{2.3}$$

where $p_n = |\mathcal{P}_n|$, the number of n-edge SAPs, counted up to translation. Thus, each SAP in $\mathcal{P}_n$ defines a polymer solution conformation in a good solvent, and p_n tells us the number of conformations.

2.2.3 Modelling Polymers Under Confinement

This thesis uses SAPs in $\mathbb{Z}^3$ in an $L \times M$ tube ($\mathbb{T}$) to model dilute ring polymer solution conformations with confinement. Two ways of measuring the system size are considered. For the case that size is the number of edges, the state space is the set of all n-edge SAPs in $\mathbb{T}$ which occupy at least one vertex in the plane $x = 0$ (call this set $\mathcal{P}_{\mathbb{T},n}$). A SAP in $\mathcal{P}_{\mathbb{T},n}$ represents the configuration of a ring polymer under confinement, and empty vertices represent solvent molecules. For the case that span is used for system size, the state space is the set of all span-s SAPs in $\mathbb{T}$ (call this set $\mathcal{P}_{\mathbb{T}}(s)$). When using the set $\mathcal{P}_{\mathbb{T},n}$, we will call this the *fixed-edge model*, and when using the set $\mathcal{P}_{\mathbb{T}}(s)$, we will call this the *fixed-span model*. Both of these models are used in this thesis, and more details on these two models are located in Section 3.1.2. For now, let us focus on the fixed-edge model; thus our state space (referred to previously as Γ) is $\mathcal{P}_{\mathbb{T},n}$.

One Hamiltonian that has been used, for SAPs in tubes, models an external force which acts upon a polymer (see [7, 9, 11, 13, 21, 26, 32, 66]). We assume that a force f is applied to a single ring polymer modelled by a SAP ω, which has span $s(\omega)$. We assume f acts parallel to the x-axis, perpendicular to and incident on the plane $x = s(\omega)$ (see Figure 2.5). When $f > 0$, the force is a stretching force, and when $f < 0$, the force is a compressing force. Thus, the equilibrium probability of a SAP ω with span $s(\omega)$ in a tube $\mathbb{T}$ subject to a force f is given by

$$\mathbb{P}(\omega) = \frac{e^{fs(\omega)}}{\sum_{\omega^* \in \mathcal{P}_{\mathbb{T},n}} e^{fs(\omega^*)}}, \tag{2.4}$$

where this distribution depends on f, and f determines the Hamiltonian and the temperature. Notice that if $f < 0$, SAPs with smaller span are preferred, and the model is referred to as

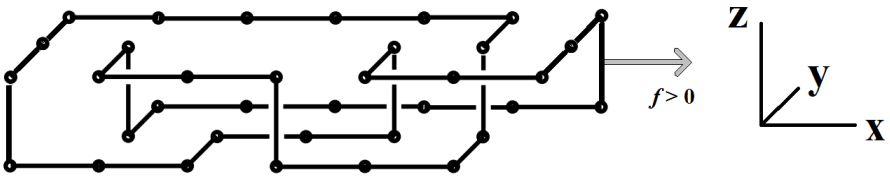

Figure 2.5: A force f acting upon a ring polymer is modelled by a SAP with span-s, where f acts parallel to the x-axis, perpendicular to and incident on the plane $x = s$. Here $f > 0$ is a stretching force.

being in the *compressed regime*. If $f > 0$, SAPs with larger span are preferred, and the model is referred to as being in the *stretched regime*. If $f = 0$, the probability distribution simplifies to

$$\mathbb{P}(\omega) = \frac{1}{\sum_{\omega^* \in \mathcal{P}_{\mathbb{T},n}} 1} = \frac{1}{p_{\mathbb{T},n}}, \tag{2.5}$$

where $p_{\mathbb{T},n} = |\mathcal{P}_{\mathbb{T},n}|$. Note that the counts $p_{\mathbb{T},n}$ can be calculated directly from a transfer matrix, as shown in Section 2.3.2.

2.3 Transfer Matrix Method

One advantage of working with SAPs in tubes is that the SAPs' "growth" is limited to the $+x$-direction. This allows us to utilize transfer matrices. In this section, it is explained how transfer matrices are applied to SAPs in tubes to obtain counts by length or span and growth rate estimates. It is also explained how the transfer matrix can be used to generate all SAPs of a certain length or span, as well as to obtain transition probabilities to perform Monte Carlo sampling of large sized SAPs.

2.3.1 Defining a Transfer Matrix for SAPs

In order to apply transfer matrix theory to SAPs in tubes, we first provide some necessary definitions. There are multiple ways to define an appropriate transfer matrix; here we use the definitions that correspond closest with my novel computer implementation that has allowed

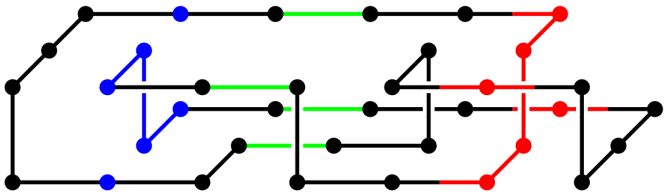

Figure 2.6: The blue vertices and edges denote the 1st hinge H_1, and the green edges denote the 3rd section S_3. The red vertices, edges, and half-edges denote a 1-block.

for the reduction of the size of the transfer matrices (see Section 3.2 for further details). These definitions are also used in [5, 10, 11, 12].

We start with a series of definitions that are illustrated in Figures 2.6, 2.7, and 2.8. Given a SAP ω with span-s in a tube $\mathbb{T}$, a *hinge* H_k $(0 \leq k \leq s)$ of ω is the set of edges and vertices lying in the intersection of ω and the y-z plane at $x = k$. A *section* S_k of ω is the set of edges in ω that connect the hinges H_{k-1} and H_k. A *half-section* of S_k is a set of half-edges in S_k, with either $k - 1 \leq x \leq k - \frac{1}{2}$ or $k - \frac{1}{2} \leq x \leq k$. A *1-block* of ω is any nonempty hinge, together with the half-edges of ω in the two adjacent half-sections. See Figure 2.6 for an example of a hinge, section, and 1-block.

For a 1-block β, let $\mathcal{L}_\beta = \{l_1, \ldots, l_{2p}\}$ be the set of half-edges on the left (it may be the case that $p = 0$ if the 1-block is at the "start" of the SAP). Similarly, let $\mathcal{R}_\beta$ be the set of half-edges on the right. If $p > 0$ and $\omega \in \mathbb{T}$ is a SAP containing an occurrence of β, then the part of ω to the left of β (ω_{left}) induces a partition of $\mathcal{L}_\beta$ into pairs. That is, for any l_i, follow the edges of ω on the left of β from l_i until eventually arriving back at some l_j; then l_i and l_j get paired. See Figure 2.7 for an example. Note that all pairings are possible unless $\mathcal{L}_\beta$ consists of all possible half-edges; then there must be at least one pairing must be between two adjacent half-edges. Then for a given 1-block β, we define $\Pi(\mathcal{L}_\beta)$ to be the set of all pair-partitions of $\mathcal{L}_\beta$, which are induced by polygons containing β in $\mathbb{T}$. If $p = 0$, then $\Pi(\mathcal{L}_\beta) = \{\emptyset\}$.

We define a *1-pattern* π to be a pair (β, ρ) where β is a 1-block and $\rho \in \Pi(\mathcal{L}_\beta)$. Note that a nonempty ρ induces a pairing on $\mathcal{R}_\beta$ – call this pairing ρ'. (If $\rho = \emptyset$, then the edges in β's hinge induce the pairing ρ'.) See Figure 2.7. If ρ and ρ' are both nonempty then we say π is a *proper 1-pattern*; if only ρ is empty then π is a *start 1-pattern*; and if only ρ' is empty

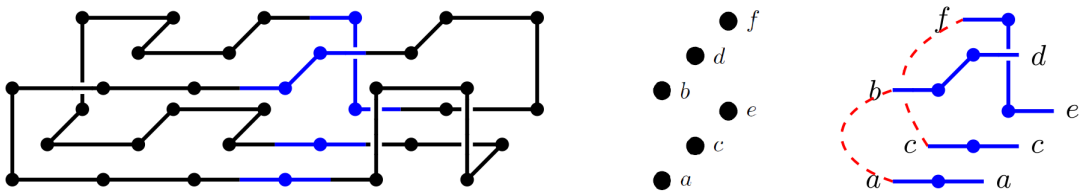

Figure 2.7: A polygon ω in $\mathbb{T}_{2\times 1}$ and the 1-block β (in blue) occurring between $x = 3\pm\frac{1}{2}$. If we label the six (y,z) locations of the $y-z$ plane from a to f lexicographically $((0,0)\to(0,1)\to(1,0)\to(1,1)\to\cdots\to(2,1))$, then here we have $\mathcal{L}_\beta = \{a,b,c,f\}$ and $\mathcal{R}_\beta = \{a,c,d,e\}$. The pairing ρ on $\mathcal{L}_\beta$ induced by ω_{left} is $\{\{a,b\},\{c,f\}\}$ (indicated by the dashed red lines), and this induces the pairing ρ'=$\{\{a,d\},\{c,e\}\}$ on $\mathcal{R}_\beta$. The pair (β,ρ) forms a 1-pattern.

then π is an *end 1-pattern*. We denote the sets of start, proper, and end 1-patterns in $\mathbb{T}$ by $\mathcal{A}_{\text{S}}, \mathcal{A}_{\text{P}}$ and $\mathcal{A}_{\text{E}}$ respectively. We also define $\mathcal{A}_0$ to be the set of all polygons in $\mathbb{T}$ with span $s = 0$; namely the 1-patterns for which both ρ and ρ' are empty.

Given two 1-patterns $\pi_1 = (\beta_1,\rho_1)$ and $\pi_2 = (\beta_2,\rho_2)$, we say π_2 can *follow* π_1 if $\rho_1' = \rho_2$. Notice that a polygon in a tube can be thought of as a "word" made of 1-patterns which can follow the previous 1-pattern. That is, a polygon (with span $s \geq 1$) consists of a start 1-pattern, a sequence of proper 1-patterns (if $s > 1$) which can follow the previous, and an end 1-pattern which can follow the last proper 1-pattern. See Figure 2.8 for an illustration. Note that an earlier definition of the transfer matrix for polygons in tubes (in [54]) included both left and right pairings on a 1-block in the 1-pattern definition. Removing the unnecessary right pairings has lead to a substantial reduction in the size of the transfer matrices (see 3.2 for further details).

With this definition of 1-patterns, we can now define appropriate transfer matrices. Assign a label to each of the k 1-patterns in $\mathcal{A}_{\text{P}}$ and denote them as $\pi_1,\pi_2,\ldots,\pi_k$. Then the $k\times k$ transfer matrix $T_{\mathbb{T}}(x) = T(x)$ for proper 1-patterns is defined as:

$$[T(x)]_{i,j} = \begin{cases} x^{|\pi_i|} & \text{if proper 1-pattern } \pi_j \text{ can follow proper 1-pattern } \pi_i \\ 0 & \text{otherwise,} \end{cases} \tag{2.6}$$

where $|\pi|$ is the length of the 1-block from which the 1-pattern π was derived. We can similarly define a "start transfer matrix". Assign a label to each of the k_S start 1-patterns in $\mathcal{A}_{\text{S}}$ and denote them as $\alpha_1,\alpha_2,\ldots,\alpha_{k_S}$. Then the $k_S\times k$ start transfer matrix $S_{\mathbb{T}}(x) = S(x)$

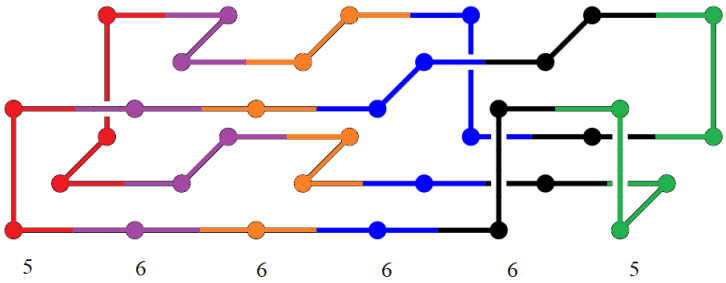

Figure 2.8: A polygon consists of a start 1-pattern (red), a sequence of proper 1-patterns which can follow the previous (purple, orange, blue, black), and an end 1-pattern (green). Also, for each 1-pattern, its associated power of x in their transfer matrix ($|\alpha_i|, |\pi_i|, |\gamma_j|$, from Equations 2.6, 2.7, 2.8) is written below.

for start 1-patterns is defined as:

$$[S(x)]_{i,j} = \begin{cases} x^{|\alpha_i|} & \text{if proper 1-pattern } \pi_j \text{ can follow start 1-pattern } \alpha_i \\ 0 & \text{otherwise.} \end{cases} \tag{2.7}$$

We can also define an "end transfer matrix". Assign a label to each of the k_E end 1-patterns in $\mathcal{A}_{\mathrm{E}}$ and denote them as $\gamma_1, \gamma_2, \ldots, \gamma_{k_E}$. Then the $k \times k_E$ end transfer matrix $E_{\mathbb{T}}(x) = E(x)$ for end 1-patterns is defined as:

$$[E(x)]_{i,j} = \begin{cases} x^{|\pi_i|+|\gamma_j|} & \text{if end 1-pattern } \gamma_j \text{ can follow proper 1-pattern } \pi_i \\ 0 & \text{otherwise.} \end{cases} \tag{2.8}$$

This formulation has an n-edge polygon with span-s contribute an x^n term in the i,j-th entry of $S(x)T(x)^{s-2}E(x)$, where i and j correspond to the polygon's start and end 1-patterns, respectively. For example, the polygon in Figure 2.8 will contribute an x^{34} term in an entry of $S(x)T(x)^3E(x)$.

2.3.2 Obtaining Counts of SAPs by Length or Span

Let $p_{\mathbb{T},n}(s)$ be the number of n-edge SAPs with span-s in $\mathbb{T}$. Using the above transfer matrices, transfer matrix theory [56] tells us the two-variable generating function for n-edge,

span-s, SAPs in $\mathbb{T}$ can be written in terms of the transfer matrices as:

$$F_{\mathbb{T}}(x,y) = \sum_{s\geq 0}\sum_{n\geq 4} p_{\mathbb{T},n}(s)x^n y^s \tag{2.9}$$

$$= \left[\sum_{s=0}^{1}\sum_{n\geq 4} p_{\mathbb{T},n}(s)x^n y^s\right] + \sum_{i,j}\left[\sum_{s=2}^{\infty} S(x)T(x)^{s-2}E(x)y^s\right]_{i,j}, \tag{2.10}$$

where the first term is the contribution of span $s = 0$ and $s = 1$ SAPs.

If we are interested in counts by span ($p_{\mathbb{T}}(s)$), the corresponding generating function $G_{\mathbb{T}}(y)$ can be found via:

$$G_{\mathbb{T}}(y) = \sum_{s=0}^{\infty} p_{\mathbb{T}}(s)y^s = F_{\mathbb{T}}(1,y) = \sum_{s=0}^{1} p_{\mathbb{T}}(s)y^s + \sum_{i,j}\left[\sum_{s=2}^{\infty} S(1)T(1)^{s-2}E(1)y^s\right]_{i,j}.$$

Thus $p_{\mathbb{T}}(s)$ can be found directly from the transfer matrices for $s > 1$ by:

$$p_{\mathbb{T}}(s) = \sum_{i,j}\left[S(1)T(1)^{s-2}E(1)\right]_{i,j}. \tag{2.11}$$

If instead we are interested in counts by length ($p_{\mathbb{T},n}$), the corresponding generating function $\hat{G}_{\mathbb{T}}(x)$ can be found via:

$$\hat{G}_{\mathbb{T}}(x) = \sum_{n=4}^{\infty} p_{\mathbb{T},n}x^n = F_{\mathbb{T}}(x,1) = \sum_{s=0}^{1} p_{\mathbb{T},n}x^n + \sum_{i,j}\left[\sum_{s=2}^{\infty} S(x)T(x)^{s-2}E(x)\right]_{i,j} \tag{2.12}$$

$$= \sum_{s=0}^{1} p_{\mathbb{T},n}x^n + \sum_{i,j}\left[S(x)(I-T(x))^{-1}E(x)\right]_{i,j}. \tag{2.13}$$

Thus the generating functions for $p_{\mathbb{T}}(s)$ and $p_{\mathbb{T},n}$ can be expressed in terms of the transfer matrices, and $p_{\mathbb{T}}(s)$ can be easily calculated by taking powers of the transfer matrix. In Chapter 3, Table 3.3, counts of $p_{\mathbb{T}}(s)$ obtained so far are provided. Note that $p_{\mathbb{T}}(s)$ for Hamiltonian polygons in the $2\times 1, 3\times 1$, and 2×2 tubes were published in 1998 in [29, TABLE III], and our counts confirm the counts in [29].

2.3.3 Asymptotic Growth Constants

Now let us examine the asymptotic growth of $p_{\mathbb{T},n}$ as $n\to\infty$ (fixed-edge), or $p_{\mathbb{T}}(s)$ as $s\to\infty$ (fixed-span). Here, we will focus on the fixed-edge case, but a very similar argument can be applied for the fixed-span case.

Since $\hat{G}_{\mathbb{T}}(x)$ is a power series, it has radius of convergence

$$r = \lim_{n\to\infty} (p_{\mathbb{T},n})^{-1/n},$$

assuming the limit exists. Taking the logarithm and multiplying by -1 gives:

$$-\log(r) = \lim_{n\to\infty} n^{-1} \log p_{\mathbb{T},n} =: \kappa_{\mathbb{T},p}, \tag{2.14}$$

which we call the "connective constant" for SAPs in tubes (κ_p). This limit has been proved to exist [55]. Recall from Equation 2.13 that the generating function for $p_{\mathbb{T},n}$ is:

$$\hat{G}_{\mathbb{T}}(x) = \sum_{n=4}^{\infty} p_{\mathbb{T},n} x^n = \sum_{s=0}^{1} p_{\mathbb{T},n} x^n + \sum_{i,j} \left[S(x)(I - T(x))^{-1} E(x) \right]_{i,j}. \tag{2.15}$$

Matrix theory tells us that the radius of convergence r of $\hat{G}_{\mathbb{T}}(x)$ is determined by the singularities of $\det(I - T(x))$ [56], and thus r is determined by the eigenvalues of $T(x)$ (details are given in my Master's thesis [20]). In particular, for a given value of x, let $\rho(x)$ be the spectral radius of $T(x)$, and let $x_0 > 0$ be the smallest value of x which makes $\rho(x) = 1$. Then x_0 is the radius of convergence of $\hat{G}_{\mathbb{T}}(x)$. If we ensure $T(x)$ is non-negative, irreducible, and aperiodic, then the Perron-Frobenius theorem [48] implies that such a value exists, and let ξ and η be the corresponding right and left eigenvectors of $\hat{G}_{\mathbb{T}}(x)$ (normalized such that $\eta^\top \xi = 1$). Then as in Alm and Janson [2] Equation 2.13 can be re-written for large n as:

$$\begin{aligned}
\lim_{x\to x_0} (x_0 - x)\hat{G}_{\mathbb{T}}(x) &\sim \lim_{x\to x_0} (x_0 - x) \sum_{i,j} \left[S(x)(I - T(x))^{-1} E(x) \right]_{i,j} \\
\lim_{x\to x_0} (x_0 - x) \sum_{n=4}^{\infty} p_{\mathbb{T},n} x^n &\sim \lim_{x\to x_0} \sum_{i,j} (S(x)(x_0 - x)(I - T(x))^{-1} E(x))_{i,j} \\
&\sim \sum_{i.j} (S(x_0)(x_0 \beta^{-1} \xi \eta^\top) E(x_0))_{i,j} \\
&\sim x_0 \beta^{-1} \sum_{i,j} (S(x_0) \xi \eta^\top E(x_0))_{i,j},
\end{aligned} \tag{2.16}$$

where $\beta = x_0 \eta^\top T'(x_0) \xi$ [2] ($T'(x_0)$ is the derivative of $T(x)$ with respect to x, evaluated at

x_0) . For ease of notation, let $\sum_{i,j}(S(x_0)\xi\eta^\top E(x_0))_{i,j} = A(x_0)$. Then as $x \to x_0$,

$$\begin{aligned}\sum_{n=4}^{\infty} p_{\mathbb{T},n}x^n &\sim x_0\beta^{-1}A(x_0)(x_0-x)^{-1} \\ &\sim \beta^{-1}A(x_0)(1-x/x_0)^{-1} \\ &\sim \beta^{-1}A(x_0)\sum_{n=0}^{\infty}(x/x_0)^n \\ &\sim \beta^{-1}A(x_0)\sum_{n=0}^{\infty}x_0^{-n}x^n. \end{aligned} \tag{2.17}$$

Differentiating both sides of the above equation n times with respect to x, setting $x = 0$, and dividing by $n!$ implies that

$$p_{\mathbb{T},n} \sim \beta^{-1}A(x_0)(x_0)^{-n} \text{ as } n \to \infty. \tag{2.18}$$

From Equation 2.14, $e^{\kappa_{\mathbb{T},p}} = x_0^{-1}$, so we have

$$p_{\mathbb{T},n} \sim C_{\mathbb{T}}e^{\kappa_{\mathbb{T},p}n} = C_{\mathbb{T}}\mu_{\mathbb{T},p}^n, \tag{2.19}$$

where $C_{\mathbb{T}} = \beta^{-1}A(x_0) = \beta^{-1}\sum_{i,j}(S(x_0)\xi\eta^\top E(x_0))_{i,j}$ and $\mu_{\mathbb{T},p} = x_0^{-1}$ is called the *growth constant*. Both $C_{\mathbb{T}}$ and $\mu_{\mathbb{T},p}$ can be calculated from the spectral radius and corresponding eigenvectors of the transfer matrix. These are calculated by using a combination of the Power Method [77] and the False Position Method [73].

2.3.4 Generating and Sampling SAPs By Utilizing Transfer Matrices

Transfer matrices can also be used to generate all SAPs in tubes (of a certain size). Since the transfer matrices contain the "connectivity" information of the 1-patterns, SAPs can be generated by building up the SAPs from left to right, until the desired span (or number of edges) is reached. This can be done by storing the actual configuration of the 1-patterns (when generating the transfer matrix), instead of just storing the number of edges (i.e. $x^{|\pi_i|}$). Generating a complete set of all polygons with a certain span (or number of edges) can then be done by exhaustively going through every possible valid combination of start 1-pattern $\to$ proper 1-patterns $\to$ end 1-pattern. Below is pseudocode for generating all polygons of a desired span.

```
for all start 1-patterns do
  AddStartPattern()
  while currSpan < desiredSpan − 1/2 do
    for all proper 1-patterns that can follow do
      Recursively loop through all combinations of proper 1-patterns until currSpan =
      desiredSpan − 1/2
      for all end 1-patterns that can follow the last proper 1-pattern do
        AddEndPattern()
        SavePolygon()
      end for
    end for
  end while
end for
```

The knot-type of each generated SAP can be identified as described in Section 2.4.3, and then the resulting sequence of knot-types determines the knot distribution for a given SAP size. In Chapter 3, Tables 3.3 and 3.4 contain results.

Transfer matrix theory from Alm and Janson [2] can also be used to find the limiting transition probabilities between proper 1-patterns. This is used in the Monte Carlo method developed by Beaton [10, 12] to obtain uniform, independent, identically distributed samples of large SAPs in tubes.

Consider the fixed-span model where each SAP with span-s is equally likely. Let $T(x)$ be the proper 1-pattern transfer matrix (defined earlier in Section 2.3.1) and let λ be the dominant eigenvalue of $T(1)$. After checking that the matrix $T(1)$ is irreducible and aperiodic, by the Perron-Frobenius theorem, λ is real, positive, and simple. Let ζ be the corresponding right eigenvector, and let i and j be proper 1-patterns such that j can follow i. Let $q_{ij}(s)$ be the transition probability that an occurrence of i is followed by j in a uniformly random polygon of span-s. From Alm and Janson [2, Section 7], the limiting transition probability

as $s \to \infty$ is

$$q_{ij}(s) \to q_{ij} = \lambda^{-1} \frac{\zeta_j}{\zeta_i}, \tag{2.20}$$

where ζ_i is the i-th component of the eigenvector ζ. SAPs are randomly generated by building them as a sequence of 1-patterns, using the above transition probabilities. The sampling procedure in pseudocode for generating a SAP ω, comprised of $(s+1)$ 1-patterns $b_0, b_1, \ldots, b_s$ is as follows:

Select b_0 uniformly at random from all N_{start} start 1-patterns
if b_0 is not rejected according to $r_1(b_0)$ (detailed below) **then**
  Select b_1 from all proper 1-patterns which can follow b_0 with probability proportional to ζ_{b_1}
  for $i = 2, 3, \ldots, s-1$ **do**
    Select b_i with probability q_{b_{i-1}, b_i}
  end for
  if b_{s-1} is not rejected according to $r_s(b_{s-1})$ (detailed below) **then**
    Select b_s uniformly at random from all end 1-patterns which can follow b_{s-1} ($N_{\text{end}}(b_{s-1})$)
  else
    Restart
  end if
else
  Restart
end if

The rejection probabilities r_1 and r_s are chosen such that the sampling is uniform. First define

$$t_1(i) = \sum_{j \text{ follows } i} \zeta_j \quad \text{and} \quad t_s(i) = \frac{N_{\text{end}}(i)}{\zeta_i}, \tag{2.21}$$

where $N_{\text{end}}(i)$ is the number of end 1-patterns that can follow i. Then the rejection proba-

bilities are:

$$r_1(b_0) = 1 - \frac{t_1(b_0)}{\max\limits_{i \text{ start}}\{t_1(i)\}} \quad \text{and} \quad r_s(b_{s-1}) = 1 - \frac{t_s(b_{s-1})}{\max\limits_{i \text{ internal}}\{t_s(i)\}}. \tag{2.22}$$

Thus, a polygon consisting of the 1-patterns $b_0, b_1, \ldots, b_s$ has a selection probability of:

$$\left(\frac{1}{N_{\text{start}}}\right)\left(\frac{t_1(b_0)}{\max\limits_{i \text{ start}}\{t_1(i)\}}\right)\left(\frac{\zeta_{b_1}}{t_1(b_0)}\right)\left(\lambda^{-1}\frac{\zeta_{b_2}}{\zeta_{b_1}}\right)\cdots\left(\lambda^{-1}\frac{\zeta_{b_{s-1}}}{\zeta_{b_{s-2}}}\right)\left(\frac{N_{\text{end}}(b_{s-1})/\zeta_{b_{s-1}}}{\max\limits_{i \text{ internal}}\{t_s(i)\}}\right)\left(\frac{1}{N_{\text{end}}(b_{s-1})}\right)$$
$$= \left(\frac{1}{N_{\text{start}}}\right)\left(\frac{1}{\max\limits_{i \text{ start}}\{t_1(i)\}}\right)\left(\lambda^{-(s-2)}\right)\left(\frac{1}{\max\limits_{i \text{ internal}}\{t_s(i)\}}\right),$$

which does not depend on the chosen 1-patterns $b_0, b_1, \ldots, b_s$. Thus the sampling is uniform.

Note that a similar sampling procedure can be done for the fixed-edge model by using the transition probability [2, Section 7]

$$p_{ij}(n) \to p_{ij} = x_0^{|i|}\frac{\xi_j}{\xi_i} \qquad \text{as} \quad n \to \infty, \tag{2.23}$$

where x_0 is the value of x which makes the spectral radius of $T(x) = 1$, and ξ is the dominant right eigenvector of $T(x_0)$.

2.4 Basic Knot Theory

Much of the work in this thesis involves the knotting and linking of SAPs. Therefore, it is important to define a "mathematical knot" and a "mathematical link", as well as what we mean by "knot-type" and "link-type." In this section, a brief introduction to knot theory is given. Unless stated otherwise, the standard definitions in this section are from [1] and [17].

2.4.1 Mathematical Knots

A *mathematical knot* is defined as an embedding of a simple closed curve in $\mathbb{R}^3$. The difference between mathematical knots and the conventional idea of a knot (such as in a shoelace) is that mathematical knots must be closed. That is, there are no ends to tie or untie the knot. Notice that a SAP is a knot since it is a closed, non-self-intersecting curve. Two knots are considered *equivalent* if one knot can be continuously deformed (that is no breaks or cuts are

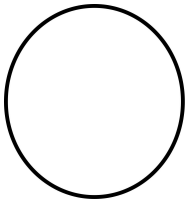

Figure 2.9: The trivial knot, called the unknot (0_1).

allowed) into the other. Equivalence classes are naturally formed from this definition, and these equivalence classes are referred to as *knot-types*.

For a given knot, a *regular knot projection* is a projection of the knot into a plane in such a way that there are no "triple points" (three points of the knot that get projected to the same point). To obtain a knot diagram of the knot, when making a regular projection of the knot, at each double point of the projection (called a *crossing* in the diagram), information about which strand of the knot is over and which is under at the double point is retained (see Figure 2.11 for examples of knot diagrams). The *minimal crossing number* of a knot is the smallest number of crossings of any knot diagram of the knot. Knot-types are typically named in the form n_m, where n is the minimal crossing number of the knot and m represents the m-th knot with n minimal crossings as tabulated in [49]. One measure of the complexity of a knot K is its minimal crossing number $c(K)$, where a knot with a low $c(K)$ is said to be "simpler" than one with a larger $c(K)$.

The simplest knot-type is the trivial knot, called the unknot (denoted by 0_1). See Figure 2.9. If a knot is not the unknot, then we say it is *knotted*. The simplest nontrivial knot is the trefoil knot (denoted by 3_1). If a knot is equivalent to its mirror image, then we call it *achiral*; if it is not equivalent to its mirror image, then we call it *chiral*. Note that 3_1 is chiral, and there are two types of trefoils: the positive trefoil and the negative trefoil. Knot diagrams of these knots are shown in Figure 2.11, with over and under crossings indicated. Note that each crossing is considered positive or negative, based on a *right-hand rule* (see Figure 2.10). These two types of trefoils are not equivalent; therefore, they are considered to be different knot-types (denoted by 3_1^+ and 3_1^- respectively). An example of an achiral knot is the figure-8 knot, as shown in Figure 2.11.

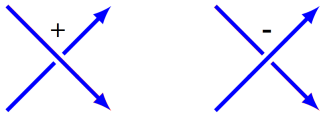

Figure 2.10: The right-hand-rule for crossings in a SAP.

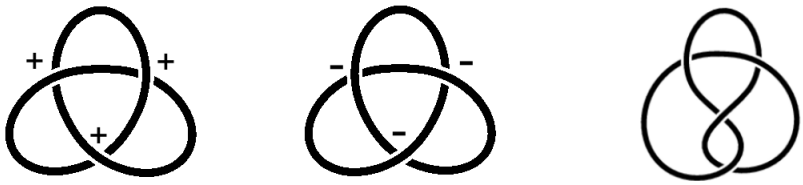

Figure 2.11: Knot diagrams of the positive trefoil (3_1^+), negative trefoil (3_1^-), and the figure-8 (4_1). The 3_1 is chiral, while the 4_1 is achiral.

If a knot is made of two or more independent (non-trivial) knots joined together by a "connect-sum operation" (as in Figure 2.12), then the resulting knot is called a *composite knot*. A *prime knot* is one that cannot be decomposed into two or more (non-trivial) knots. The composition of two knots (K_1 and K_2) is represented by $K_1 \# K_2$, and we say it is the *connect-sum* of its *factors* K_1 and K_2. See Figure 2.12 for an example of a 3_1^+ knot composed with a 3_1^- knot.

2.4.2 Mathematical Links

It is also possible to have multiple non-intersecting closed curves embedded in $\mathbb{R}^3$, where each curve is a knot. A *mathematical link* is a finite union of non-intersecting knots. In this thesis, we are only interested in links which consist of one or two non-intersecting knots, called *components*. The simplest link consists of only one component, which is a knot; therefore

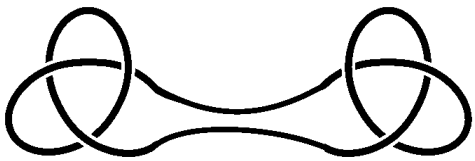

Figure 2.12: An example of a composite knot, the $3_1^+ \# 3_1^-$.

Figure 2.13: Knot diagrams of the unlink (0_1^2) (left) and the Hopf link (2_1^2) (right).

the set of knots is a subset of the set of links. However, in this thesis, we will refer to one-component links as just knots, and the word link will refer to two-component links.

Just like with knots, two links are considered *equivalent* if one link can be continuously deformed into the other. Again, equivalence classes are naturally formed from this definition, and these equivalence classes are referred to as *link-types*. The simplest two-component link is the trivial link, called the *unlink*, which is two separable unknots (Figure 2.13). Also, we say a link is *split* if its components can be continuously deformed so that each component lies in disjoint balls in $\mathbb{R}^3$, and if a link is not split, then it is called a *non-split* link.

The simplest two-component nontrivial non-split link is called the Hopf link, which is two unknots linked together (Figure 2.13). Link-types are typically named in the form n_m^c, where n is the minimal number of crossings in the link, c is the number of components in the link, and m represents the m-th link with n crossings and c components, as tabulated in [49] (e.g. the unlink is denoted 0_1^2 and the Hopf link is denoted 2_1^2). If a link consists of a connect-sum of two or more independent (non-trivial) links, then it is considered a *composite link.*, and the non-trivial links are called *factors*. A "prime link" is one that cannot be decomposed into two or more (non-trivial) links.

2.4.3 Identifying Knot and Link-types

Given two knots or links, it is generally not easy to determine whether they are equivalent. Accordingly, it is not easy to identify knot-types or link-types of a given knot or link diagram. A knot/link *invariant* is something that can be calculated for each knot/link, such that the invariant is the same for each equivalent knot/link. A knot/link invariant can be useful for distinguishing between knot-types if the invariant gives different values for different knot-types. But there is no known invariant that does that for every knot-type. For exam-

ple, minimal crossing number is a knot/link invariant (two equivalent knots will have the same minimal crossing number). However, there are two different minimal crossing number 5 knot-types (5_1 and 5_2), and hence minimal crossing number cannot be used to distinguish between those knot-types. Thus, an ongoing area of study in knot theory is to search for an invariant that distinguishes between the maximum number of knot-types. Some commonly used invariants are the Alexander, Jones, and HOMFLY polynomials. They have the advantage that algorithms have been developed by others to calculate these polynomials. Details on how to calculate these polynomials are not given here, but can be found in [1]. Note that some knot-types have the same polynomials, but such occurrences are expected to be rare for the size of polygons studied here (where the most likely prime knots have small minimal crossing number), and these occurrences are unlikely to noticeably affect any statistics. For the results in this thesis, the HOMFLY polynomial was used to identify knots and links via the software Knotplot [49], which algorithmically determines the knot-type following an approach which is detailed in [58].

Note that the polynomial invariants are calculated based on the crossings of a regular projection of the knot/link. The knots and links in this thesis are confined to narrow tubes, and the projections of some of these knots/links contain thousands of crossings. In these cases with very large amounts of crossings, calculating these polynomials directly is too difficult a task.

As part of this Ph.D. work, to solve this issue, knots are first "simplified" prior to calculating their HOMFLY polynomial. For knots, we can "slice" a polygon in a tube at any half-integer x-plane that only contains two edges (referred to as a *2-section*). We can then close up the two loose ends "left" of the 2-section and the two loose ends "right" of the 2-section. This forms two smaller polygons with knot-types K_1 and K_2, and notice that if the original polygon had knot-type K, then $K = K_1 \# K_2$. This procedure can be repeated at every 2-section, which results in a long polygon being split into p smaller polygons with $K = K_1 \# K_2 \# \ldots \# K_p$. Moreover, long polygons have a positive density of 2-sections, so on average $p = O(s)$ [12], where s is the span of the original polygon. See Figure 2.14 for an illustration of this slicing process.

Also for knots, we know that any SAP in $\mathbb{Z}^3$ with fewer than 24 edges is an unknot [50],

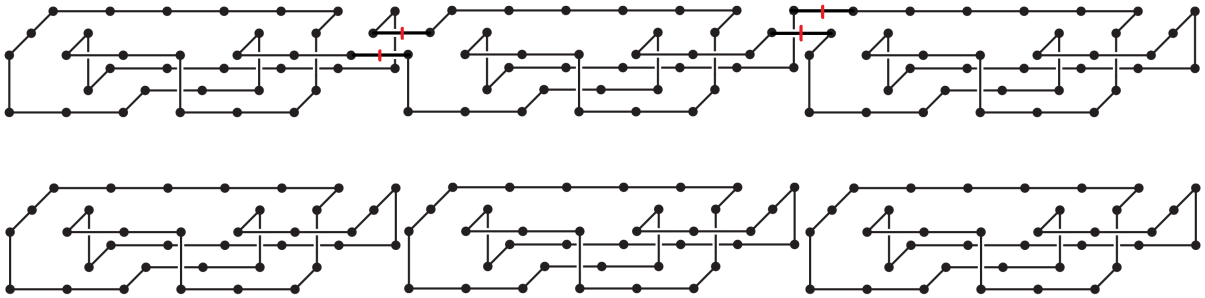

Figure 2.14: The top polygon's knot-type can be determined by slicing the polygon at 2-sections (indicated by red) and identifying the knot-type of each of the resulting polygons (below). The knot-type of the top polygon is the knot composition of each of the knot-types of the smaller polygons. In this case, the original polygon has knot type $3_1\#3_1\#3_1$.

Figure 2.15: This figure illustrates Type 0, +2, and -2 moves from the BFACF algorithm, introduced in [70]. These moves can be used to reduce the size of a polygon without changing its knot-type.

so if any of the small polygons from the above procedure have fewer than 24 edges, they are unknots and can be discarded. For those that have 24 or more edges, "BFACF moves" [70] are used (see Figure 2.15 for an illustration of the BFACF moves). BFACF moves perform "local changes" on a polygon which can decrease the length of a polygon without changing its knot-type [70]. If a small polygon's size can be reduced below 24 edges, then it is an unknot and is discarded.

After slicing the original polygon at each 2-section to form smaller polygons, and shrinking (if possible) these smaller polygons using BFACF moves, the result is a number of polygons each with lengths 24 or larger. Each polygon's knot-type is identified (if possible) via the software Knotplot [49]. Then the original polygon's knot-type is the connect sum of these knot-types. Note that Knotplot identifies prime knots up to 10 crossings. In the extremely rare case, some polygons could not be identified. These unknown knot-types were categorized

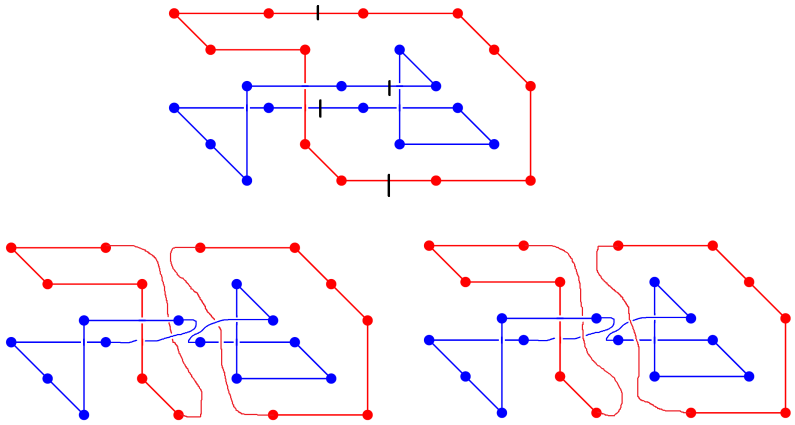

Figure 2.16: This figure illustrates that link-type will change depending on how a sliced 4-section is reconnected.

as prime knots that consisted of more than 10 crossings. However, these cases were so rare that any incorrect classifications would not noticeably affect any of the results.

For links, this thesis only considers two-component links (2SAPs). Since every section of a 2SAP has at least four edges, we do not yet have an analagous "slicing method" to simplify 2SAPs as described above for polygons. This is because the link-type will change based on how the sliced 4-section is reconnected (see Figure 2.16 for an illustration). There is potential to manipulate a 2SAP and perform slicing on each individual polygon in the 2SAP, but that was not done here. We do know that if either component of a two-component link on $\mathbb{Z}^3$ has fewer than eight edges, then the link must be an unlink. Modified BFACF moves were used in an attempt to shrink either component of the 2SAP below 8 edges. For those 2SAPs that were not able to be shrunk below this threshold, they had their link-type calculated via the software Knotplot [49].

Note that for links, Knotplot identifies prime link-types up to 9 crossings. Due to a lack of a "slicing method" for links, in some cases (larger tube sizes, especially Hamiltonian) there were a significant number of 2SAPs that could not have their link-type identified. Due to this, analysis was limited to the simpler link-types. Identifying 2SAPs with crossing numbers larger than 9 is left as an open problem. More details involving the challenges associated with 2SAP link identification are given in Section 4.5.

2.5 Summary

This chapter contained the fundamentals needed for the remainder of this thesis. First, the definitions of the main items and terms are given (Section 2.1). Then an explanation of the three main ingredients in a statistical mechanics model of a polymer in dilute solution are presented: the set of possible conformations, a Hamiltonian function which determines the potential energy associated with each conformation, and an equilibrium distribution for the conformations based on the Hamiltonian (Section 2.2). Two examples of these three ingredients were then given for a lattice SAP model (Section 2.2.2), as well as for SAPs confined to a tube (Section 2.2.3). Next, a transfer matrix for SAPs in tubes was defined (Section 2.3.1), and some transfer matrix theory was given to show how quantities of interest can be calculated from transfer matrices (Sections 2.3.2 and 2.3.3). The algorithm for the exact generation of SAPs, as well as the sampling procedure to obtain independent uniform samples of SAPs, was then presented (Section 2.3.4). Lastly, some basic knot theory was given to explain knot- and link-types, and the identification procedure used to determine knot- and link-types is explained, along with a new knot identification method which was used to identify long span polygons. (Section 2.4).

In the next chapter, the creation of transfer matrices for small tube sizes is explained, and they are used to calculate asymptotic growth rates. The transfer matrices are slightly modified to store the actual configurations of their 1-patterns, and these modified transfer matrices are used to generate and sample polygons to examine fixed knot-type SAPs.

3 SELF-AVOIDING POLYGONS CONFINED TO A LATTICE TUBE

Polymers are often confined in some way; for example, DNA can be confined in a cell, nucleus, or viral capsid [41]. These geometrical constraints can affect the conformational and physical properties (such as the entanglement complexity) of confined polymers in many ways [38]. These confinement effects have motivated adding spatial constraints into the standard lattice model of polymers. Such spatial constraints include confining a lattice polygon to a sphere, box, wedge, or slab (see review in [41]). As described before, this thesis focuses on confining a lattice polygon to a semi-infinite tube of $\mathbb{Z}^3$, where the polygon is confined between four planes ($z = 0, z = L, y = 0, y = M$) with $x \geq 0$. The entanglement complexity of these polygons are of interest; for example, the knotting probabilities of different knot-types and the localization of knotting are topics of interest. To study the knotting of polygons, we need to be able to generate polygons, since determining knot-type requires the entire polygon.

As mentioned previously, one main advantage of working with SAPs in tubes is that the polygon's "growth" is limited to the $+x$-direction; this allows for the use of transfer matrices. This thesis expands on previous work presented in my Master's thesis [20], where transfer matrices were created for SAPs in the 1×1, 2×1, and 3×1 tube sizes. In this thesis, transfer matrices are created for the 4×1, 5×1, 2×2, and 3×2 tube sizes. Some of the work done in this thesis is also part of the published papers [5, 11, 12]

The new transfer matrices are used to calculate new exponential growth rates (Table 3.1), calculate new exact knot distributions (Tables 3.3 and 3.4), and study the asymptotic knot distribution of SAPs in these larger tube sizes. Utilizing the new transfer matrices, a large database consisting of millions of independent, uniformly sampled, large span (up to span 1200) SAPs in these larger tube sizes is created. From this database of SAPs, evidence is provided suggesting that the exponential growth rate of polygons with a fixed knot-type in

a tube is the same as that for unknots, and evidence is provided towards the conjectured asymptotic growth form of the number of polygons with fixed knot-type K (Equation 3.6). This conjectured form is consistent with the idea that knotting occurs in a relatively localized manner. Also, using this database of SAPs, two different modes of knot patterns, "local" and "non-local", are studied. For the local mode, there is a knotted arc in the pattern, while for the non-local mode, it is necessary to "go outside" the pattern to form a knotted arc (Figure 3.9 contains an illustration of the difference between these two modes).

This chapter is laid out as follows: Section 3.1 reviews the SAP in a tube model, including the difference between a fixed-edge and fixed-span model, and presents the new exponential growth rates that were calculated. Section 3.2 discusses how the larger transfer matrices were created by increasing the efficiency while creating and storing transfer matrices. Section 3.3 contains exact results that were obtained by utilizing these larger transfer matrices, and Section 3.4 contains the Monte Carlo results, along with evidence to support the aforementioned conjecture (Equation 3.6). Section 3.5 uses the random samples of SAPs to examine and compare the two different modes of knotting seen in polygons in a tube.

3.1 The Model

Recall that in Section 2.2.3, we defined $\mathcal{P}_{\mathbb{T}}$ to be the set of SAPs in an $L \times M$ tube $\mathbb{T}$, $\mathcal{P}_{\mathbb{T},n}$ to be the subset of $\mathcal{P}_{\mathbb{T}}$ with n edges, and let $p_{\mathbb{T},n} = |\mathcal{P}_{\mathbb{T},n}|$. Also, let $\mathcal{P}_{\mathbb{T}}(s)$ be the subset of $\mathcal{P}_{\mathbb{T}}$ with span-s, and as in Section 2.3.2, let $p_{\mathbb{T}}(s) = |\mathcal{P}_{\mathbb{T}}(s)|$. Similarly for Hamiltonian SAPs, define $\mathcal{P}^{\mathrm{H}}_{\mathbb{T}}$ to be the set of Hamiltonian SAPs in $\mathbb{T}$, let $\mathcal{P}^{\mathrm{H}}_{\mathbb{T},n}$ be the subset of $\mathcal{P}^{\mathrm{H}}_{\mathbb{T}}$ with n edges, and let $p^{\mathrm{H}}_{\mathbb{T},n} = |\mathcal{P}^{\mathrm{H}}_{\mathbb{T},n}|$. Notice that if s is the span of a Hamiltonian SAP, then $n = (s+1)(L+1)(M+1)$.

3.1.1 Exponential Growth Rates

It was shown in 1989 by Soteros and Whittington [55] that for an $L \times M$ tube $\mathbb{T}$ ($L, M \geq 1$) the limit

$$\lim_{n\to\infty} n^{-1} \log p_{\mathbb{T},n} \equiv \kappa_{\mathbb{T}} \tag{3.1}$$

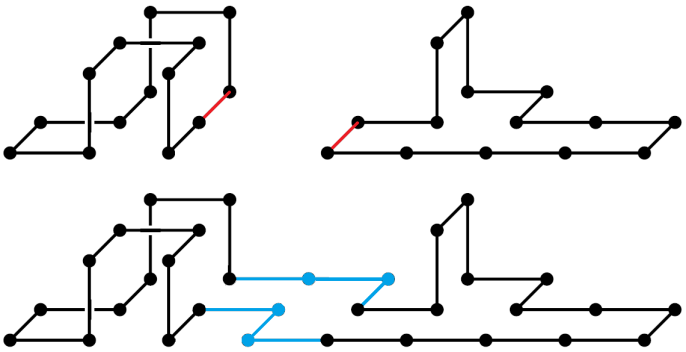

Figure 3.1: An example of concatenating two polygons in the 2×1 tube. The red edges are removed and the blue edges join the polygons.

exists (n even), where $\kappa_{\mathbb{T}}$ is called the connective constant for SAPs in $\mathbb{T}$. For Hamiltonian SAPs, I showed in my Master's thesis [20] that the limit

$$\lim_{n\to\infty} n^{-1} \log p^{\mathrm{H}}_{\mathbb{T},n} \equiv \kappa^{\mathrm{H}}_{\mathbb{T}} \tag{3.2}$$

also exists (where the limit is taken through multiples of $(L+1)(M+1)$).

A sketch of the proof for the existence of the above limits is as follows. First it is shown that two polygons (ω_1 and ω_2) in $\mathbb{T}$ can be concatenated (joined) by: translating ω_2 to the right of ω_1, removing a rightmost edge from ω_1 and a leftmost edge from ω_2, and adding a (minimal) number of edges $c_{\mathbb{T}}$ to join the two polygons. If ω_1 has n_1 edges and ω_2 has n_2 edges, the result is a new polygon in $\mathbb{T}$ with $n_1 + n_2 + c_{\mathbb{T}} - 2$ edges. See Figure 3.1 for an illustration of such a concatenation. Thus we have $p_{\mathbb{T},n_1} p_{\mathbb{T},n_2} \leq p_{\mathbb{T},n_1+n_2+c_{\mathbb{T}}-2}$, or equivalently

$$\log p_{\mathbb{T},n_1-c_{\mathbb{T}}+2} + \log p_{\mathbb{T},n_2-c_{\mathbb{T}}+2} \leq p_{\mathbb{T},n_1+n_2-c_{\mathbb{T}}+2}.$$

Fekete's lemma (see for example [57, Lemma 1.2.1]) states that if $\{a_n\}_{n=1}^{\infty}$ is a *superadditive* sequence (i.e. $a_n + a_m \leq a_{n+m}$) of real numbers, then $\lim_{n\to\infty} \frac{a_n}{n}$ exists in $(-\infty, \infty]$ and $\lim_{n\to\infty} \frac{a_n}{n} = \sup_{n\geq 1} \frac{a_n}{n}$. The sequence $a_n = \log p_{\mathbb{T},n-c_{\mathbb{T}}+2}$ is superadditive, so by applying Fekete's lemma, we have the limit in Equation (3.1) exists. A conctenation of Hamiltonain SAPs is shown in my Master's thesis [20], which results in the existence of the limit in Equation (3.2).

From transfer matrix theory, as described in Section 2.3, Equations (3.1) and (3.2) give

Table 3.1 Growth rates and connective constants for the fixed-edge, Hamiltonian, and fixed-span models. $\kappa_{\mathbb{T}}$ and $\mu_{\mathbb{T}}$ are the connective constants and growth rates, respectively, for the fixed-edge model (Equations 3.1 and 3.3). $\kappa_{\mathbb{T}}^{\mathrm{H}}$ and $\mu_{\mathbb{T}}^{\mathrm{H}}$ are the connective constants and growth rates, respectively, for the Hamiltonian model (Equations 3.2 and 3.4). $\chi_{\mathbb{T}}$ and $\nu_{\mathbb{T}}$ are the connective constants and growth rates, respectively, for the fixed-span model (Equations 3.7 and 3.8). These numbers are calculated from the transfer matrices and error is expected to be confined to the last digit.

Tube Size	$\kappa_{\mathbb{T}}$	$\mu_{\mathbb{T}}$	$\kappa_{\mathbb{T}}^{\mathrm{H}}$	$\mu_{\mathbb{T}}^{\mathrm{H}}$	$\chi_{\mathbb{T}}$	$\nu_{\mathbb{T}}$
1x1	0.602581	1.826828	0.329240	1.389910	1.945910	7.000000
2x1	0.826948	2.286331	0.440751	1.553874	3.536898	34.360181
3x1	0.944703	2.572050	0.488109	1.629232	5.106969	165.169003
4x1	1.016490	2.763477	0.515163	1.673912	6.647594	770.927137
5x1	1.064376	2.899030	0.532587	1.703334	8.178333	3562.9113648
2x2	1.004778	2.731300	0.516565	1.676260	6.032775	416.870159
3x2	1.099898	3.003860	0.565046	1.759529	8.506307	4945.864451

us

$$p_{\mathbb{T},n} \sim C_{\mathbb{T}} \mu_{\mathbb{T}}^{n}, \qquad \text{as} \quad n \to \infty, \tag{3.3}$$

where $\mu_{\mathbb{T}} = e^{\kappa_{\mathbb{T}}}$ is called the *growth constant* or *growth rate* for SAPs in $\mathbb{T}$, and

$$p_{\mathbb{T},n}^{\mathrm{H}} \sim C_{\mathbb{T}}^{\mathrm{H}} \left(\mu_{\mathbb{T}}^{\mathrm{H}}\right)^{n}, \qquad \text{as} \quad n \to \infty, \tag{3.4}$$

where $\mu_{\mathbb{T}}^{\mathrm{H}} = e^{\kappa_{\mathbb{T}}^{\mathrm{H}}}$. The constants $C_{\mathbb{T}}, C_{\mathbb{T}}^{\mathrm{H}}, \kappa_{\mathbb{T}}, \kappa_{\mathbb{T}}^{\mathrm{H}}, \mu_{\mathbb{T}}$ and $\mu_{\mathbb{T}}^{\mathrm{H}}$ are determined by the eigenvectors and eigenvalues of the transfer matrix (details in Section 2.3). Numerical estimates for $\kappa_{\mathbb{T}}, \kappa_{\mathbb{T}}^{\mathrm{H}}, \mu_{\mathbb{T}}$ and $\mu_{\mathbb{T}}^{\mathrm{H}}$ were calculated in my Master's thesis [20] for tube sizes $L \times 1$ ($1 \leq L \leq 4$) and 2×2. Creating new transfer matrices for the 5×1 and 3×2 tube sizes extended these results to those seen in Table 3.1.

To study the entanglement complexity of SAPs, we examine the growth rate of the number of n-edge SAPs with a fixed knot-type K. For all polygons, that is without the tube constraint, it is conjectured [68] that the number of n-edge polygons with knot-type K ($p_n(K)$) has the following asymptotic form:

$$p_n(K) \sim C_K \mu_{0_1}^{n} n^{\alpha_{0_1} - 3 + f_K}, \qquad \text{as} \quad n \to \infty, \tag{3.5}$$

where C_K and α_{0_1} are constants, μ_{0_1} is the growth rate for unknotted SAPs (the limit that defines it has been proved to exist [67]), and f_K is the number of prime knot factors in the prime knot decomposition of K, with $f_{0_1} = 0$. Note that it has been proven that the growth rate of unknots is less than that for all SAPs ($\mu_{0_1} < \mu$) [43, 60], proving the FWD conjecture. Notice that the conjecture in Equation 3.5 is implying that the growth rate for any knot-type K (assuming it exists) is the same as the growth rate of the unknot ($\mu_K = \mu_{0_1}$), however this has not been proved for any $K \neq 0_1$.

With the tube constraint, it is conjectured [12] that the number of n-edge SAPs with fixed knot-type K in tube $\mathbb{T}$ has the following asymptotic form:

$$p_{\mathbb{T},n}(K) \sim C_{\mathbb{T},K}\mu_{\mathbb{T},0_1}^n n^{f_K}, \qquad \text{as} \quad n \to \infty, \tag{3.6}$$

where $C_{\mathbb{T},K}$ is a constant and $\mu_{\mathbb{T},0_1}$ is the growth rate of unknots in $\mathbb{T}$. For the special case when $\mathbb{T} = 2 \times 1$, we have recently (in [5]) proved that $\mu_{2\times1,K} = \mu_{2\times1,0_1}$, and we have provided bounds on the exponent of n. Additionally, for knot-types that are connect sums of prime knots with "unknotting number" of 1, we prove the exponent of n is f_K. Numerical evidence is provided in Section 3.4 that the form in Equation 3.6 holds for tube sizes $L \times 1$ ($1 \leq L \leq 5$) and $L \times 2$ ($2 \leq L \leq 3$).

Almost all of the results in this thesis are based on enumerating SAPs by span instead of edges (for reasons explained in Section 3.1.2). If we count SAPs by span instead of edges, the asymptotic forms are not expected to change, but the constants will. It is shown in [11] that the limit

$$\lim_{s\to\infty} s^{-1} \log p_{\mathbb{T}}(s) \equiv \chi_{\mathbb{T}}, \tag{3.7}$$

exists, and thus,

$$p_{\mathbb{T}}(s) \sim D_{\mathbb{T}}\nu_{\mathbb{T}}^s, \qquad \text{as} \quad s \to \infty, \tag{3.8}$$

where $\nu_{\mathbb{T}} = e^{\chi_{\mathbb{T}}}$. Values for $\chi_{\mathbb{T}}$ and $\nu_{\mathbb{T}}$ were calculated from the fixed-span transfer matrices, and these values are also in Table 3.1.

Hamiltonian SAPs can also be counted by span, but length n is determined exactly by span-s through the relationship $n = (s+1)(L+1)(M+1)$. Thus the Hamiltonian connective

constants have the relationship:

$$\chi^{\mathrm{H}}_{\mathbb{T}} = \log \nu^{\mathrm{H}}_{\mathbb{T}} = \lim_{s\to\infty} \frac{1}{s} \log p^{\mathrm{H}}_{\mathbb{T},(s+1)(L+1)(M+1)} = (L+1)(M+1)\kappa^{\mathrm{H}}_{\mathbb{T}}.$$

So for enumeration by span, an equivalent form to the conjecture in Equation 3.6 is:

$$p_{\mathbb{T}}(s;K) \sim D_{\mathbb{T},K} \nu^{s}_{\mathbb{T},0_1} s^{f_K}, \qquad \text{as} \quad s\to\infty, \tag{3.9}$$

and for Hamiltonian SAPs:

$$p^{\mathrm{H}}_{\mathbb{T}}(s;K) \sim D^{\mathrm{H}}_{\mathbb{T},K} \left(\nu^{\mathrm{H}}_{\mathbb{T},0_1}\right)^{s} s^{f_K}, \qquad \text{as} \quad s\to\infty. \tag{3.10}$$

As discussed in Chapter 2, when the set $\mathcal{P}_{\mathbb{T}}(s)$ is used, we refer to this as the "fixed-span model", and when the set $\mathcal{P}_{\mathbb{T},n}$ is used, we refer to this as the "fixed-edge model".

3.1.2 Fixed-Edge vs Fixed-Span models

This subsection will explain some differences between the fixed-edge and fixed-span models and why the fixed-span model was primarily used in this thesis.

Recall from Section 2.2.1 that there are three main ingredients when modelling polymers:

1. A set Γ of all possible conformations of the polymer.
2. An energy function (Hamiltonian) $\mathcal{H}$ associated with each conformation $S \in \Gamma$.
3. An equilibrium distribution $\mathbb{P}$ for the conformations in Γ, based on the Hamiltonian.

Note that in this thesis there are two very different uses for the term "Hamiltonian" depending on the context. Here it is used to represent the energy function, but later in the section it is used to denote a SAP that occupies every vertex in a box (defined earlier in Equation 2.1.6). For the fixed-edge model, we use the following ingredients (also presented in Section 2.2.3):

1. The set Γ is $\mathcal{P}_{\mathbb{T},n}$, where each n-edge SAP ω in $\mathcal{P}_{\mathbb{T},n}$ represents the configuration of a ring polymer under confinement.
2. The Hamiltonian incorporates an external force f acting upon a polymer, parallel to the tube's direction. When $f > 0$ there is a stretching force, and when $f < 0$ there is a compressing force. Each n-edge SAP $\omega \in \mathcal{P}_{\mathbb{T},n}$ with span $s(\omega)$ has $-\beta\mathcal{H}(\omega) = fs(\omega)$.

3. The equilibrium probability of an n-edge SAP $\omega \in \mathcal{P}_{\mathbb{T},n}$ with span $s(\omega)$ is

$$\mathbb{P}_n^{(\mathrm{ed},f)}(\omega) = \frac{e^{fs(\omega)}}{\sum_{\omega^* \in \mathcal{P}_{\mathbb{T},n}} e^{fs(\omega^*)}}.$$

Here, if we take $f = 0$, so each n-edge SAP ω is equally likely: $\mathbb{P}_n^{(\mathrm{ed},0)}(\omega) = 1/p_{\mathbb{T},n}$. However, there has been work done where the force varies [7, 11].

In [7], Atapour et al. proved that the *limiting free energy per edge* for polygons in $\mathbb{T}$

$$\mathcal{F}_{\mathbb{T}}(f) = \lim_{n\to\infty} \frac{1}{n} \log \sum_s p_{\mathbb{T},n}(s) e^{fs}$$

exists for all f. In [11], Beaton et al. calculated bounds for $\mathcal{F}_{\mathbb{T}}(f)$, which are based on the growth rates for all polygons and for Hamiltonian polygons in $\mathbb{T}$. It is also proven in [11] that $\mathcal{F}_{\mathbb{T}}(f)$ is asymptotic to the line $f/2$ for $f \to \infty$ (for any $\mathbb{T}$), and to the line $\frac{f}{(L+1)(M+1)} + \kappa_{\mathbb{T}}^{\mathrm{H}}$ ($\kappa_{\mathbb{T}}^{\mathrm{H}}$ is defined in Equation 3.2) for $f \to -\infty$ (for small tube sizes where $\kappa_{\mathbb{T}}^{\mathrm{H}}$ is calculated). Note that since we published [11], I have now created the new transfer matrices for tube sizes up to 3×2 and 5×1, and it is now known that the $f \to -\infty$ result is true for cases up to these tube sizes, and it is conjectured to be true for all tube sizes.

For the fixed-span model, the following polymer model ingredients are used:

1. The set Γ is now $\mathcal{P}_{\mathbb{T}}(s)$, where each span-$s$ SAP ω in $\mathcal{P}_{\mathbb{T}}(s)$ represents the configuration of a ring polymer under confinement.
2. The Hamiltonian used is proportional to the length of the polymer. Each span-s SAP $\omega \in \mathcal{P}_{\mathbb{T}}(s)$ with $n(\omega)$ edges has $-\beta\mathcal{H}(\omega) = gn(\omega)$.
3. The equilibrium probability of a span-s SAP $\omega \in \mathcal{P}_{\mathbb{T}}(s)$ with $n(\omega)$ edges is

$$\mathbb{P}_s^{(\mathrm{sp},g)}(\omega) = \frac{e^{gn(\omega)}}{\sum_{\omega^* \in \mathcal{P}_{\mathbb{T}}(s)} e^{gn(\omega^*)}}.$$

Now, if we take $g = 0$, so each SAP ω with span-s is equally likely: $\mathbb{P}_s^{(\mathrm{sp},0)}(\omega) = 1/p_{\mathbb{T}}(s)$. It is known [11] that the *free energy per span* exists

$$\mathcal{G}_{\mathbb{T}}(g) = \lim_{n\to\infty} \frac{1}{n} \log \sum_n p_{\mathbb{T},n}(s) e^{gn}.$$

Most of the work and results done in this thesis are for the fixed-span model. One reason for this is that knots are much more common in the fixed-span model when compared to

the fixed-edge model. As shown later in Section 3.4.1, the growth rate of unknots can be estimated from the obtained Monte Carlo data. For example, from [12], in the 3×1 tube, we can compare the growth rates of unknots to all polygons:

$$\log\left(\frac{\mu_{\mathbb{T},0_1}}{\mu_{\mathbb{T}}}\right) \approx -1.2 \times 10^{-7} \qquad \text{(fixed-edge)}$$

$$\frac{1}{\langle O_{\mathbb{T}}\rangle}\log\left(\frac{\nu_{\mathbb{T},0_1}}{\nu_{\mathbb{T}}}\right) \approx -2.1 \times 10^{-5} \qquad \text{(fixed-span)}$$

$$\frac{1}{(L+1)(M+1)}\log\left(\frac{\nu^{\mathrm{H}}_{\mathbb{T},0_1}}{\nu^{\mathrm{H}}_{\mathbb{T}}}\right) \approx -8.9 \times 10^{-5} \qquad \text{(Hamiltonian)}$$

where $\langle O_{\mathbb{T}}\rangle$ is the average number of occupied vertices per span in the fixed-span model (see Section 3.4.1 for further explanation). The closer the ratios are to 1, the closer the log is to 0. Hence, we see that unknots are far less common in the fixed-span and Hamiltonian models than in the fixed-edge model.

This difference in knotting probability between models comes from how *dense* the polygons are in these models; that is the average number of edges per unit span. This quantity can be calculated directly from the transfer matrix (details in [20]). On average, fixed-edge SAPs are less dense than fixed-span SAPs, which are of course less dense than Hamiltonian SAPs. In general, a larger density means more edges, which means more opportunities to get tangled, which means a higher probability of knotting.

Another reason for using the fixed-span model over the fixed-edge model, is that when generating SAPs using transfer matrices (using the process outlined in Section 2.3.4), the polygons are generated by appending one span at each step. This almost always guarantees a valid polygon when the desired span is reached. However, if instead a desired length was required, there would be many more cases where a polygon could not be finished with the desired length. This causes wasted time and a decrease in efficiency, especially when sampling large span SAPs.

The downside to using the fixed-span model over the fixed-edge model is that a direct comparison to results outside of the tube may be difficult, since the enumeration there will likely be by length. However, as shown in Section 3.4.1, a comparison can still be made by calculating a rough estimation based on $\langle O_{\mathbb{T}}\rangle$.

3.2 Creating Transfer Matrices for Larger Tube Sizes

In my Master's thesis [20], numerical transfer matrix results were limited to the $L \times 1$ ($1 \leq L \leq 4$) and 2×2 tube sizes, and exact polygon generation results were limited to the 2×1 and 3×1 tube sizes. Now, both numerical calculations and polygon generation (exact and Monte Carlo) can be done in the $L \times 1$ ($1 \leq L \leq 5$) and $L \times 2$ ($2 \leq L \leq 3$) tube sizes. This was primarily made possible by storing the transfer matrices more efficiently by reducing the amount of information stored for each 1-pattern to the minimum required. This reduced the size of the transfer matrices and the amount of computer memory required.

Recall from Section 2.3.1 that in this thesis, each row and column of the transfer matrix represents a "proper 1-pattern". However, previously in my Master's thesis [20], each row and column instead represented a 1-block (defined in 2.3.1) with an assigned "ordering". The ordering was put on the half-edges in the 1-blocks and was used to encode connectivity between 1-blocks. However, this meant that all 1-blocks had multiple orderings, which resulted in a transfer matrix that was larger than what was needed.

Instead, now 1-patterns are used; recall from Section 2.3.1 that a 1-pattern is a 1-block along with "left-connectivity" information (instead of an ordering). This drastically reduced the size of the transfer matrix, since each proper 1-pattern corresponds to a 1-block with at least 2 orderings. Table 3.2 contains a comparison of the transfer matrix sizes when using 1-blocks with ordering versus 1-patterns.

3.3 Exact Results

Transfer matrices for SAPs and Hamiltonian SAPs were created for tube sizes $L \times 1, 1 \leq L \leq 5$, and $L \times 2$, $2 \leq L \leq 3$. Using the process outlined in Section 2.3.4, a complete set of all SAPs in these tube sizes of small span can be generated, limited by computational resources (memory and time). This was only done for tube sizes $2 \times 1, 3 \times 1, 4 \times 1$, and 2×2 due to the large memory and time restrictions of using the 5×1 and 3×2 transfer matrices (see Table A.1). Instead, the memory and computational time resources were dedicated to obtaining Monte Carlo results for these 5×1 and 3×2 tube sizes (Table A.1 in Appendix A contains

Table 3.2 An illustration of how using 1-patterns instead of 1-blocks with orderings reduced the number of rows/columns in the transfer matrices. In my master's thesis [20] 1-blocks with orderings were used, and in this thesis, 1-patterns are used instead. These numbers represent the number of rows/columns in the transfer matrices.

Tube Size	1-blocks with orderings	1-patterns
1×1	108	48
2×1	9,702	1,829
3×1	963,096	70,306
4×1	129,143,546	3,165,653
5×1		165,637,127
2×2	12,095,392	513,585
3×2		201,423,784

the required computational resources for each case).

After a complete set of all SAPs in a certain small tube size and span are generated, their knot-types were identified (explained in Section 2.4.3). The exact results for SAPs and Hamiltonian SAPs are displayed in Table 3.3 and Table 3.4 respectively. Note that all of these results are new since my Master's thesis [20] except for the Hamiltonian 2×1 and Hamiltonian 3×1 cases.

The exact counts of unknots (by span) can be used to calculate a lower bound on the fixed-span connective constant of unknots ($\chi_{\mathbb{T},0_1} = \log \nu_{\mathbb{T},0_1}$, as defined in Equation 3.9) as follows. We know from [55] that any two polygons (ω_1 and ω_2) in $\mathbb{T}$ can be concatenated (joined) to form a new polygon in $\mathbb{T}$ (a sketch of the proof is given earlier in Section 3.1.1). Since such a concatenation can be done within span 2, and since such a concatenation of two unknots results in another unknot, we have $p_{\mathbb{T}}(r;0_1)p_{\mathbb{T}}(s;0_1) \leq p_{\mathbb{T}}(r+s+2;0_1)$, or equivalently

$$\log p_{\mathbb{T}}(r-2;0_1) + \log p_{\mathbb{T}}(s-2;0_1) \leq \log p_{\mathbb{T}}(r+s-2;0_1).$$

Applying Fekete's lemma (see for example [57, Lemma 1.2.1]), we have

$$\chi_{\mathbb{T},0_1} = \lim_{s\to\infty} \frac{1}{s} \log p_{\mathbb{T}}(s-2;0_1) = \lim_{s\to\infty} \frac{a_s}{s} = \sup_{s\geq 2} \frac{a_s}{s} = \sup_{s\geq 2} \frac{1}{s} \log p_{\mathbb{T}}(s-2;0_1).$$

Thus, for any $s \geq 2$, $\frac{1}{s} \log p_{\mathbb{T}}(s-2;0_1)$ is a lower bound on $\chi_{\mathbb{T},0_1}$.

Table 3.3 Exact SAP generation results. All results are new since my Master's thesis [20]. Note that these results confirm the results from [27] about the minimum number of edges required to form a 3_1 and 4_1 knot in these tube sizes.

Tube	Span	Total	3_1^+	3_1^-	4_1
2×1	1	219	0	0	0
2×1	2	7,631	0	0	0
2×1	3	264,543	0	0	0
2×1	4	9,101,347	0	0	0
2×1	5	312,733,719	0	0	0
2×1	6	10,745,324,481	1,832	1,832	0
3×1	1	1,528	0	0	0
3×1	2	277,400	0	0	0
3×1	3	47,368,928	598	598	0
3×1	4	7,863,265,372	382,257	382,257	36
4×1	1	10,197	0	0	0
4×1	2	9,633,793	0	0	0
4×1	3	7,939,543,353	383,453	383,453	36
2×2	1	8,052	0	0	0
2×2	2	3,410,348	0	0	0
2×2	3	1,430,358,664	4,182	4,182	0

Table 3.4 Exact Hamiltonian SAP generation results. The 4×1 and 2×2 results are new since my Master's thesis [20]. Note that the 8_{19} knots generated here improve a previous upper bound on the minimum number of edges required for the 8_{19} in a 4×1 tube, calculated in [27] (improved from 52 to 50 edges).

Tube	Span	Total	3_1^+	3_1^-	4_1	5_1^+	5_1^-	5_2^+	5_2^-	6_1^+	6_1^-	$3_1^+\#3_1^-$	8_{19}	8_{19}^-
2×1	1	22	0	0	0	0	0	0	0	0	0	0	0	0
2×1	2	324	0	0	0	0	0	0	0	0	0	0	0	0
2×1	3	4,580	0	0	0	0	0	0	0	0	0	0	0	0
2×1	4	64,558	0	0	0	0	0	0	0	0	0	0	0	0
2×1	5	908,452	0	0	0	0	0	0	0	0	0	0	0	0
2×1	6	12,788,368	144	144	0	0	0	0	0	0	0	0	0	0
2×1	7	180,011,762	4,302	4,302	0	0	0	0	0	0	0	0	0	0
2×1	8	2,533,935,102	96,620	96,620	72	0	0	0	0	0	0	0	0	0
3×1	1	82	0	0	0	0	0	0	0	0	0	0	0	0
3×1	2	4,580	0	0	0	0	0	0	0	0	0	0	0	0
3×1	3	232,908	58	58	0	0	0	0	0	0	0	0	0	0
3×1	4	11,636,834	5,710	5,710	16	0	0	0	0	0	0	0	0	0
3×1	5	578,377,118	458,980	458,980	3,216	32	32	70	70	2	2	36	0	0
4×1	1	306	0	0	0	0	0	0	0	0	0	0	0	0
4×1	2	64,558	0	0	0	0	0	0	0	0	0	0	0	0
4×1	3	11,636,834	5,710	5,710	16	0	0	0	0	0	0	0	0	0
4×1	4	2,040,327,632	2,264,820	2,264,820	35,816	3,148	3,148	8	8	0	0	0	4	4
2×2	1	324	0	0	0	0	0	0	0	0	0	0	0	0
2×2	2	0	0	0	0	0	0	0	0	0	0	0	0	0
2×2	3	3,918,744	96	96	0	0	0	0	0	0	0	0	0	0
2×2	4	0	0	0	0	0	0	0	0	0	0	0	0	0

A similar lower bound can be obtained for Hamiltonian polygons. We know from [20] that any two Hamiltonian polygons in $\mathbb{T}$ can be concatenated using edges within span 3 to form a new Hamiltonian polygon in $\mathbb{T}$. See Figure 3.2 for an example of this concatenation. Following the same derivation as above, we have that for any $s \geq 3$, $\frac{1}{s}\log p^{\mathrm{H}}_{\mathbb{T}}(s-3;0_1)$ is a lower bound on $\chi^{\mathrm{H}}_{\mathbb{T},0_1}$ (as defined in Equation 3.10). Using the exactly enumerated polygons, Table 3.5 contains the maximum values of $\frac{1}{s}\log p_{\mathbb{T}}(s-2;0_1)$ and $\frac{1}{s}\log p^{\mathrm{H}}_{\mathbb{T}}(s-2;0_1)$ seen, for different tube sizes. Note that comparisons between these values should not be made, since the maximal span of the polygons generated varied between tube sizes. Also note that the lower bound estimates for the growth rate of all and Hamiltonian polygons ($\chi_{\mathbb{T}}$ and $\chi^{\mathrm{H}}_{\mathbb{T}}$) obtained using the same technique (maximum values of $\frac{1}{s}\log p_{\mathbb{T}}(s-2)$ and $\frac{1}{s}\log p^{\mathrm{H}}_{\mathbb{T}}(s-2)$) are the same as those for the unknot, at least up to ten significant figures, in all the cases shown here (although the actual quantities are different).

Although these lower bound estimates are not close to the actual growth rates calculated directly from the transfer matrix, the unknot counts have proven useful for obtaining a "pattern theorem" for unknots in the 2×1 tube [5]. Specifically, this lower bound on the growth rate of unknots is strictly larger than an upper bound estimate (obtained via the transfer matrix) on the growth rate of polygons which have no "2-sections". Hence, since the set of unknot polygons without 2-sections is a subset of the set of all polygons without 2-sections, it follows that all but exponentially few unknot polygons (in the 2×1 tube) contain 2-sections. This result, along with showing that unknots also contain a non-zero density of 2-sections [5], yields a pattern theorem for unknots in the 2×1 tube.

Note that exact enumeration is limited to these small span cases due to computational resources. Since we are interested in the asymptotics of $p_{\mathbb{T}}(s;K)$, we turn to Monte Carlo techniques to examine large span SAPs. This is discussed in the next section.

3.4 Monte Carlo Results

The Monte Carlo method used here is outlined in Section 2.3.4 and uses the generated transfer matrices to sample independent large span SAPs uniformly (each SAP of a given span is equally likely) at random. A summary table of Monte Carlo results for SAP knot-

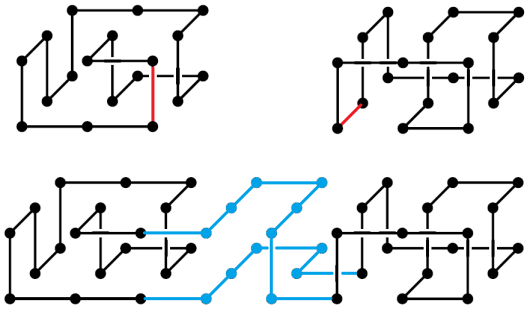

Figure 3.2: An example of concatenating two Hamiltonian polygons in the 2×1 tube. The red edges are removed and the blue edges join the polygons while adding a span of 2.

Table 3.5 The maximal values observed of the sequences $\frac{1}{s}\log p_{\mathbb{T}}(s-2;0_1)$ and $\frac{1}{s}\log p^{\mathrm{H}}_{\mathbb{T}}(s-2;0_1)$ from the exact generation of polygons, in different tube sizes. These values serve as lower bounds on $\chi_{\mathbb{T},0_1}$ and $\chi^{\mathrm{H}}_{\mathbb{T},0_1}$, respectively. Note that comparisons between these values should not be made, since the maximal span polygons generated varied between tube sizes. Error is confined to the last digit.

Tube Size	$\max_s(\frac{1}{s}\log p_{\mathbb{T}}(s-2;0_1))$	$\max_s(\frac{1}{s}\log p^{\mathrm{H}}_{\mathbb{T}}(s-2;0_1))$
2x1	2.670655	1.714937
3x1	3.133304	1.685891
4x1	3.076616	1.430896
2x2	2.997892	2.530205

types can be seen in Appendix C in Table C.1 (all) and Table C.2 (Hamiltonian). These samples are used to provide evidence for Equation 3.9: the conjecture that the number of polygons in $\mathbb{T}$ with span-s and knot-type K has the asymptotic form:

$$p_{\mathbb{T}}(s;K) \sim D_{\mathbb{T},K}\nu_{\mathbb{T},0_1}^s s^{f_K}, \qquad \text{as} \quad s \to \infty, \tag{3.11}$$

where $D_{\mathbb{T},K}$ is a constant, f_K is the number of prime knot factors in the prime knot decomposition of K with $f_{0_1} = 0$, and $\nu_{\mathbb{T},0_1}$ is the growth rate (by span) for unknots in $\mathbb{T}$, with $\nu_{\mathbb{T},0_1} = \nu_{\mathbb{T},K}$ for any knot-type K (conjectured).

3.4.1 Evidence that the asymptotic form holds for the unknot, and estimates for the difference between the growth rates of unknots and all SAPs

First note that all of this Monte Carlo work is new since my Master's thesis [20]. For the tube sizes 2×1 and 3×1, the results are published in [12]. This section will focus on the newer results for the $4 \times 1, 5 \times 1, 2 \times 2$, and 3×2 tube sizes.

Recall that the growth rate for all SAPs ($\nu_{\mathbb{T}}$) can be calculated directly from the eigenvectors and eigenvalues of the transfer matrix (Table 3.1). To obtain estimates for the growth rate of unknots ($\nu_{\mathbb{T},0_1}$), recall $p_{\mathbb{T}}(s) \sim D_{\mathbb{T}}\nu_{\mathbb{T}}^s$, and let $\mathbb{P}_{\mathbb{T},s}(K) = \frac{p_{\mathbb{T}}(s;K)}{p_{\mathbb{T}}(s)}$ be the probability that a span-s SAP in $\mathbb{T}$ has knot-type K. If $p_{\mathbb{T}}(s;0_1) \sim D_{\mathbb{T},0_1}\nu_{\mathbb{T},0_1}^s$ as conjectured, then we have the form:

$$\log \mathbb{P}_{\mathbb{T},s}(0_1) \sim D + s \log\left(\frac{\nu_{\mathbb{T},0_1}}{\nu_{\mathbb{T}}}\right), \qquad \text{as} \quad s \to \infty,$$

with constant $D = \log \frac{D_{\mathbb{T},0_1}}{D_{\mathbb{T}}}$.

Equivalently for Hamiltonian SAPs, $\nu_{\mathbb{T}}^{\mathrm{H}}$ can be calculated from the Hamiltonian transfer matrix (Table 3.1), and if we let $\mathbb{P}_{\mathbb{T},s}^{\mathrm{H}}(K) = \frac{p_{\mathbb{T}}^{\mathrm{H}}(s;K)}{p_{\mathbb{T}}^{\mathrm{H}}(s)}$, we have the conjectured form:

$$\log \mathbb{P}_{\mathbb{T},s}^{\mathrm{H}}(0_1) \sim D^{\mathrm{H}} + s \log\left(\frac{\nu_{\mathbb{T},0_1}^{\mathrm{H}}}{\nu_{\mathbb{T}}^{\mathrm{H}}}\right), \qquad \text{as} \quad s \to \infty,$$

with constant $D^{\mathrm{H}} = \log \frac{D_{\mathbb{T},0_1}^{\mathrm{H}}}{D_{\mathbb{T}}^{\mathrm{H}}}$.

In Figure 3.3, we plot $\log \mathbb{P}_{\mathbb{T},s}(0_1)$ and $\log \mathbb{P}_{\mathbb{T},s}^{\mathrm{H}}(0_1)$ against span-s from the Monte Carlo data and fit it with a best fit line for tube sizes $2 \times 2, 4 \times 1, 5 \times 1$, and 3×2. From the

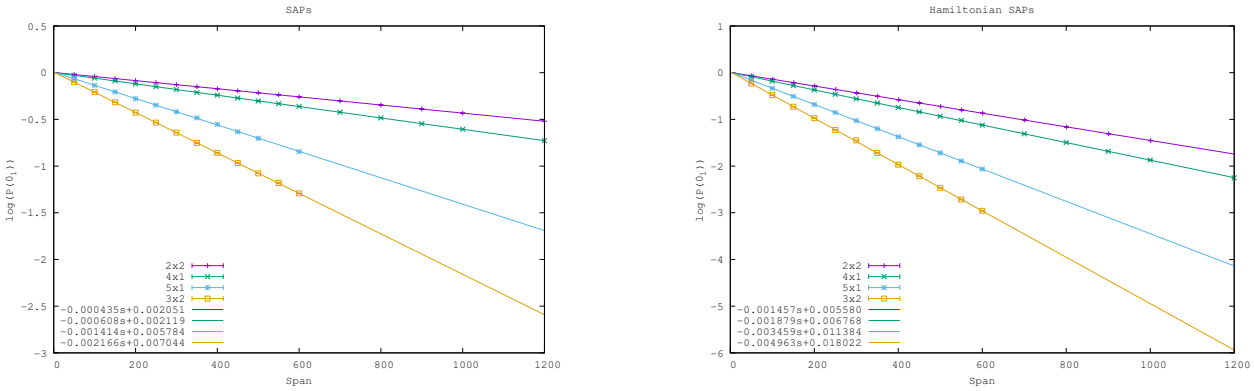

(a) **(b)**

Figure 3.3: Plots of (a) $\log \mathbb{P}_{\mathbb{T},s}(0_1)$ and (b) $\log \mathbb{P}^{\mathrm{H}}_{\mathbb{T},s}(0_1)$ against s (span) for the tubes $\mathbb{T} = 2 \times 2, 4 \times 1, 5 \times 1, 3 \times 2$, together with linear best fits. Error bars indicate 95% confidence intervals.

Table 3.6 Linear best-fit estimates for $\log \mathbb{P}_{\mathbb{T},s}(0_1) \sim as + b$ and $\log \mathbb{P}^{\mathrm{H}}_{\mathbb{T},s}(0_1) \sim a^{\mathrm{H}}s + b^{\mathrm{H}}$.

Tube	a (error)	b (error)	a^{H} (error)	b^{H} (error)
2×2	-0.000434987 (3.369×10^{-7})	0.00205085 (0.000202)	-0.00145658 (1.03×10^{-6})	0.00557983 (0.0005513)
4×1	-0.000608242 (5.47×10^{-7})	0.00211878 (0.0003251)	-0.00187919 (1.541×10^{-6})	0.00676831 (0.0009161)
5×1	-0.00141351 (5.441×10^{-6})	0.00578379 (0.001887)	-0.00345904 (1.563×10^{-6})	0.0113844 (0.000575)
3×2	-0.00216574 (2.147×10^{-6})	0.00704401 (0.0007902)	-0.00496299 (1.26×10^{-5})	0.0180222 (0.004638)

plots, we can see the linear fit is good for all cases (reduced chi-squared statistic $< 10^{-4}$), which indicates the form of Equation 3.9 is correct for the unknot. Therefore, we conclude that $\log \mathbb{P}(0_1) \sim as + b$ and $\log \mathbb{P}(0_1) \sim a^{\mathrm{H}}s + b^{\mathrm{H}}$, where estimates for a, b, a^{H}, and b^{H} are given in Table 3.6. The errors denote the asymptotic standard error reported by the software gnuplot [76] using a least squares fit. Using the slopes of these best fit lines (Table 3.6) along with the growth rates of SAPs (Table 3.1), estimates for the growth rates of the unknot are calculated (Table 3.7).

The differences between $\nu_{\mathbb{T}}$ and $\nu_{\mathbb{T},0_1}$ (and $\nu^{\mathrm{H}}_{\mathbb{T}}$ and $\nu^{\mathrm{H}}_{\mathbb{T},0_1}$) can be compared to best estimates for the cubic lattice with no tube constraint. It is estimated in [68] that the difference between the growth rate (by length) of unknots and all SAPs is:

$$\log \frac{\mu_{0_1}}{\mu} = (-4.15 \pm 0.32) \times 10^{-6}.$$

Notice that the growth rates calculated in this thesis via the Monte Carlo results are for span, not length. But for Hamiltonian SAPs, length is completely determined by span, so

Table 3.7 Estimates of the growth rate of the unknot (0_1). Error is expected to be confined to the last digit.

Tube	$\nu_{\mathbb{T},0_1}$	$\nu^{\mathrm{H}}_{\mathbb{T},0_1}$
2×2	416.688865	104.3368934
4×1	770.4583692	172.3902216
5×1	3557.878712	594.4175928
3×2	4935.164585	876.1998427

Table 3.8 Values for $\langle O_{\mathbb{T}} \rangle$, the average number of occupied vertices per span. These averages can be calculated directly from the transfer matrix. Error is expected to be confined to the last digit.

$\mathbb{T}$	$\langle O_{\mathbb{T}} \rangle$
2×1	4.871382
3×1	5.355162
4×1	5.736078
5×1	6.053739
2×2	5.593681
3×2	6.132268

using the relationship between number of edges n and span-s, $n = (L+1)(M+1)(s+1)$, we have:

$$\log \frac{\mu^{\mathrm{H}}_{\mathbb{T},0_1}}{\mu^{\mathrm{H}}_{\mathbb{T}}} = \frac{1}{(L+1)(M+1)} \log \frac{\nu^{\mathrm{H}}_{\mathbb{T},0_1}}{\nu^{\mathrm{H}}_{\mathbb{T}}}.$$

For SAPs from the fixed-span model, the lengths are not fixed, so we cannot make a direct comparison. However, we can use an approximation based on the average number of occupied vertices per span $\langle O_{\mathbb{T}} \rangle$. This average can be calculated from the transfer matrix (details in [20]). Table 3.8 contains the values calculated for $\langle O_{\mathbb{T}} \rangle$. Thus an approximate difference between the growth rates by length in $\mathbb{T}$ ($\mu_{\mathbb{T}}$ and $\mu_{\mathbb{T},0_1}$) is:

$$\log \frac{\mu_{\mathbb{T},0_1}}{\mu_{\mathbb{T}}} \approx \frac{1}{\langle O_{\mathbb{T}} \rangle} \log \frac{\nu_{\mathbb{T},0_1}}{\nu_{\mathbb{T}}}.$$

Table 3.9 contains the estimated differences $\log \dfrac{\mu_{\mathbb{T},0_1}}{\mu_{\mathbb{T}}}$ and $\log \dfrac{\mu^{\mathrm{H}}_{\mathbb{T},0_1}}{\mu^{\mathrm{H}}_{\mathbb{T}}}$. The 2×1 and 3×1 estimates are from [12]. Notice that for all of the cases except for the 2×1 tube, knots are

Table 3.9 Comparing the estimated difference in growth rates (by length) of all SAPs and unknots, to the difference estimated in [68] with no tube restraint: $\log \mu_{0_1}/\mu = -4.15 \times 10^{-6}$. Note that $\approx \log \mu_{\mathbb{T},0_1}/\mu_{\mathbb{T}}$ is a rough approximation based on the average number of occupied vertices per span. Since these are rough approximations, no attempt at stating errors is made. The 2×1 and 3×1 numbers are from [12].

Tube	$\approx \log \frac{\mu_{\mathbb{T},0_1}}{\mu_{\mathbb{T}}}$	$\approx \log \frac{\mu^{\mathrm{H}}_{\mathbb{T},0_1}}{\mu^{\mathrm{H}}_{\mathbb{T}}}$
2×1	-1.66×10^{-7}	-4.78×10^{-6}
3×1	-2.15×10^{-5}	-8.92×10^{-5}
4×1	-1.06×10^{-4}	-1.88×10^{-4}
5×1	-2.33×10^{-4}	-2.88×10^{-4}
2×2	-7.78×10^{-5}	-1.62×10^{-4}
3×2	-3.53×10^{-4}	-4.10×10^{-4}

more common (in the sense that the knotting probability goes to 1 faster as SAP length goes to infinity) than for all for all SAPs on the cubic lattice with no tube constraint (using the estimate in [68] for the knotting probability growth rate).

Also note that if $\mathbb{T}_{L \times M}$ is a subtube of a larger tube, the knots are less common in the subtube, but it is interesting to compare non-overlapping tubes. Notice from Table 3.9 that knots are less likely in 3×1 than 2×2, but more common in 4×1 than 2×2. Also notice that for two tubes with the same amount of hinge vertices (12), Table 3.9 shows that knots are less likely in 5×1 (a more flat tube) than 3×2 (a more symmetrical tube). This is to be expected as there are more opportunities for crossings to occur. Note that there is also one more hinge edge in the 3×2 tube than the 5×1 tube (17 edges compared to 16).

The clear linear relationships seen in Figure 3.3 indicate that the conjectured asymptotic form in Equation 3.9 holds for the unknot. Next, evidence is provided that this form also holds for any knot-type K.

3.4.2 Evidence that the asymptotic form holds for other knot-types and that the growth rate of the unknot is equal to that of any knot-type

In the previous subsection, evidence indicated that Equation 3.9 holds for the unknot: $p_{\mathbb{T}}(s;0_1) \sim D_{\mathbb{T},0_1}\nu_{\mathbb{T},0_1}^s$. In this subsection we provide evidence that Equation 3.9 holds for any knot-type K. Consider a prime knot K_*, where $f_{K_*} = 1$. If Equation 3.9 holds, then $p_{\mathbb{T}}(s;K_*) \sim D_{\mathbb{T},K_*}\nu_{\mathbb{T},K_*}^s s$, giving the conjectured asymptotic form for the ratio

$$\frac{\mathbb{P}_{\mathbb{T},s}(K_*)}{\mathbb{P}_{\mathbb{T},s}(0_1)} \sim \frac{D_{\mathbb{T},K_*}}{D_{\mathbb{T},0_1}} s \left(\frac{\nu_{\mathbb{T},K_*}}{\nu_{\mathbb{T},0_1}}\right)^s, \qquad \text{as} \quad s \to \infty.$$

The equivalent ratio for Hamiltonian SAPs is conjectured to have the following asymptotic form

$$\frac{\mathbb{P}^{\mathrm{H}}_{\mathbb{T},s}(K_*)}{\mathbb{P}^{\mathrm{H}}_{\mathbb{T},s}(0_1)} \sim \frac{D^{\mathrm{H}}_{\mathbb{T},K_*}}{D^{\mathrm{H}}_{\mathbb{T},0_1}} s \left(\frac{\nu^{\mathrm{H}}_{\mathbb{T},K_*}}{\nu^{\mathrm{H}}_{\mathbb{T},0_1}}\right)^s, \qquad \text{as} \quad s \to \infty.$$

These ratios are plotted in Figures 3.4 (all) and 3.5 (Hamiltonian) for various prime knots, scaled by constants to be visible in the same plot. The linear forms of the plots indicate that for these prime knot-types, the form in Equation 3.9 holds with $\nu_{\mathbb{T},K_*} = \nu_{\mathbb{T},0_1}$ and $\nu^{\mathrm{H}}_{\mathbb{T},K_*} = \nu^{\mathrm{H}}_{\mathbb{T},0_1}$.

More generally, to examine if Equation 3.9 holds for SAPs with knot-type K consisting of f_K-factors, Figures 3.6 (all) and 3.7 (Hamiltonian) contain log-log plots of the probabilities of multiple factor knots, again divided by the probability of the unknot. If Equation 3.9 holds, then the log of this ratio will have the form

$$\log \frac{\mathbb{P}_{\mathbb{T},s}(K)}{\mathbb{P}_{\mathbb{T},s}(0_1)} \sim \log\left(\frac{D_{\mathbb{T},K}}{D_{\mathbb{T},0_1}}\right) + s \log\left(\frac{\nu_{\mathbb{T},K}}{\nu_{\mathbb{T},0_1}}\right) + f_K \log s, \qquad \text{as} \quad s \to \infty,$$

and for Hamiltonian SAPs

$$\log \frac{\mathbb{P}^{\mathrm{H}}_{\mathbb{T},s}(K)}{\mathbb{P}^{\mathrm{H}}_{\mathbb{T},s}(0_1)} \sim \log\left(\frac{D^{\mathrm{H}}_{\mathbb{T},K}}{D^{\mathrm{H}}_{\mathbb{T},0_1}}\right) + s \log\left(\frac{\nu^{\mathrm{H}}_{\mathbb{T},K}}{\nu^{\mathrm{H}}_{\mathbb{T},0_1}}\right) + f_K \log s, \qquad \text{as} \quad s \to \infty.$$

Again, the linear forms of all these log-log plots indicate that the form in Equation 3.9 holds, and that $\nu_{\mathbb{T},K} = \nu_{\mathbb{T},0_1}$ and $\nu^{\mathrm{H}}_{\mathbb{T},K} = \nu^{\mathrm{H}}_{\mathbb{T},0_1}$. Furthermore, the slope of the lines for the f_K-factor knots is close to f_K, providing further evidence of the correctness of Equation 3.9.

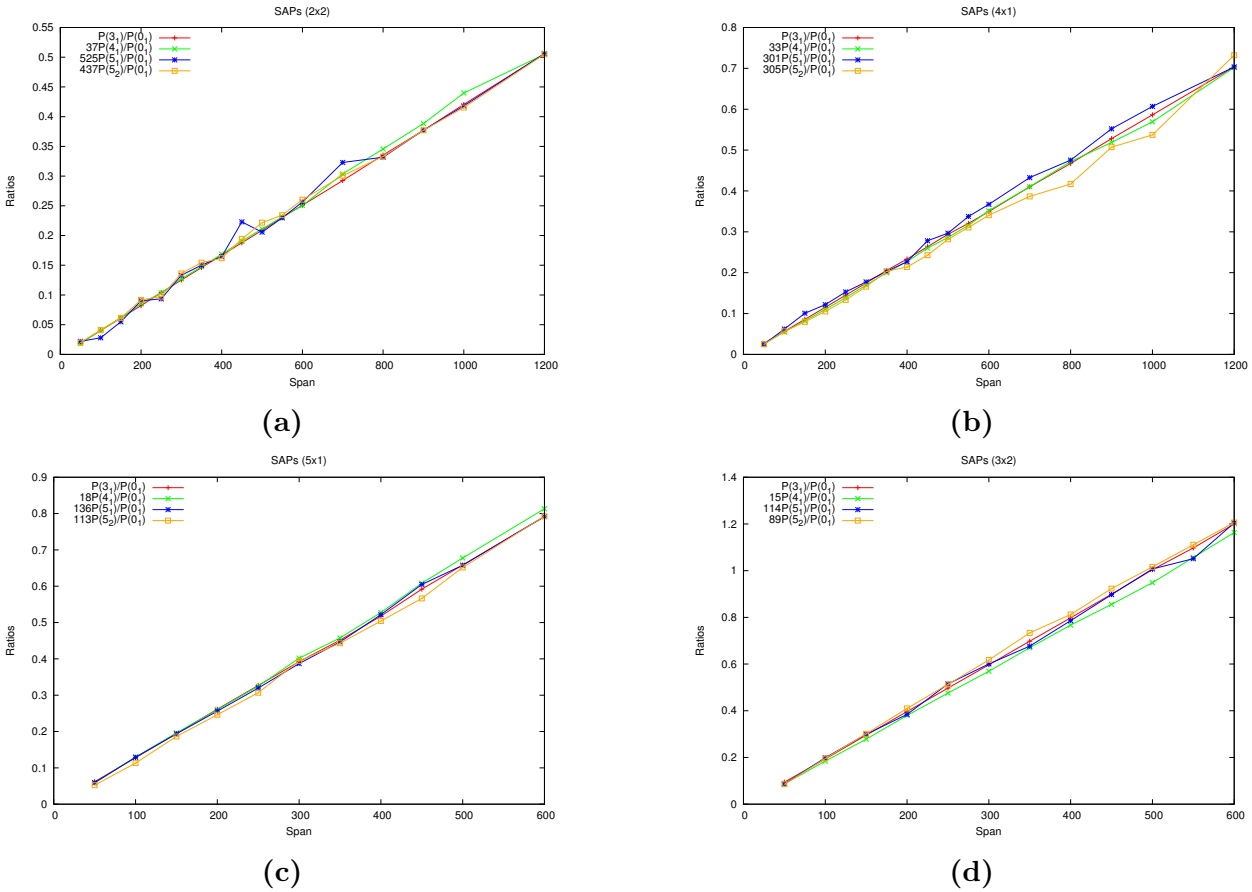

Figure 3.4: Plots of the ratio $\mathbb{P}_{\mathbb{T},s}(K_*)/\mathbb{P}_{\mathbb{T},s}(0_1)$ for $K_* = 3_1$ (red), 4_1 (green), 5_1 (blue), 5_2 (orange), scaled by a constant factor for clarity, against s (span), for tube sizes (a) 2×2, (b) 4×1, (c) 5×1, and (d) 3×2.

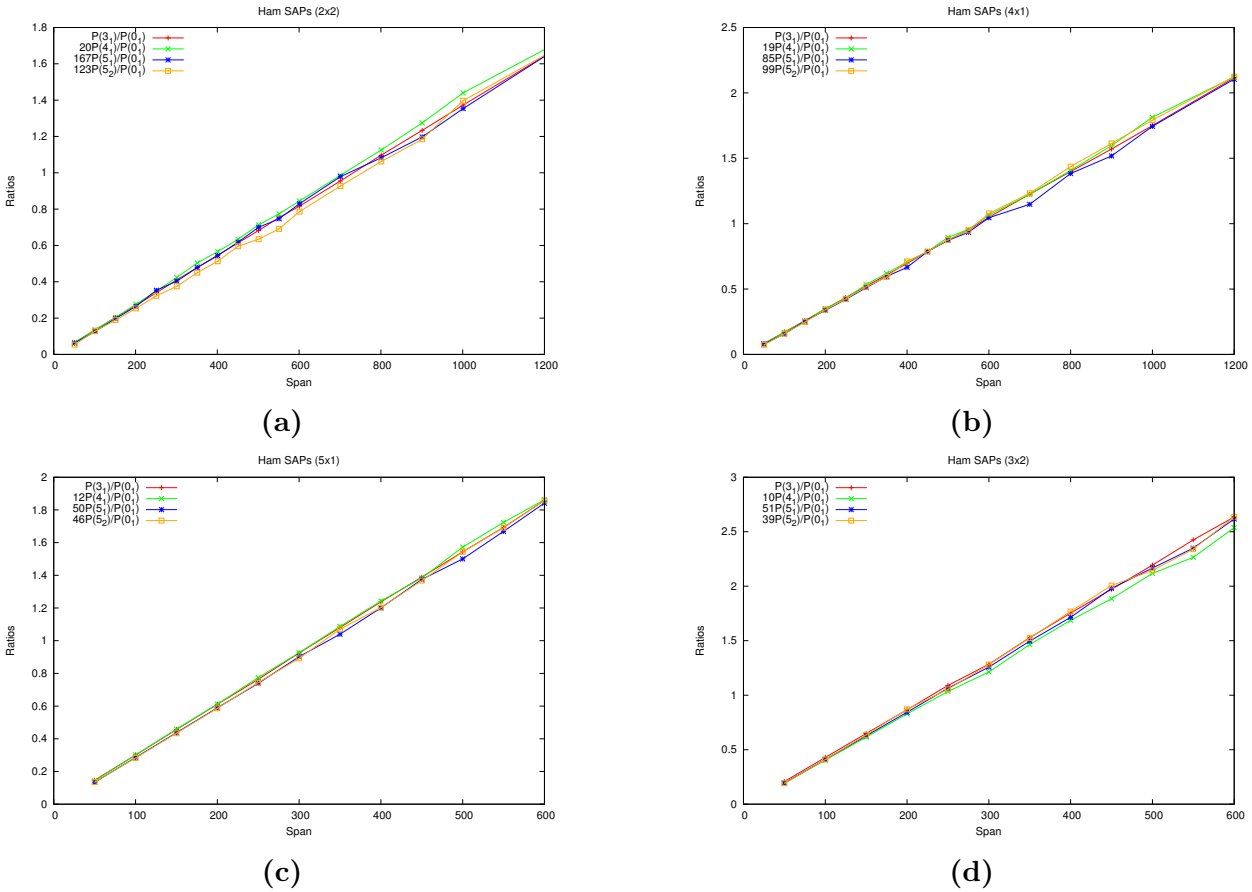

Figure 3.5: Plots of the ratio $\mathbb{P}^{\mathrm{H}}_{\mathbb{T},s}(K_*)/\mathbb{P}^{\mathrm{H}}_{\mathbb{T},s}(0_1)$ for $K_* = 3_1$ (red), 4_1 (green), 5_1 (blue), 5_2 (orange), scaled by a constant factor for clarity, against s (span), for tube sizes (a) 2×2, (b) 4×1, (c) 5×1, and (d) 3×2.

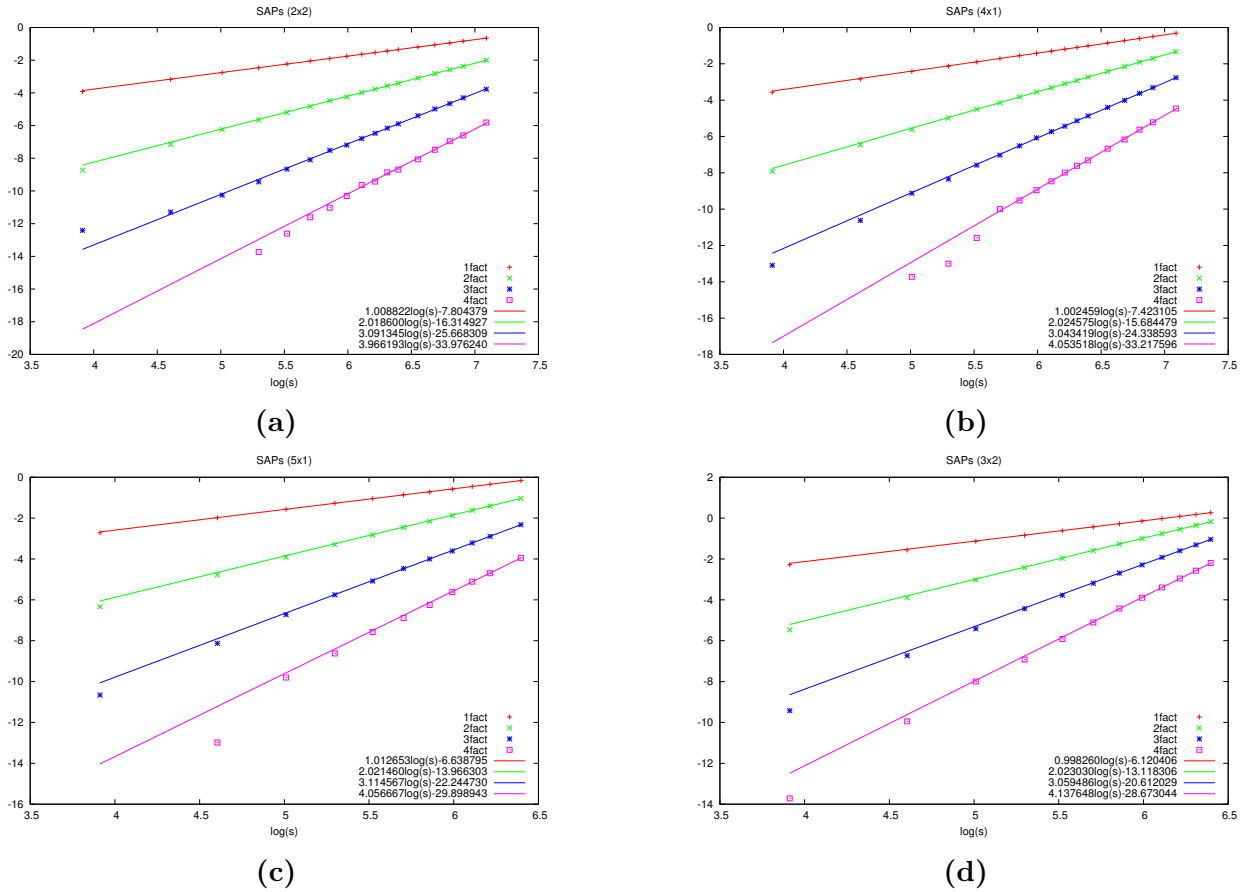

Figure 3.6: Log-log plots of $\mathbb{P}_{\mathbb{T},s}(f_K \text{ factor knot})/\mathbb{P}_{\mathbb{T},s}(0_1)$ for $f_K = 1$ (red), 2 (green), 3 (blue), 4 (pink), together with straight line fits for spans $s \geq 400$, for tube sizes (a) 2×2, (b) 4×1, (c) 5×1, and (d) 3×2.

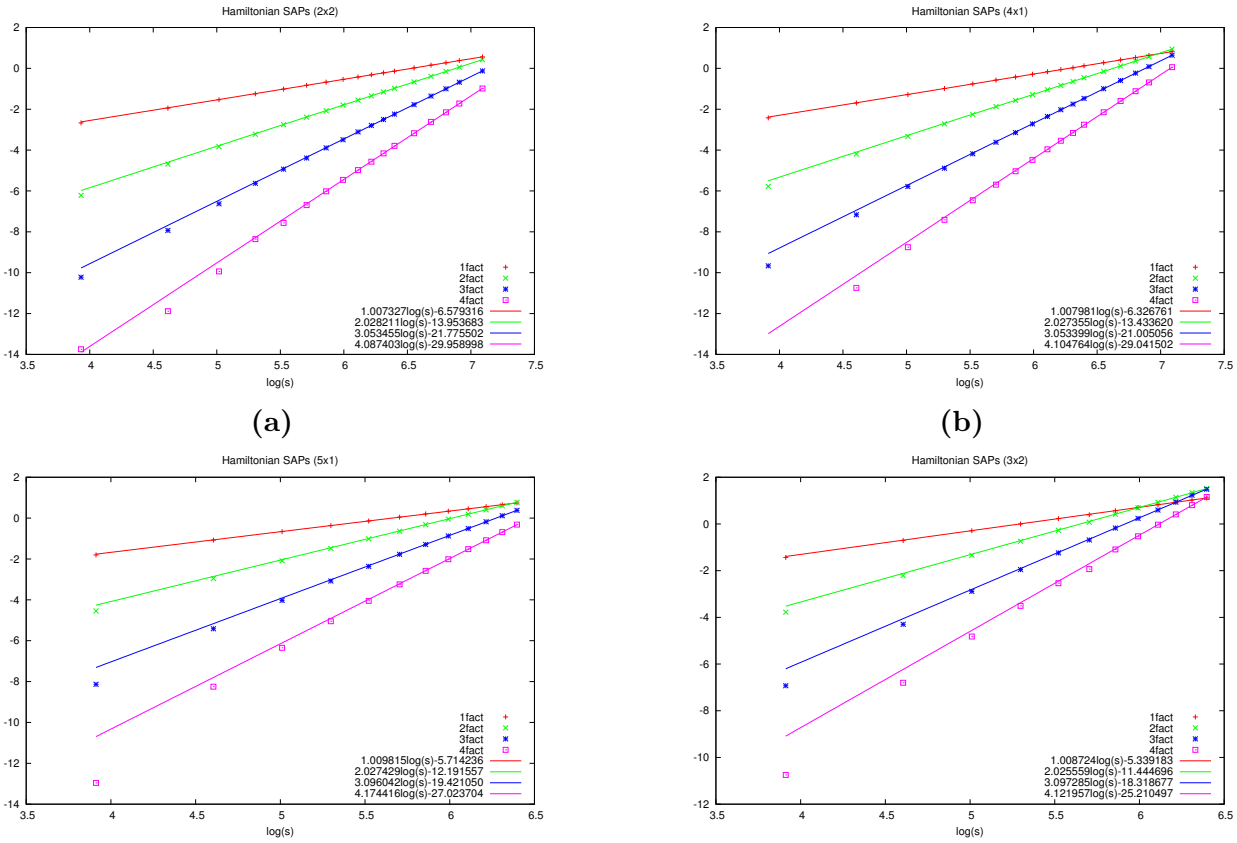

Figure 3.7: Log-log plots of $\mathbb{P}^{\mathrm{H}}_{\mathbb{T},s}(f_K \text{ factor knot})/\mathbb{P}^{\mathrm{H}}_{\mathbb{T},s}(0_1)$ for $f_K = 1$ (red), 2 (green), 3 (blue), 4 (pink), together with straight line fits for spans $s \geq 400$, for tube sizes (a) 2×2, (b) 4×1, (c) 5×1, and (d) 3×2.

Table 3.10 Approximate values for $M_{\mathbb{T}}(K)$ and $M_{\mathbb{T}}^{\mathrm{H}}(K)$ from Equations 3.12 and 3.13. These values represent a rough estimate of the span where knots with f_K factors have the highest probability.

Tube Size	Approx. $M_{\mathbb{T}}(K)$	Approx. $M_{\mathbb{T}}^{\mathrm{H}}(K)$
2x2	$2300 f_K$	$687 f_K$
4x1	$1640 f_K$	$532 f_K$
5x1	$707 f_K$	$289 f_K$
3x2	$462 f_K$	$201 f_K$

With evidence that

$$\mathbb{P}_{\mathbb{T},s}(K) \sim D_{\mathbb{T},K} \left(\frac{\nu_{\mathbb{T},0_1}}{\nu_{\mathbb{T}}} \right)^s s^{f_K}, \qquad \text{as} \quad s \to \infty$$

and

$$\mathbb{P}_{\mathbb{T},s}^{\mathrm{H}}(K) \sim D_{\mathbb{T},K}^{\mathrm{H}} \left(\frac{\nu_{\mathbb{T},0_1}^{\mathrm{H}}}{\nu_{\mathbb{T}}^{\mathrm{H}}} \right)^s s^{f_K}, \qquad \text{as} \quad s \to \infty,$$

note that these probabilities (respectively) have a maximum at approximately

$$M_{\mathbb{T}}(K) \approx -\frac{f_K}{\log\left(\frac{\nu_{\mathbb{T},0_1}}{\nu_{\mathbb{T}}}\right)} \tag{3.12}$$

and

$$M_{\mathbb{T}}^{\mathrm{H}}(K) \approx -\frac{f_K}{\log\left(\frac{\nu_{\mathbb{T},0_1}^{\mathrm{H}}}{\nu_{\mathbb{T}}^{\mathrm{H}}}\right)}. \tag{3.13}$$

Notice that the terms on the right hand sides do not depend on the knot-type K, only the number of factors in its decomposition f_K. However, the exact values of $M_{\mathbb{T}}(K)$ and $M_{\mathbb{T}}^{\mathrm{H}}(K)$ can depend on K; in particular, the minimum span needed to create K can affect $M_{\mathbb{T}}(K)$ and $M_{\mathbb{T}}^{\mathrm{H}}(K)$ (i.e. if approximate values of $M_{\mathbb{T}}(K)$ or $M_{\mathbb{T}}^{\mathrm{H}}(K)$ are less than the minimum span of K). Table 3.10 contains approximated values of $M_{\mathbb{T}}(K)$ and $M_{\mathbb{T}}^{\mathrm{H}}(K)$. In Figure 3.8, $\mathbb{P}_{\mathbb{T},s}^{\mathrm{H}}(f_K)$ is plotted for $f_K = 1, 2, 3, 4$. Only the Hamiltonian plot is shown here since only for these can some maxima be easily seen in the spans that were sampled.

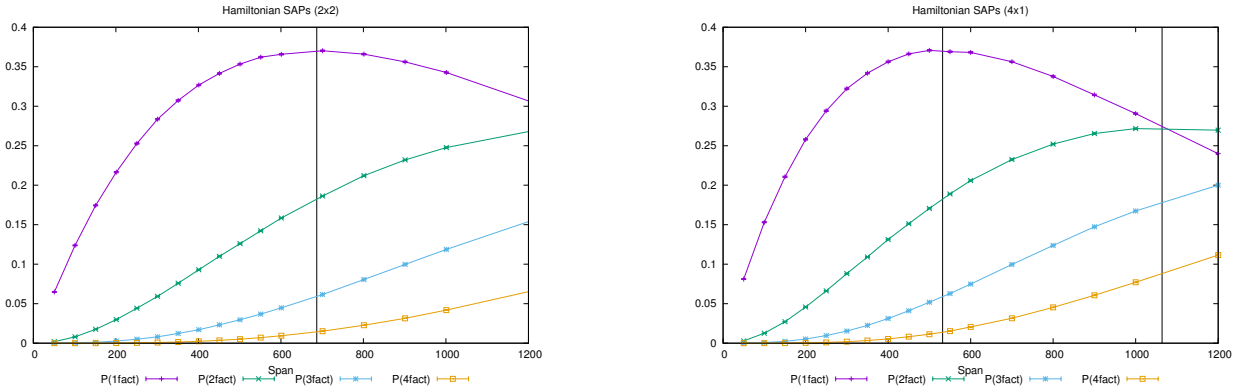

(a)

(b)

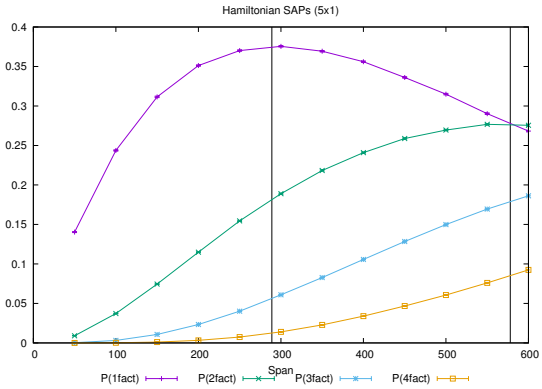

(c)

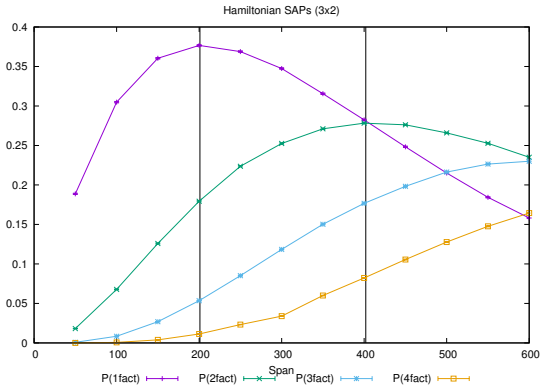

(d)

Figure 3.8: Plots of $\mathbb{P}^{\mathrm{H}}_{\mathbb{T},s}(f_K)$ against s (span) for $f_K = 1$ (purple), 2 (green), 3 (blue), 4 (orange), for tube sizes (a) 2×2, (b) 4×1, (c) 5×1, and (d) 3×2. The black vertical lines indicate approximate locations of maxima ($M^{\mathrm{H}}_{\mathbb{T}}(K)$) from Table 3.10. Error bars indicate 95% confidence intervals.

3.5 Monte Carlo Results Regarding Two Modes of Knotting

The results presented in this section are an extension of the Monte Carlo work done in [10] to larger tube sizes. Note that the work published in [10] is also part of my PhD work.

There are many ways to measure the "size" of the knotted part of a knot, or the "localization" of the knotted part of a knot. When one measures the size of the knotted part according to the size of the region in which the crossings are concentrated, then the configurations shown in Figures 3.9(a) and 3.9(b) correspond to examples of "local" or "tight" knotting. We will call this "knot localization". However, using another standard measure for determining knot-size, namely using the length of a smallest knotted subarc, leads to characterizing Figure 3.9(a) as a "non-local" knotting mode and Figure 3.9(b) as a "local" knotting mode. To help visualize why this is the case, knotted subarcs are drawn with a solid line in Figures 3.9(c) and 3.9(d). Note the difference between knot localization and the two modes of knotting, the local mode and non-local mode. These two modes will be defined precisely in Section 3.5.1.

Also note that since subarcs are not closed, they are not topologically knotted. So in order to call a subarc knotted, there must be some closure scheme applied to the subarc. Also since subarcs are not closed, it is not always clear how to define a knotted subarc. How much of the arc is considered "knotted"? We define knotted arcs and use a closure scheme specific for knots in a tube (defined shortly), but in general, there are different ways to define knotted arcs, and there are different closure schemes which can be applied. Note that depending on how knotted arcs are defined and which closure scheme is applied, the knot-type of the arc can change. The work in [65] studies knotted subarcs and different arc closure schemes.

Using the two modes (local and non-local), the results in [10] indicated that the non-local mode of knotting is more likely than the local mode of knotting in the 2×1 and 3×1 tubes. The sampled Monte Carlo polygons generated in this thesis in larger tube sizes are used to examine these two modes of knotting further. Note that these two modes have been observed in non-equilibrium simulation experiments [59], and it is unclear which is more

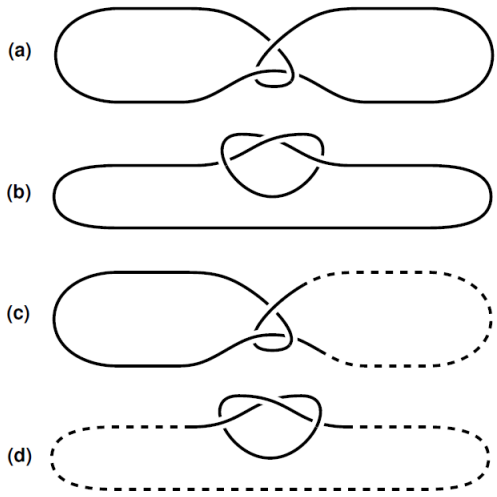

Figure 3.9: An illustration of (a) a non-local mode trefoil and (b) a local mode trefoil. The "knotted part" of (a) is drawn with a solid line in (c). Similarly, the "knotted part" of (b) is drawn with a solid line in (d). Notice how the knotted part in (c) is relatively much larger when compared to its polygon size, than the knotted part in (d) when it is compared to its polygon size.

likely. Studying which is more likely in our equilibrium model is expected to add insight into the experiments.

Without the tube constraint, it is generally accepted that the local mode of knotting is more common than non-local mode of knotting. However, simulations of knotting in fully confined volumes suggest that once a full spatial constraint is imposed, the non-local mode of knotting becomes more common [36]. For partially confined spaces, where two spatial dimensions are restricted but not the third (such as a tube), recent simulations and experimental studies have indicated that local knotting dominates [38, 39, 44, 59] (unlike when all three spatial dimensions are restricted). For polygons confined to a lattice tube, it is shown in [10] that all but few sufficiently long polygons are non-locally knotted. For more details regarding the local and non-local modes of knotting, please see [10].

3.5.1 Defining the Local and Non-local Modes of Knot Patterns for SAPs in a Tube

For SAPs in a tube, the local and non-local modes of knotting are defined as follows (from [10]). But first, some definitions must be introduced. Let ω be a polygon in $\mathbb{T}$ with span-s. Thus ω is embedded in $\mathbb{T}$ between the planes $x = 0$ and $x = s$. For half-integers $k \in \mathbb{Z} + \frac{1}{2}$ with $0 < k < s$, recall from Section 2.4.3 that ω has a *2-section* at $x = k$ if the plane $x = k$ intersects ω at exactly two points. If ω has m 2-sections, let $t(\omega) = (t_1, \ldots, t_m)$ be the (ordered) set of x-values at which they occur. Clearly $m \leq s$; if $m = 0$ then $t(\omega)$ is empty.

The 2-sections of a polygon ω in $\mathbb{T}$ naturally partition it into a sequence of "segments". Moreover, if ω has prime knot-type, then typically the segment of ω which contains the "knotted part" will lie between two successive 2-sections. It is this idea which will allow us to locate, measure, and classify knot components within polygons in $\mathbb{T}$.

Take ω in $\mathbb{T}$ with $m \geq 2$. The 2-sections of ω partition it into a sequence of segments that we call *connect-sum patterns* (*cs-patterns* for short). Then for any $1 \leq i < m$, the segment of ω between $x = t_i$ and $x = t_{i+1}$ is called a *proper* cs-pattern of ω. If $m \geq 1$ then the segment of ω between $x = 0$ and $x = t_1$ is called the *start* cs-pattern of ω; likewise, the segment of ω between $x = t_m$ and $x = s(\omega)$ is called the *end* cs-pattern of ω.

Any proper cs-pattern σ (between $x = t_i$ and $x = t_{i+1}$, for some $i \geq 1$) is the union of two "strands" (self-avoiding walks) σ_1 and σ_2, each extending from the left end of the pattern to the right. On the left side of the plane $x = t_i$, joining the two left ends of σ_1 and σ_2 to each other and then, on the right side of the plane $x = t_{i+1}$, joining their two right ends to each other, yields the *denominator closure* of the cs-pattern. See Figure 3.10(a). *Note here that if the overall polygon has knot-type K and one of its proper cs-patterns has denominator closure of knot-type K', then K' must be part of the knot-decomposition of K.* Let $DC(\sigma)$ be the knot-type of the denominator closure of σ. If $DC(\sigma) \neq 0_1$, then we say that σ is a *knot pattern* with knot-type $DC(\sigma)$.

Alternatively, the two endpoints of σ_1 (resp. σ_2) can be *reconnected* to each other (outside of $\mathbb{T}$) to form a (possibly separable) link. This is the *numerator closure* of σ. See Figure 3.10(b). Here we are not interested in the overall link-type of the numerator closure; we

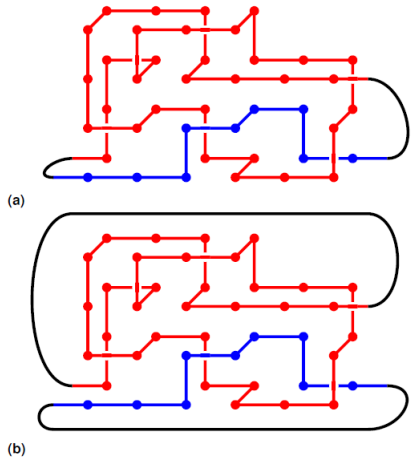

Figure 3.10: (a) An illustration of the denominator closure of a proper cs-pattern σ. The blue strand corresponds to σ_1 and the red to σ_2 and their union is proper cs-pattern σ. The denominator closure is obtained by adding the black arcs and yields a closed curve with knot-type 5_1, i.e. $DC(\sigma) = 5_1$. (b) The numerator closure of the same pattern. The numerator closure gives a link with one component a $3_1 (\neq 5_1)$ knot and the other an unknot ($0_1 \neq 5_1$); hence this is a non-local knot pattern. Here $NC_1(\sigma) = 0_1$ and $NC_2(\sigma) = 3_1$.

instead only care about the knot-types of its two components. Let $NC_1(\sigma)$ (resp. $NC_2(\sigma)$) be the knot-type of the closure of σ_1 (resp. σ_2).

We are now prepared to give our definitions of the local mode and the non-local mode of knot patterns. Let σ be a cs-pattern of a polygon. If σ is a proper pattern with $DC(\sigma) = K \neq 0_1$ but such that $NC_1(\sigma) \neq K\#K'$ and $NC_2(\sigma) \neq K\#K''$ for any K' or K'' (i.e. K is not in the knot decomposition of either $NC_1(\sigma)$ or $NC_2(\sigma)$), then the knot K cannot be discovered by examining only one of the strands of σ. In this case both strands are needed to detect K and hence since the two strands of σ could potentially be far apart along the contour of the entire polygon, we define σ to be a *non-local* mode knot pattern. For example, the denominator closure in Figure 3.10(a) is a 5_1 knot while the components of the numerator closure in Figure 3.10(b) are a trefoil and an unknot; the corresponding proper cs-pattern is therefore a non-local mode knot pattern. For all other cases we classify σ as a *local* mode knot pattern.

3.5.2 Probabilities of Local and Non-local Knot Patterns

As mentioned earlier, this thesis extended the Monte Carlo results from [10], where only the 2×1 and 3×1 tubes were examined. Here, a similar process was repeated for the 4×1, 5×1, 2×2, and 3×2 tubes. The sampled polygons had their knot-type identified by using the slicing method described in Section 2.4.3. Notice that this slicing at each 2-section forms a set of cs-patterns. To determine if the modes of the knotted cs-patterns, each knotted cs-pattern had their denominator and numerator closures formed and knot-type identified. Each knot was then classified as either the local or non-local mode, based on the previous definitions.

We plot the probabilities of local and non-local mode prime knots versus span. That is, for a prime knot K, we plot $P_s(K^{\mathrm{L}})$ and $P_s(K^{\mathrm{NL}})$, and for the Hamiltonian case, we plot $P_s^{\mathrm{H}}(K^{\mathrm{L}})$ and $P_s^{\mathrm{H}}(K^{\mathrm{NL}})$. These plots can be seen in Figure 3.11 for the prime knot-types 3_1, 4_1, 5_1, and 5_2. Observe that the probability of occurrence of a non-local mode knot pattern is significantly greater than that of a local mode knot pattern. This was true for all knot-types observed.

These results show that for tube sizes up to 5×1 and 3×2, the conclusion from [10] that the non-local mode of knotting is more likely than local mode of knotting is still true. It is unknown if this is also true for larger tube sizes, as unfortunately transfer matrices for larger tube sizes have not yet been generated due to computational limitations. It would be interesting to discover if the local mode of knotting becomes more likely than non-local mode at some tube size.

Additionally, one can also look at the average span of the knot patterns (local and non-local modes). This was done in [10] for the 2×1 and 3×1 tubes, but remains to be done for the larger tube sizes. From [10], Figure 3.12 plots the average span of local and non-local 3_1 and 4_1 patterns for all and Hamiltonian polygons. Notice that average spans of non-local mode knot patterns are smaller than the corresponding local knot mode patterns, and also notice that as span gets very large, these average spans appear to remain constant. Thus, knot patterns are relatively small in span and do not grow significantly with polygon size. This is consistent with the results from the previous section that knotting generally occurs

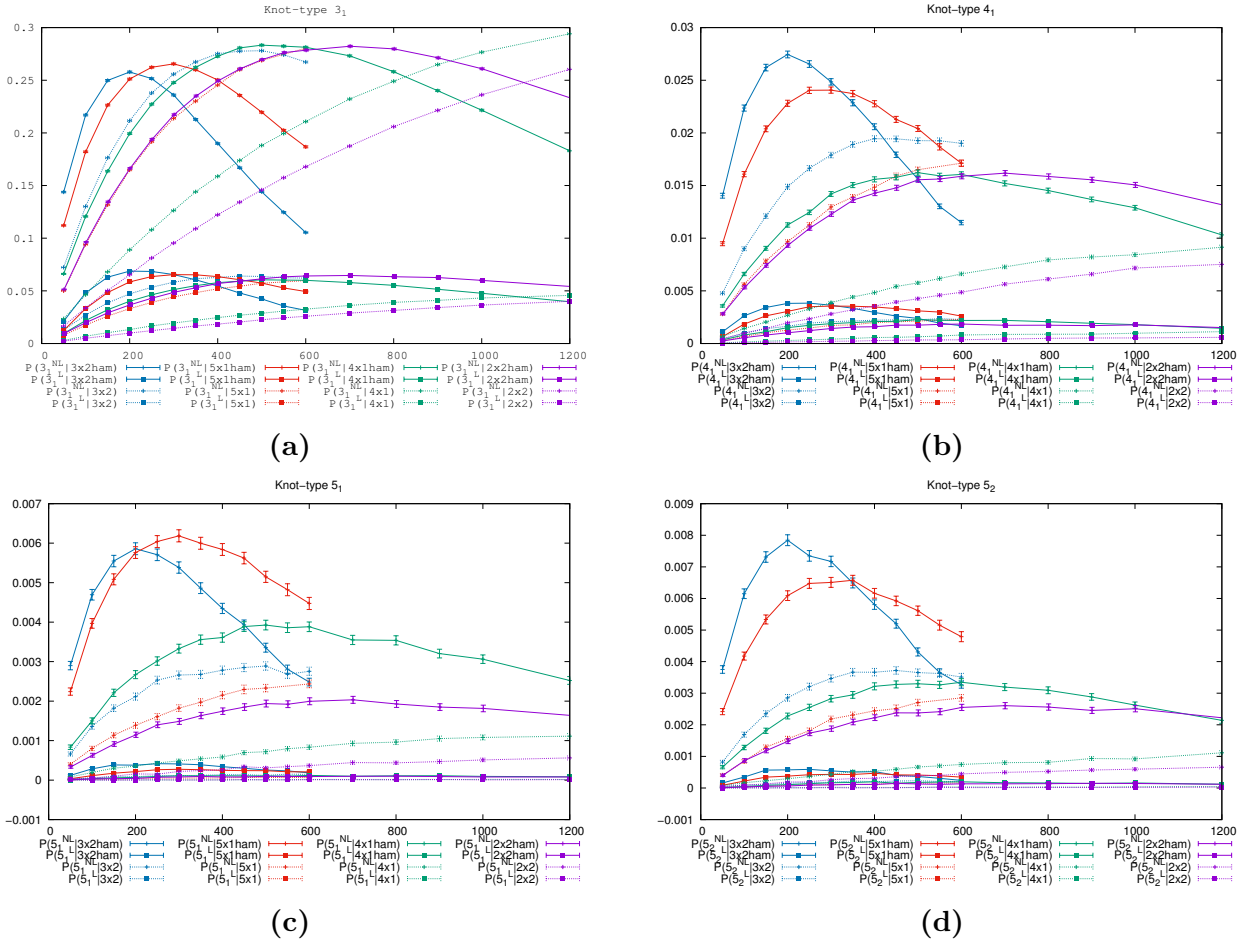

Figure 3.11: Plots of the probabilities of local and non-local knots in different systems. The knot-types (a) 3_1, (b) 4_1, (c) 5_1, and (d) 5_2 are presented here. Matching tube sizes are coloured the same. Solid lines represent the Hamiltonian cases and dashed lines represent the general cases. Local knots are denoted by a solid square, and non-local knots are denoted by a plus symbol. The horizontal axis is span-s. Error bars indicate 95% confidence intervals.

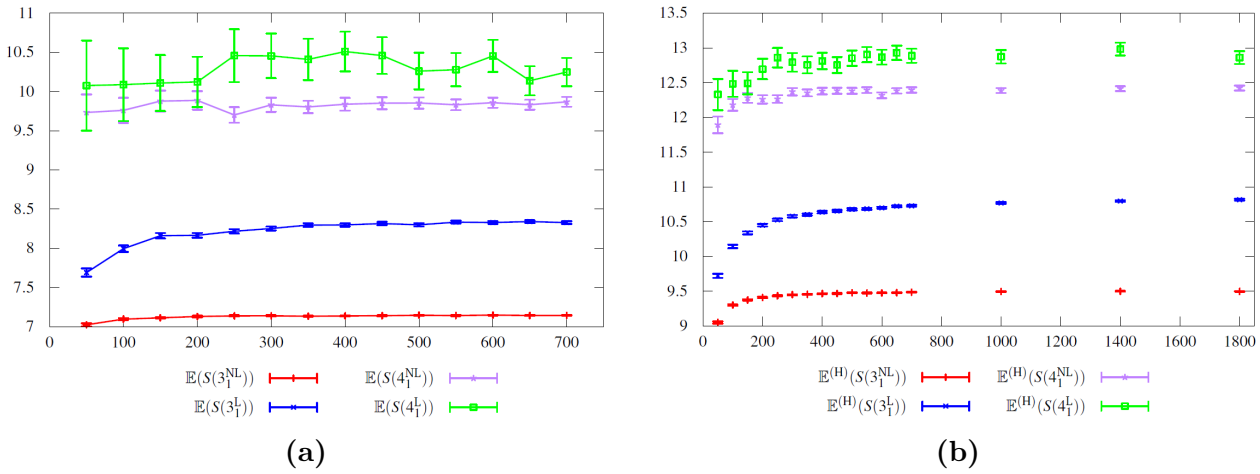

Figure 3.12: Average span of non-local 3_1 (red), local 3_1 (blue), non-local 4_1 (purple), and local 4_1 (green) knot patterns versus overall polygon span, for all polygons (a) and Hamiltonian polygons (b) in the 3×1 tube. Plot is from [10].

as a series of relatively small knot factors.

To summarize, knot patterns are "localized" in the sense that the size of the region in which the crossings are concentrated is relatively small, and evidence indicates that this region does not increase significantly as the size of the polygon increases. Of these localized knot patterns, evidence showed that the non-local mode of knotting is more common than the local mode, at least for the small tube sizes examined here.

Note that there have also been recent simulations of knotted DNA rings translocating through nanopores [59], where two modes of knotting have been observed (which correspond to the definitions of the two modes given here). For that model, the modes were measured as the knot passed through the nanopore. The relative frequencies of the modes depended on the length of the DNA molecule and the initial conditions prior to translocation.

3.6 Summary

In this chapter, results from the generated transfer matrices for SAPs were presented. Transfer matrices were generated for tubes sizes up to 5×1 and 3×2. This was made possible by storing the transfer matrix in terms of 1-patterns instead of 1-blocks with an ordering. From the transfer matrices, connective constants and growth rates were calculated numerically for the fixed-edge, fixed-span, and Hamiltonian models. Knotting distributions were determined

exactly for small spans, and large independent, uniform (with respect to span) samples were obtained by implementing a new Monte Carlo method. These sampled polygons were used to provide evidence toward the conjectured asymptotic growth rate of fixed knot-type SAPs in a tube (Equation 3.6):

$$p_{\mathbb{T},n}(K) \sim C_{\mathbb{T},K}\mu_{\mathbb{T},0_1}^n n^{f_K}, \qquad \text{as} \quad n \to \infty.$$

Evidence was first provided that the unknot (0_1) follows this form, as the plots of $\log \mathbb{P}_{\mathbb{T},s}(0_1)$ showed a strong linear trend (with a negative slope). From the slope of the best fit lines, an estimate for the difference between the growth rates of unknots and all SAPs was calculated. Then, evidence was provided that the form in Equation 3.6 also holds for any prime knot-type K_*, by showing that the ratio $\frac{\mathbb{P}_{\mathbb{T},s}(K_*)}{\mathbb{P}_{\mathbb{T},s}(0_1)}$ has a linear form. To examine if Equation 3.6 holds for any knot-type K, log-log plots of the above ratio for knots with f_K factors were plotted. It was observed that these plots were linear, and furthermore, the slopes of the best-fit lines were close to f_K, further strengthening the evidence supporting Equation 3.6. Lastly, the sampled polygons were also used to examine two modes of knotting, as was done in [10]. It was determined that knots are localized, in the sense that they occur in a localized region, but the knot patterns also occur in two modes of knotting. The two modes of knot patterns, local and non-local knot patterns, were defined, and it was determined from the sampled SAPs that the non-local mode was much more common than the local mode.

In the next chapter, transfer matrices are applied to a system of two mutually-avoiding SAPs in a tube with equal span, called 2SAPs. Novel transfer matrices are created for 2SAPs (and Hamiltonian 2SAPs), and similar techniques to those that were used on SAPs are extended to 2SAPs. Both exact and numerical results are obtained, and some evidence is provided to support a new asymptotic growth conjecture.

4 SYSTEMS OF TWO SPANNING SELF-AVOIDING POLYGONS CONFINED TO A LATTICE TUBE

As mentioned previously, single SAPs on the simple cubic lattice have been used to model and study the self-entanglement of closed curves and ring polymers in many works. In particular, the FWD conjecture [18, 23] that all but exponentially few sufficiently long ring polymers are knotted was first proven using a lattice SAP model [60]. Similar questions regarding the entanglement complexity of multiple closed curves can also be addressed with lattice SAP models, where multiple closed curves can be modelled by mutually avoiding SAPs.

For pairs of mutually avoiding cubic lattice SAPs with total length n (sum of the lengths of each SAP), if the two SAPs are constrained to have a pair of edges (one from each SAP) which are within a fixed distance apart, then the exponential growth rate (with respect to n) of linked SAP pairs is equal to that of the unlinked SAP pairs [40]. That is, unlike the single SAP case with knotting, we cannot say that all but exponentially few SAP pairs are linked, even with this distance constraint. Note that it is still possible that the linking probability goes to one, but it will not do so exponentially fast (with respect to n).

When confined to tubes, the exponential growth rates for linked and unlinked SAP pairs are still equal [63] when again forcing a pair of edges (one from each SAP) to be close. In this thesis, a more severe constraint is put on the pair of SAPs: the pair of SAPs in the tube are forced to have the same span (but not necessarily the same length). This constraint is enough to prove that all but exponentially few sufficiently large spanning pairs of SAPs in an $L \times M$ tube are linked, with $L + M \geq 4$ [6].

In this chapter, the focus is on further studying the entanglement complexity of two

spanning mutually self-avoiding polygons confined to a lattice tube. We call such a pair of spanning polygons in an $L \times M$ tube a *2SAP* (See Figure 4.1). The remainder of this chapter is outlined as follows. In Section 4.1 it is explained how novel 2SAP transfer matrices are created for small tube sizes. In Section 4.2 it is reviewed how the 2SAP concatenation theorem in [6] leads to the existence of the exponential growth rate of 2SAPs. Then, by using the generated transfer matrices, exponential growth rates of 2SAPs are calculated for small tube sizes. To study the entanglement complexity of 2SAPs, the transfer matrices are also used to generate 2SAPs and Knotplot is used to identify their link-types. In Section 4.3, all 2SAPs are generated exactly for small tube sizes and spans – this results in exact linking distributions. Exact "linking numbers" are also calculated via the transfer matrices. To study the asymptotics of the entanglement complexity, we first review the result from [6] that a pattern exists which, when followed by itself, guarantees a link. It is shown that this pattern fits inside the 3×1 tube, which proves the result from [6] that all but exponentially few sufficiently long 2SAPs are linked. In Section 4.4, it is explained why the growth rate of unlinks has yet to be proven to exist, and the growth rate of "untangled" unlinks is introduced and discussed. Next, an asymptotic form for the number of fixed link-type 2SAPs is conjectured, and "unlinking number" and linking number are discussed. To further examine the asymptotics of linking, in Section 4.5, a Monte Carlo sampling technique (similar to that which was done for polygons), is used to obtain independent uniform random samples of 2SAPs. Using these samples, evidence is provided to support the aforementioned asymptotic form, and the possibility that unlinking number affects the entropic exponent is discussed. Ultimately for more conclusive results, larger span 2SAPs are needed, and the challenges and directions for future work are highlighted.

4.1 Creating 2SAP Transfer Matrices

First recall from Section 2.1 that an $L \times M$ tube is the sublattice of $\mathbb{Z}^3$ induced by the vertex set $\{(x, y, z) \in \mathbb{Z}^3 | x \geq 0, 0 \leq y \leq L, 0 \leq z \leq M\}$. A *2SAP* consists of two mutually avoiding SAPs in a $L \times M$ tube $\mathbb{T}$, with each SAP having the same span. We will also consider *Hamiltonian* 2SAPs with span-s, which are 2SAPs that occupy every vertex in a $s \times L \times M$

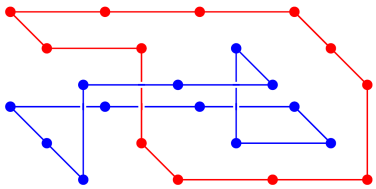

Figure 4.1: An example of a 2SAP in the 2×1 tube with span 3. This 2SAP also happens to be a Hamiltonian 2SAP and has the link-type 2_1^2 (Hopf link).

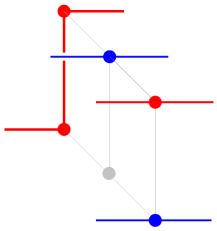

Figure 4.2: An example of a 2SAP proper 1-pattern

subtube of $\mathbb{T}$. See Figure 4.1 for an example of a 2SAP.

The 2SAP transfer matrix was created by utilizing what had already been implemented for the single SAP case. Each row and column of the transfer matrix represents a 2SAP proper 1-pattern (See Figure 4.2). The 2SAP proper 1-patterns were created by first forming a SAP proper 1-pattern, and then adding all other SAP proper-1-patterns which can occur in the remaining unoccupied vertices. Once a valid combination is generated, it is recorded as a 2SAP proper 1-pattern. Transfer matrices were created for 2SAPS and Hamiltonian 2SAPs in the tube sizes $2 \times 1, 3 \times 1, 4 \times 1$, and 2×2. Such transfer matrices have never been created before to our knowledge. Table 4.1 contains the numbers of 2SAP 1-patterns for these tube sizes.

Table 4.1 Number of proper 2SAP and Hamiltonian 2SAP 1-patterns.

Tube Size	2SAP 1-patterns	Ham. 2SAP 1-patterns
1×1	2	2
2×1	1,048	490
3×1	108,410	37,454
4×1	9,419,930	2,598,620
2×2	1,126,578	495,792

Before exploring the results from the 2SAP transfer matrices further, in the next section, the exponential growth rates of 2SAPs are discussed.

4.2 Exponential Growth Rates

The number of edges in a 2SAP is defined to be the sum of the number of edges in both SAPs. Note that althought the two 2SAPs in a 2SAP have the same span, they may not have the same number of edges. Define $\mathcal{Q}_{\mathbb{T}}$ to be the set of 2SAPs in $\mathbb{T}$ where each SAP in the 2SAP occupies at least one vertex in the plane $x = 0$. For the fixed-edge model, let $\mathcal{Q}_{\mathbb{T},n}$ be the subset of $\mathcal{Q}_{\mathbb{T}}$ with n edges, and let $q_{\mathbb{T},n} = |\mathcal{Q}_{\mathbb{T},n}|$. For the fixed-span model, let $\mathcal{Q}_{\mathbb{T}}(s)$ be the subset of 2SAPs from $\mathcal{Q}_{\mathbb{T}}$ with span-s, and let $q_{\mathbb{T}}(s) = |\mathcal{Q}_{\mathbb{T}}(s)|$. Similarly for Hamiltonian 2SAPs, define $\mathcal{Q}^{\mathrm{H}}_{\mathbb{T}}$ to be the set of Hamiltonian 2SAPs in $\mathbb{T}$, let $\mathcal{Q}^{\mathrm{H}}_{\mathbb{T},n}$ be the subset of $\mathcal{Q}^{\mathrm{H}}_{\mathbb{T}}$ with n edges, and let $q^{\mathrm{H}}_{\mathbb{T},n} = |\mathcal{Q}^{\mathrm{H}}_{\mathbb{T},n}|$. Note that a Hamiltonian 2SAP in a $L \times M$ tube has its number of edges determined exactly from its span-s through the relationship $n = (L+1)(M+1)(s+1)$.

For the fixed-edge model, it is proved in [6] that $q_{\mathbb{T},n}$ grows at an exponential rate:

$$q_{\mathbb{T},n} \sim A_{\mathbb{T}} \psi_{\mathbb{T}}^{n}, \qquad \text{as} \quad n \to \infty,$$

where $A_{\mathbb{T}}$ and $\psi_{\mathbb{T}}$ are constants determined by the eigenvectors and eigenvalues of their transfer matrix (details in Section 2.3). Using a very similar argument, it is also known [4] that $q_{\mathbb{T}}(s)$ grows at an exponential rate:

$$q_{\mathbb{T}}(s) \sim B_{\mathbb{T}} \omega_{\mathbb{T}}^{s}, \qquad \text{as} \quad s \to \infty,$$

where $B_{\mathbb{T}}$ and $\omega_{\mathbb{T}}$ are constants, determined by the eigenvectors and eigenvalues of the transfer matrix for $\mathbb{T}$.

These proofs rely on a concatenation theorem for 2SAPs; that is, any two 2SAPs (θ_1 and θ_2) in $\mathbb{T}$ can be concatenated (joined) by: translating θ_2 to the right of θ_1, removing two rightmost edges from θ_1 (one from each polygon) and two leftmost edges from θ_2 (one from each polygon), and adding a finite number of edges within a finite span to join the two 2SAPs in such a way that a new 2SAP in $\mathbb{T}$ is formed. See Figure 4.3 for an illustration of the idea

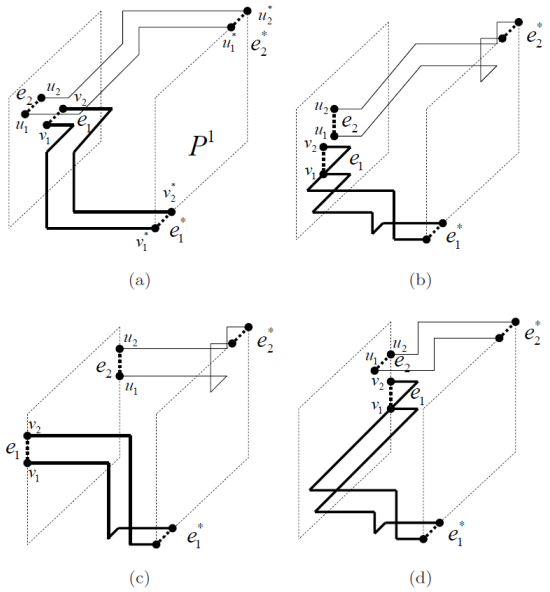

Figure 4.3: This figure from [4] (reproduced with permission of the author) shows how a set of rightmost edges (e_1 and e_2) from a 2SAP can be changed into the edges e_1^* and e_2^*. Using symmetry arguments, this is used to prove a concatenation theorem for 2SAPs (for the full proof, see [4, Lemma 4.3.1]).

behind how a concatenation of 2SAPs can always be formed. See Figure 4.4 for a very simple example of a concatenation of 2SAPs.

Once a concatenation theorem is established, the existence of the exponential growth rates is proved in the following manner. We will work with the fixed-span model, but the fixed-edge model's derivation is very similar. Suppose the 2SAPs θ_1 and θ_2 have spans s and r, respectively. Then using the concatenation theorem, we have

$$q_{\mathbb{T}}(s)q_{\mathbb{T}}(r) \leq q_{\mathbb{T}}(s + r + d_{\mathbb{T}}),$$

where $d_{\mathbb{T}}$ is the finite span needed for the concatenation. Equivalently, we can write the above inequality as

$$\log q_{\mathbb{T}}(s - d_{\mathbb{T}}) + \log q_{\mathbb{T}}(r - d_{\mathbb{T}}) \leq \log q_{\mathbb{T}}(s + r - d_{\mathbb{T}}).$$

Thus, (recall from Section 3.3 in Chapter 3) the sequence $\log q_{\mathbb{T}}(s - d_{\mathbb{T}})$ is *superadditive*, and by Fekete's lemma (see for example [57, Lemma 1.2.1]), we have that

$$\log \omega_{\mathbb{T}} = \lim_{s\to\infty} \frac{1}{s} \log q_{\mathbb{T}}(s) = \sup_{s} \frac{1}{s} \log q_{\mathbb{T}}(s - d_{\mathbb{T}}),$$

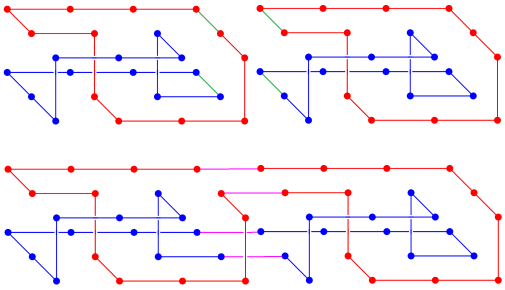

Figure 4.4: Although the concatenation of 2SAPs is more complicated in general, here is an example of concatenating 2SAPs in the 2×1 tube. The green edges are removed and the pink edges concatenate the 2SAPs together to form a new 2SAP. Note that in this example, the two 2SAPs are Hamiltonian 2SAPs and the shown concatenation results in another Hamiltonian 2SAP.

exists.

Notice that once a concatenation theorem is proved, the existence of the exponential growth rate follows. It is expected that Hamiltonian 2SAPs also have a concatenation theorem (i.e. any two Hamiltonian 2SAPs in $\mathbb{T}$ can be concatenated to form another Hamiltonian 2SAP in $\mathbb{T}$, using a finite number of edges and span). See Figure 4.4 for a simple example of a concatenation of two Hamiltonian 2SAPs. This simple concatenation can be performed when there are two pairs of matching edges across from one another (one edge from each polygon, in each 2SAP). The Hamiltonian concatenation theorem's proof is expected to be a combination of the 2SAP concatenation proof in [6] and techniques used to prove a concatenation theorem for Hamiltonian polygons (done in my Master's thesis [20, Theorem 4.1]), but full details are yet to be worked out. One must ensure that the concatenation process fills all vertices so the resulting 2SAP is also Hamiltonian. Thus, it is expected that

$$q^{\mathrm{H}}_{\mathbb{T},n} \sim A^{\mathrm{H}}_{\mathbb{T}} \left(\psi^{\mathrm{H}}_{\mathbb{T}}\right)^n, \qquad \text{as} \quad n \to \infty. \tag{4.1}$$

As mentioned earlier, part of this thesis work was creating transfer matrices for 2SAPs and Hamiltonian 2SAPs in small tube sizes of $\mathbb{T}$ ($2 \times 1, 3 \times 1, 4 \times 1$, and 2×2). From these transfer matrices, the exponential growth rates for the fixed-edge model, fixed-span model, and Hamiltonian model ($\psi_{\mathbb{T}}$, $\omega_{\mathbb{T}}$ and $\psi^{\mathrm{H}}_{\mathbb{T}}$, respectively) are directly calculated (results in Table 4.2). Note that since the Hamiltonian 2SAP transfer matrices are irreducible and aperiodic, it follows from the Perron-Frobenius theorem that the Hamiltonian growth rate (of Equation

Table 4.2 The growth rate constants for 2SAPs from the fixed-edge model ($\psi_{\mathbb{T}}$), Hamiltonian model ($\psi_{\mathbb{T}}^{\mathrm{H}}$), and fixed-span model ($\omega_{\mathbb{T}}$). The growth rate $\omega_{\mathbb{T}}^{\mathrm{H}}$ is the Hamiltonian growth rate if counting by span instead of edges, with the direct relationship $\omega_{\mathbb{T}}^{\mathrm{H}} = \left(\psi_{\mathbb{T}}^{\mathrm{H}}\right)^{(L+1)(M+1)}$. Error is expected to be confined to the last digit.

Tube	$\psi_{\mathbb{T}}$	$\psi_{\mathbb{T}}^{\mathrm{H}}$	$\omega_{\mathbb{T}}$	$\omega_{\mathbb{T}}^{\mathrm{H}}$
2×1	1.5292741300	1.3299693974	9.4559609907	5.5341481260
3×1	1.9076033253	1.4906484172	65.0125083457	24.3782358112
4×1	2.1774964452	1.5814502215	380.8242546757	97.8480976778
2×2	2.0774601803	1.5567085577	180.5117028784	53.6865331419

4.1) exists for these tube sizes where the transfer matrices are actually generated.

In the next section, the generated transfer matrices are also used to exactly generate all 2SAPs for small spans.

4.3 Exact Results

Exact counts for 2SAPs and Hamiltonian 2SAPs by link-type were obtained for small tube sizes and spans via the transfer matrices. This was done using a method similar to the method used for calculating exact knot-type counts for SAPs (details in Section 2.3.4). Essentially, a complete set of all 2SAPs in these tube sizes of small span are generated, limited by computational resources (memory and time). These 2SAPs then have their link-type identified using the software Knotplot [49]. Since determining the link-type of a 2SAP requires the whole 2SAP to be generated, and since the number of 2SAPs grows exponentially (with span or edges), exact link-type results have been limited to the cases in Tables 4.3 (all) and 4.4 (Hamiltonian). Note that there were unresolved memory issues in the 4×1 case when generating a complete set, but random samples were obtained during Monte Carlo sampling of the 4×1 case (presented in Section 4.5).

If we are interested in just the linking probability (or the probability of unlinks), and not the full link distribution, it is possible to use "linking number" to achieve a lower bound on linking probability (and an upper bound on the probability of unlinks). The *linking number* (Lk) of a 2SAP is the sum of all the signed crossings between the two SAPs, of any

Table 4.3 2SAP generation results. Note that these results prove a new result regarding the minimal number of edges (and minimal span) required for the 2_1^2 and 4_1^2 link-types in these tube sizes.

Tube	Span	Total	2_1^2	4_1^2
1×1	all	2	0	0
2×1	1	72	0	0
2×1	2	623	0	0
2×1	3	5,609	8	0
2×1	4	51,046	198	0
2×1	5	467,109	3,458	0
2×1	6	4,288,906	50,943	0
2×1	7	39,482,621	680,200	16
2×1	8	364,275,071	8,511,359	796
2×1	9	3,367,542,877	101,738,596	27,958
3×1	1	1,334	0	0
3×1	2	77,030	72	0
3×1	3	4,622,536	33,464	2
3×1	4	281,352,953	5,021,040	2,878
2×2	1	4,636	0	0
2×2	2	727,556	0	0
2×2	3	120,511,504	2,992,984	0

Table 4.4 Hamiltonian 2SAP generation results.

Tube	Span	Total	2_1^2	4_1^2	5_1^2	6_1^2	6_3^2	$0_1^2\#3_1$	$2_1^2\#3_1$
1×1	all	2	0	0	0	0	0	0	0
2×1	1	21	0	0	0	0	0	0	0
2×1	2	91	0	0	0	0	0	0	0
2×1	3	537	8	0	0	0	0	0	0
2×1	4	2,623	46	0	0	0	0	0	0
2×1	5	14,809	542	0	0	0	0	0	0
2×1	6	75,966	3,258	0	0	0	0	0	0
2×1	7	419,979	26,083	16	0	0	0	0	0
2×1	8	2,213,901	160,470	156	0	0	0	0	0
2×1	9	12,137,972	1,104,425	3,164	0	0	0	0	0
2×1	10	65,030,655	6,779,625	29,406	0	0	0	0	0
2×1	11	355,727,584	43,386,541	314,410	128	32	0	0	0
3×1	1	139	0	0	0	0	0	0	0
3×1	2	2,764	18	0	0	0	0	0	0
3×1	3	65,121	988	2	0	0	0	0	0
3×1	4	1,451,096	47,490	228	0	0	0	0	0
3×1	5	33,755,040	1,740,206	17,639	0	0	0	0	0
3×1	6	780,310,655	58,322,308	926,876	3,032	158	18	0	0
2×2	1	364	0	0	0	0	0	0	0
2×2	2	0	0	0	0	0	0	0	0
2×2	3	772,756	39,288	0	0	0	0	0	0
2×2	4	0	0	0	0	0	0	0	0
2×2	5	1,422,685,876	294,135,968	1,428,848	112	10	0	27,416	4,960

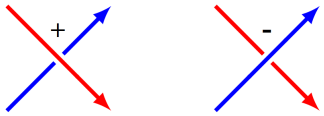

Figure 4.5: The right-hand-rule for crossings between two SAPs.

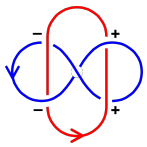

Figure 4.6: An example of a non-trivial link with linking number zero, the *Whitehead link* (5_1^2)

.

projection, divided by 2. The signed crossings are based on a right-hand rule (see Figure 4.5), and changing the orientation of one of the SAPs changes the sign of the linking number; therefore, typically when discussing the linking number of a link, the absolute value of the linking number is used ($|Lk|$). Note that a link with a non-zero linking number must be linked, but a link with linking number zero may be linked or unlinked (for example see Figure 4.6).

Since linking number is an additive property that can be stored in the transfer matrix, linking numbers can be calculated without needing to generate 2SAPs – instead powers of the transfer matrix can be taken to calculate linking numbers. Exact linking number results for 2SAPs and Hamiltonian 2SAPs are given in Appendix B in Tables B.1 and B.2. These results were obtained in collaboration with an undergraduate summer student, Nicole Zolkavich, who programmed the linking numbers for the 2×1 and 3×1 tube sizes.

While these exact results regarding linking probabilities are limited to small spans, it has been proved in [6] that all but exponentially few sufficiently long 2SAPs are linked. This is done by showing that a pattern (see Figure 4.7), called γ, which guarantees a 2SAP is linked (if it follows itself) occurs and follows itself in all but exponentially few sufficiently long 2SAPs. With Zolkavich, we showed that this pattern fits in the 3×1 tube. See Figure 4.7 for a diagram of γ, as well as its version in the 3×1 tube.

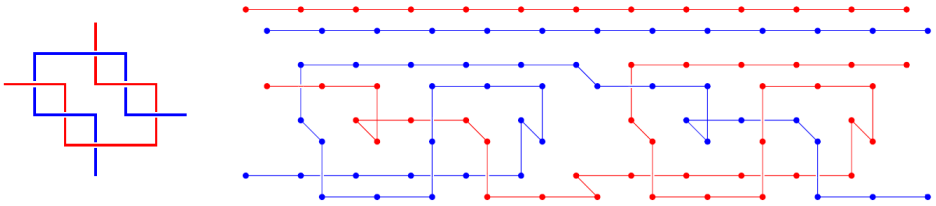

Figure 4.7: On the left, the occurrence of this pattern (γ), followed by itself, guarantees a 2SAP is linked [6]. On the right, a lattice version of γ is shown in the 3×1 tube.

Using this pattern γ, it is known that unlinks are exponentially rare among all 2SAPs, but otherwise little is known about unlinks or other 2SAPs with fixed link-type. For example, unlike for the unknot, no concatenation theorem has been proved for unlinks. The next section discusses these challenges and puts forward some hypotheses about the asymptotics for the number of 2SAPs with fixed link-type.

4.4 Hypotheses About the Exponential Growth Rates of Some Different Types of 2SAPs

In this section, we hypothesize about the growth rates of some different types of 2SAPs. Recall from Section 3.3 that for polygons in $\mathbb{T}$, a concatenation theorem exists for unknots (i.e. two unknots in $\mathbb{T}$ can be concatenated (joined) to form another unknot in $\mathbb{T}$), and thus we know the exponential growth rate for unknots exists. However, for 2SAPs, a concatenation theorem for unlinks (0_1^2) analagous to that for unknots does not work, since when concatenating two unlinks by concatenating the polygons pairwise, the result may not be an unlink. See Figure 4.8 for an example of this. Let $q_{\mathbb{T}}(s; L)$ denote the number of span-s 2SAPs in $\mathbb{T}$ with link-type L. We can still however define

$$\hat{\omega}_{\mathbb{T}}(0_1^2) = \limsup_{s\to\infty} \frac{1}{s} \log q_{\mathbb{T}}(s; 0_1^2),$$

and it was proved in [6] that this limit superior is strictly less than the growth rate of all 2SAPs ($\hat{\omega}_{\mathbb{T}}(0_1^2) < \omega_{\mathbb{T}}$), a type of FWD conjecture for links.

The situation when "concatenated" unlinks do not form another unlink arises when the

concatenated unlinks are "tangled". "Untangled" unlink 2SAPs are defined as follows: First define a *left-end pair* (*right-end pair*) to be a pair of edges, one from each component, that are on the leftmost (rightmost) plane of the 2SAP. Then if there exists a left-end (right-end) pair such that when they are removed, the resulting two self-avoiding walks, with fixed end points, can be reduced (via BFACF moves that leave the fixed endpoints untouched) to that left-end (right-end) pair, then we say the 2SAP is left (right) untangled. See Figure 4.8 a) for an unlink 2SAP that is not right untangled. Note that the left half of Figure 4.8 b) shows the two self-avoiding walks obtained by removing a right-end pair; this forms a *2-string tangle* (see for example [19]), which in this case is inseparable. If the 2SAP had been right untangled, the corresponding 2-string tangle would be separable. Finally, an unlink 2SAP is defined here to be *untangled* if it is both left and right untangled, otherwise it is called *tangled*.

Let $q_{\mathbb{T}}^{(\mathrm{un})}(s;0_1^2)$ be the number of untangled unlink 2SAPs in $\mathbb{T}$ with span-s. We expect that the same concatenation theorem from [6] applies (i.e. two concatenated untangled unlinks will form another untangled unlink) to give

$$q_{\mathbb{T}}^{(\mathrm{un})}(s;0_1^2)q_{\mathbb{T}}^{(\mathrm{un})}(r;0_1^2) \leq q_{\mathbb{T},}^{(\mathrm{un})}(s+r+d_{\mathbb{T}};0_1^2),$$

so the sequence $\log(q_{\mathbb{T}}^{(\mathrm{un})}(s-d_{\mathbb{T}};0_1^2))$ is superadditive, and the exponential growth rate for untangled unlink 2SAPs exists:

$$\log \omega_{\mathbb{T}}^{(\mathrm{un})}(0_1^2) = \lim_{s\to\infty} \frac{1}{s} \log q_{\mathbb{T}}^{(\mathrm{un})}(s;0_1^2) = \sup_s \frac{1}{s} \log q_{\mathbb{T}}^{(\mathrm{un})}(s-d_{\mathbb{T}};0_1^2).$$

A natural next question then is: How does the exponential growth rate of untangled unlinks compare to that of the unlink? Certainly $q_{\mathbb{T}}^{(\mathrm{un})}(s;0_1^2) \leq q_{\mathbb{T}}(s;0_1^2)$. We haven't yet developed an algorithm to identify untangled unlinks to compare the exponential growth rates numerically; however, we note that, as illustrated in Figure 4.8, tangled unlink patterns can typically only occur once in an unlink 2SAP, while untangled unlink patterns can occur multiple times. This suggests the possibility that untangled unlink patterns will be dominant and that untangled unlinks will have the same exponential growth rate as all unlinks. This hypothesis will be tested as part of future work.

Notice that if we concatenate an untangled unlink 2SAP with span-s to a span-r (fixed) 2SAP with any fixed link-type L, the resulting 2SAP will be of link-type L with span $s+r+d_{\mathbb{T}}$.

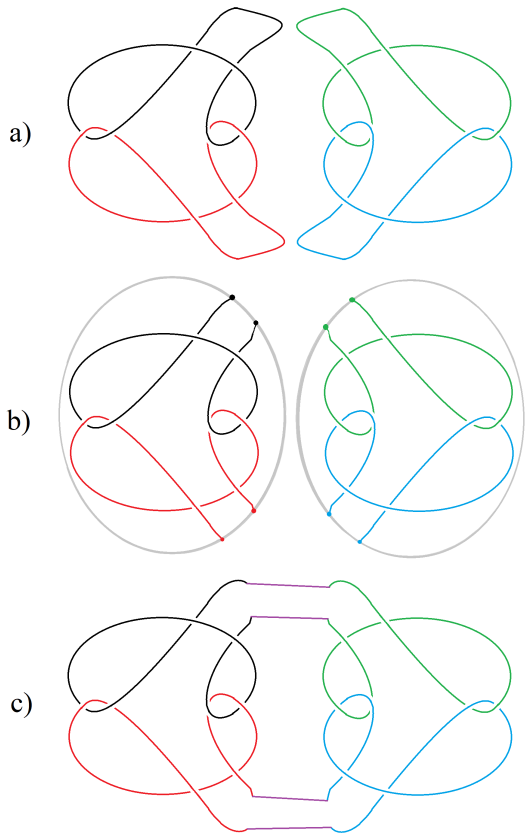

Figure 4.8: An example of two tangled unlink 2SAPs. Concatenating these two unlink 2SAPs does not form another unlink . In a) the first 2SAP is not right untangled, and the second 2SAP is not left untangled. In b) the right-end pair of the first 2SAP is removed, and the left-end pair of the second 2SAP is removed. For each 2SAP, the result is two self-avoiding walks which form a 2-string tangle. In this case, both 2-string tangles are inseparable. Thus, the result of the concatenation in c) is not an unlink. Note Shimokawa [53] used the program "Knot" [30] to determine that the non-trivial link in c) has a Conway Polynomial of $-2z^7 - 6z^5 - 5z^3 - 2z$.

Thus we have $q_{\mathbb{T}}^{(\mathrm{un})}(s;0_1^2) \leq q_{\mathbb{T}}(s+r+d_{\mathbb{T}};L)$. Taking the log, dividing by s, and taking the $\lim_{s\to\infty}$, we have the result that the exponential growth rate (assuming the limit exists) of any link-type L is at least as big as the exponential growth rate of untangled unlinks:

$$\omega_{\mathbb{T}}^{(\mathrm{un})}(0_1^2) \leq \omega_{\mathbb{T}}(L). \tag{4.2}$$

Recall from Section 3.1.1 that for SAPs with fixed knot-type K, it is believed that $p_{\mathbb{T}}(s;K) \sim D_{\mathbb{T},K}\nu_{\mathbb{T},0_1}^s s^{f_K}$ and that this has been proved [5] for SAPs in the 2×1 tube for knots which have unknotting number one, or are connect sums of such, and we have provided strong numerical evidence that it holds up to tube sizes 5×1 and 3×1 in Section 3.4. What then is the appropriate scaling form for 2SAPs with fixed link-type L? First note that since 2SAPs consist of only two polygons, a link-type L 2SAP has a factorization of the form $L = L'\#K_1\#\ldots\#K_{f_{\mathrm{knot}}(L)}$, where L' is either the unlink or is a prime 2-component non-split link and $f_{\mathrm{knot}}(L)$ is the number of prime knot factors in L. It seems reasonable to suppose that, as for knots, the exponential growth rate for fixed link-type 2SAPs will not depend on the link-type, i.e. it will be the same as that for unlinks. Similarly, it seems reasonable that the knot factors can be relatively localized within the 2SAP and hence the entropic critical exponent would still go up by one for each knot factor. So this leaves open the question of how does the factor L' contribute to the exponent, if at all. That is, we conjecture a general form:

$$q_{\mathbb{T}}(s;L) \sim B_{\mathbb{T},L}\omega_{\mathbb{T}}(L)^s s^{f_{\mathrm{knot}}(L)+g(L')}, \qquad \text{as} \quad s\to\infty, \tag{4.3}$$

where if $L' = 0_1^2$, $g(L') = 0$, but otherwise what should the term $g(L')$ be? To get some initial ideas about $g(L')$, we start with what can be proved for the 2×1 tube.

In [5], it is shown that if $\mathbb{T} = 2\times 1$ and L' is a prime two component non-split link with "unlinking number" 1 (the *unlinking number* $u(L)$ of L is the minimal number of crossing changes necessary to convert the diagram of L into a diagram of the unlink), then a twist operation can always be performed to turn a 2SAP with link-type L' into an unlink 2SAP. Specifically for $\mathbb{T} = 2\times 1$ and $u(L') = 1$, a location can be found such that a "twist pattern" (with span $t_{\mathbb{T}}$) can be inserted at that location to turn the 2SAP into an unlink, giving that

$$q_{\mathbb{T}}(s;L) \leq (Cs)q_{\mathbb{T}}(s+t_{\mathbb{T}};0_1^2). \tag{4.4}$$

Note that the term Cs is needed because the twist operation is not one-to-one (i.e. there may be more than one 2SAP with link-type L' which, after performing the twist operation, results in the same unlink). Taking the log, dividing by s, and taking the $\lim_{s\to\infty}$, gives the upper bound (assuming the limits exist)

$$\omega_{2\times 1}(L) \leq \omega_{2\times 1}(0_1^2). \tag{4.5}$$

If the exponential growth rates are equal, then the upper bound in Equation 4.4 says that $g(L') \leq 1$ for $u(L') = 1$. However, unlike for knots, here we don't have, as of yet, a corresponding lower bound to establish that $g(L') = 1$. Even if we suppose that $g(L') = 1$ is true, we don't know whether the increase by one from the unlink is due to the fact that L' is one factor in the prime decomposition of the link or whether it is because $u(L') = 1$, i.e. what will happen for a prime link with $u(L') = 2$? Many open questions remain. In Section 4.5 we numerically explore the possibility that the upper bound in Equation 4.5 holds for all tube sizes, and the exponential growth rate of a link-type L 2SAP is equal to that of the unlink. Moreover, we also explore the possibility that the entropic critical exponent goes up by one with either unlinking number or by factors.

Motivated by examining the growth rate of unlinks further, we also discuss the linking number of 2SAPs. Let $q_{\mathbb{T}}(s; Lk = 0)$ be the number of span-s 2SAPs in $\mathbb{T}$ with linking number zero. Although the concatenation process of [6] doesn't preserve orientation, it is expected that the concatenation can be slightly modified to preserve orientation, without adding anything to the linking number (a detailed proof has yet to be worked out). Since concatenating two 2SAPs with linking number zero (regardless of orientation) results in another 2SAP with linking number zero, we have

$$q_{\mathbb{T}}(s; Lk = 0)q_{\mathbb{T}}(r; Lk = 0) \leq q_{\mathbb{T}}(s + r + d_{\mathbb{T}}; Lk = 0).$$

Thus the exponential growth rate of 2SAPs with linking number zero ($\omega_{\mathbb{T}}(Lk = 0)$) exists.

We conjecture that in the set of 2SAPs with linking number zero, unlinks are exponentially rare (at least for $L + M \geq 4$). This reasoning is based on the pattern γ (Figure 4.7), the pattern which if followed by itself, guarantees a link. If we create a new pattern which is $\gamma + \gamma + \gamma' + \gamma'$, where γ' is γ with all of its crossings reversed in sign, then this new pattern,

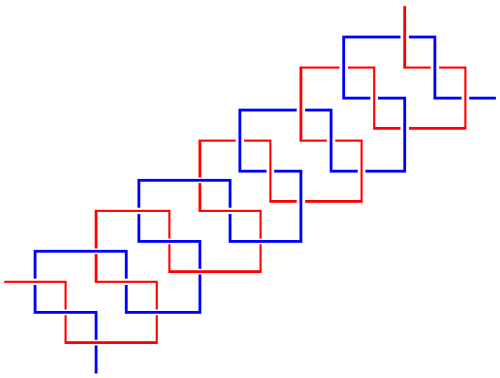

Figure 4.9: The occurrence of this pattern ($\gamma + \gamma + \gamma' + \gamma'$) guarantees a 2SAP is linked [6]. Also, it has a linking number of zero.

if it occurs, guarantees a link and contributes zero to the linking number (See Figure 4.9). Since this pattern can occur over and over in a linking number zero 2SAP, but can never occur in an unlink, we expect that unlinks are exponentially rare among linking number zero 2SAPs. In Section 4.5.1, we provide numerical evidence that this is true.

To summarize, it has not yet been proven that the exponential growth rate of unlinks exists because the techniques that are used to prove the existence of the exponential growth rate of unknots cannot be analogously applied to unlinks, due to the existence of tangled unlinks. It is shown that the exponential growth rate of untangled unlinks exists, and it is hypothesized that it is equal to that of unlinks. It is then shown that the exponential growth rate of any link-type L is at least a big as that of untangled unlinks, and it is hypothesized that all link-types have the same exponential growth rate. Based on the scaling form of fixed-knot type polygons, an asymptotic growth form for the number of span-s 2SAPs with link-type L is conjectured (in Equation 4.3), and it is hypothesized that the entropic exponent goes up by one for each knot factor ($f_{\text{knot}}(L)$), as well as potentially by the unlinking number $u(L')$. It is also shown that the exponential growth rate of linking number zero 2SAPs exists, and among these linking number zero 2SAPs, it is expected that unlinks are exponentially rare.

The next section contains evidence, obtained via Monte Carlo sampling, which supports the conjectures made in this section.

4.5 Monte Carlo Results

The Monte Carlo method used here for 2SAPs is very similar to the method used for SAPs, described in Section 2.3.4. This Monte Carlo method generates sets of independent and identically distributed random 2SAPs from a uniform distribution with respect to span. A summary table of the 2SAP Monte Carlo results can be seen in Appendix C in Table C.3 (all) and Table C.4 (Hamiltonian). 2SAPs with larger spans than those presented in the tables were obtained, but link identification by the software Knotplot [49] limited identification to 2SAPs around span 100. This is because projections of these larger span 2SAPs contain many crossings (even after BFACF moves), and calculating the HOMFLY polynomial is very difficult. Additionally, Knotplot only identifies link-types up to those with a minimal crossing number of 9. The linking numbers of the sampled 2SAPs were also calculated by using a program which I created during my Ph.D. research. These linking number results (by absolute value of Lk) are located in Appendix B in Tables B.3 (all) and B.4 (Hamiltonian).

The sampled 2SAPs are used to support conjectures made in Section 4.4 and to provide evidence for Equation 4.3: the conjecture that the number of 2SAPs in $\mathbb{T}$ with span-s and link-type $L = L'\#K_1\#\ldots\#K_{f_{\text{knot}}(L)}$ has the asymptotic form:

$$q_{\mathbb{T}}(s;L) \sim B_{\mathbb{T},L}\omega_{\mathbb{T}}(L)^s s^{f_{\text{knot}}(L)+g(L')}, \qquad \text{as} \quad s \to \infty,$$

where $B_{\mathbb{T},L}$ and $\omega_{\mathbb{T},L}$ are constants which may depend on L, and $g(L')$ is some function of L' which may be unlinking number. Unfortunately since Knotplot limited the link identification to spans around 100, evidence so far regarding Equation 4.3 is limited to simple link-types.

4.5.1 Evidence that the asymptotic form holds for the unlink, and estimates for the exponential growth rates of unlinks and linking number zero 2SAPs

Let $\mathbb{P}_{\mathbb{T},s}(L) = \frac{q_{\mathbb{T}}(s;L)}{q_{\mathbb{T}}(s)}$ be the probability that a 2SAP in $\mathbb{T}$ with span-s has link-type L. Recall from earlier that it is known that $q_{\mathbb{T}}(s) \sim B_{\mathbb{T}}\omega_{\mathbb{T}}^s$. First we provide evidence that the

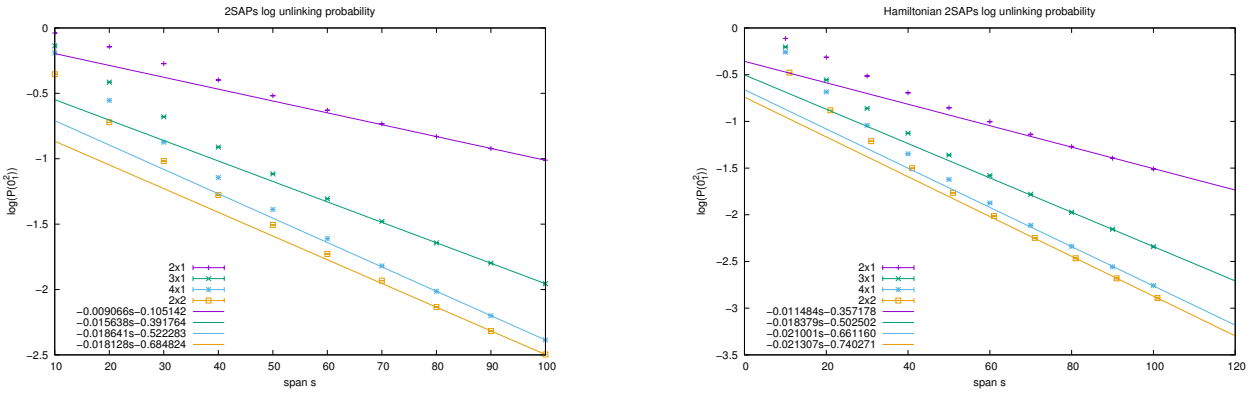

(a) **(b)**

Figure 4.10: Plots of (a) $\log \mathbb{P}_{\mathbb{T},s}(0_1^2)$ and (b) $\log \mathbb{P}^{\mathrm{H}}_{\mathbb{T},s}(0_1^2)$ against s (span) for tube sizes $2\times 1, 3\times 1, 4\times 1$, and 2×2, together with linear best fits (for $s \geq 80$). Error bars indicate 95% confidence intervals.

conjectured form in Equation 4.3 holds for the unlink (0_1^2):

$$q_{\mathbb{T}}(s; 0_1^2) \sim B_{\mathbb{T},0_1^2}\omega_{\mathbb{T}}(0_1^2)^s, \qquad \text{as} \quad s \to \infty.$$

If this is correct, then we have

$$\log \mathbb{P}_{\mathbb{T},s}(0_1^2) \sim B + s \log\left(\frac{\omega_{\mathbb{T}}(0_1^2)}{\omega_{\mathbb{T}}}\right), \qquad \text{as} \quad s \to \infty,$$

with constant $B = \log \frac{B_{\mathbb{T},0_1^2}}{B_{\mathbb{T}}}$.

Equivalently for Hamiltonian 2SAPs, let $\mathbb{P}^{\mathrm{H}}_{\mathbb{T},s}(L) = \frac{q^{\mathrm{H}}_{\mathbb{T}}(s;L)}{q^{\mathrm{H}}_{\mathbb{T}}(s)}$, and we conjecture $q^{\mathrm{H}}_{\mathbb{T}}(s; 0_1^2) \sim B^{\mathrm{H}}_{\mathbb{T},0_1^2}\omega^{\mathrm{H}}_{\mathbb{T}}(0_1^2)^s$, as $s \to \infty$. Then for Hamiltonian 2SAPs, we have the conjectured form

$$\log \mathbb{P}^{\mathrm{H}}_{\mathbb{T},s}(0_1^2) \sim B^{\mathrm{H}} + s \log\left(\frac{\omega^{\mathrm{H}}_{\mathbb{T}}(0_1^2)}{\omega^{\mathrm{H}}_{\mathbb{T}}}\right), \qquad \text{as} \quad s \to \infty,$$

with constant $B^{\mathrm{H}} = \log \frac{B^{\mathrm{H}}_{\mathbb{T},0_1^2}}{B^{\mathrm{H}}_{\mathbb{T}}}$.

The generated 2SAPs from the Monte Carlo sampling are used to plot $\log \mathbb{P}_{\mathbb{T},s}(0_1^2)$ and $\log \mathbb{P}^{\mathrm{H}}_{\mathbb{T},s}(0_1^2)$ against span (s) for tube sizes $2\times 1, 3\times 1, 4\times 1$, and 2×2 in Figure 4.10. We also plot the best fit line (for span ≥ 80) for each of these cases.

From the plots, we can see that for larger spans (≥ 80) the linear fit is good for all of the cases (reduced chi-squared statistic $< 10^{-4}$), which indicates the form in Equation 4.3 is correct for the unlink. Therefore, we conclude that $\log \mathbb{P}_{\mathbb{T},s}(0_1^2) \sim a_{0_1^2}s + b_{0_1^2}$ and

Table 4.5 Linear best-fit estimates for the slopes $a_{0_1^2}$ and $a^{\mathrm{H}}_{0_1^2}$ (columns 2 and 3), which indicate the difference between the growth rates of unlink 2SAPs and 2SAPs. Also, linear best-fit estimates for the slopes $a_{Lk=0}$ and $a^{\mathrm{H}}_{Lk=0}$ (columns 4 and 5), which indicate the difference between the growth rates of linking number zero 2SAPs and 2SAPs.)

Tube	$a_{0_1^2}$ (error)	$a^{\mathrm{H}}_{0_1^2}$ (error)	$a_{Lk=0}$ (error)	$a^{\mathrm{H}}_{Lk=0}$ (error)
2×1	-0.0090662 (6.574e-5)	-0.0114836 (0.0001867)	-0.00715013 (0.0001824)	-0.00655631 (0.0003714)
3×1	-0.0156382 (7.001e-5)	-0.0183786 (0.0001723)	-0.00662074 (0.0003437)	-0.00645542 (2.529e-5)
4×1	-0.0186413 (4.519e-6)	-0.0210013 (0.0004629)	-0.00625299 (0.0001898)	-0.00588743 (0.0005829)
2×2	-0.0181280 (0.0001216)	-0.021307 (0.0001032)	-0.00566182 (0.0001723)	-0.00562454 (0.0001071)

Table 4.6 Growth rate estimates of unlink 2SAPs ($\omega_{\mathbb{T}}(0_1^2)$ and $\omega^{\mathrm{H}}_{\mathbb{T}}(0_1^2)$), and growth rate estimates for linking number zero 2SAPs ($\omega_{\mathbb{T}}(Lk=0)$ and $\omega^{\mathrm{H}}_{\mathbb{T}}(Lk=0)$).

Tube	$\omega_{\mathbb{T}}(0_1^2)$	$\omega^{\mathrm{H}}_{\mathbb{T}}(0_1^2)$	$\omega_{\mathbb{T}}(Lk=0)$	$\omega^{\mathrm{H}}_{\mathbb{T}}(Lk=0)$
2×1	9.366291611	5.464377167	9.38859078	5.497983219
3×1	63.96855199	23.92013228	64.58349918	24.22137092
4×1	373.5382447	95.70605360	378.450394	97.27371633
2×2	177.0783007	52.52462412	179.4925659	53.3854187

$\log \mathbb{P}^{\mathrm{H}}_{\mathbb{T},s}(0_1^2) \sim a^{\mathrm{H}}_{0_1^2} s + b^{\mathrm{H}}_{0_1^2}$, where the estimates for $a_{0_1^2}$ and $a^{\mathrm{H}}_{0_1^2}$ are given in Table 4.5. The errors denote the asymptotic standard error reported by gnuplot [76] using a least squares fit. Using the slopes of these best fit lines (Table 4.5) along with the calculated growth rates of 2SAPs (Table 4.2), we calculate estimates for the growth rates of the unlink (in Table 4.6).

To get an estimate of the growth rate of linking number zero 2SAPs, let $\mathbb{P}_{\mathbb{T},s}(Lk=0) = \frac{q_{\mathbb{T}}(s;Lk=0)}{q_{\mathbb{T}}(s)}$ be the probability that a 2SAP in $\mathbb{T}$ with span-s has linking number zero. Recall from earlier that it is hypothesized that $q_{\mathbb{T}}(s;Lk=0) \sim B_{\mathbb{T},Lk=0}\left[\omega_{\mathbb{T}}(Lk=0)\right]^s s^{\alpha}$, so

$$\log \mathbb{P}_{\mathbb{T},s}(Lk=0) \sim B' + s\log\left(\frac{\omega_{\mathbb{T}}(Lk=0)}{\omega_{\mathbb{T}}}\right) + \alpha \log s, \qquad \text{as} \quad s\to\infty,$$

with constant $B' = \log \frac{B_{\mathbb{T},Lk=0}}{B_{\mathbb{T}}}$. A similar derivation can be made for Hamiltonian 2SAPs with linking number zero to obtain the form

$$\log \mathbb{P}^{\mathrm{H}}_{\mathbb{T},s}(Lk=0) \sim B'^{\mathrm{H}} + s\log\left(\frac{\omega^{\mathrm{H}}_{\mathbb{T}}(Lk=0)}{\omega^{\mathrm{H}}_{\mathbb{T}}}\right) + \alpha^{\mathrm{H}} \log s, \qquad \text{as} \quad s\to\infty,$$

with constant $B'^{\mathrm{H}} = \log \frac{B^{\mathrm{H}}_{\mathbb{T},Lk=0}}{B^{\mathrm{H}}_{\mathbb{T}}}$. Figure 4.11 contains plots of $\log \mathbb{P}_{\mathbb{T},s}(Lk=0)$ and $\log \mathbb{P}^{\mathrm{H}}_{\mathbb{T},s}(Lk=0)$ against span (s) for tube sizes $2\times 1, 3\times 1, 4\times 1$, and 2×2. The plots

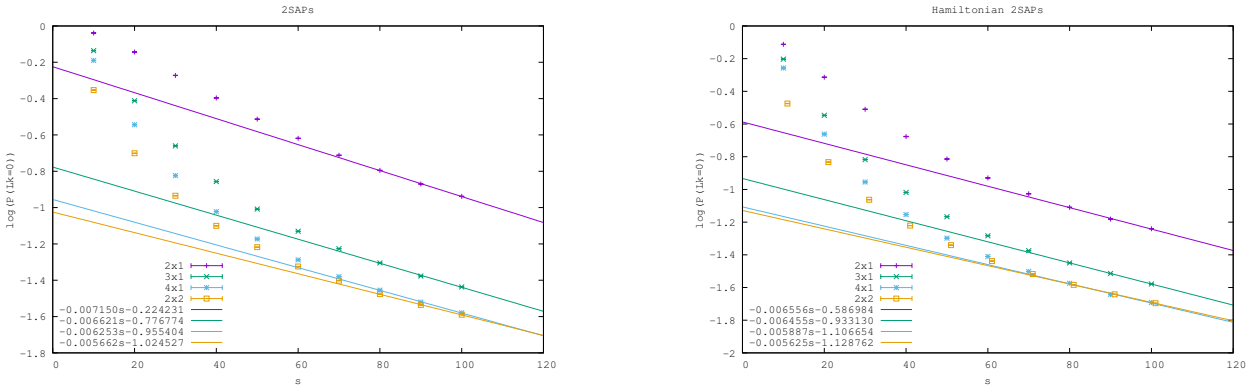

(a) **(b)**

Figure 4.11: Plots of (a) $\log \mathbb{P}_{\mathbb{T},s}(Lk = 0)$ and (b) $\log \mathbb{P}^{\mathrm{H}}_{\mathbb{T},s}(Lk = 0)$ against s (span) for tube sizes $2 \times 1, 3 \times 1, 4 \times 1$, and 2×2, together with linear best fits (for $s \geq 80$). Error bars indicate 95% confidence intervals.

appear to be approaching linear, indicating that $\alpha = \alpha^{\mathrm{H}} = 0$. We also plot the best fit line (for span ≥ 80) for each of these cases. Using the slopes of the best fit lines (Table 4.5) along with the calculated growth rates of 2SAPs (Table 4.2), we calculate estimates for the growth rates of linking number zero 2SAPs (in Table 4.6).

Notice that the exponential growth rate estimates for the number of unlink 2SAPs is smaller than that for the linking number zero 2SAPs, in each system studied (especially for $\mathbb{T} > 2 \times 1$). This supports our earlier conjecture that unlinks are exponentially rare among linking number zero 2SAPs. In Figure 4.12 we also plot the log ratio

$$\log \frac{\mathcal{P}_{\mathbb{T},s}(0_1^2)}{\mathcal{P}_{\mathbb{T},s}(Lk = 0)},$$

and the negative slope of the best fit lines (for $s \geq 80$) further indicate that unlink 2SAPs are exponentially rare among linking number zero 2SAPs.

4.5.2 Evidence that the asymptotic form holds for the simplest link-types

In this subsection we provide evidence that Equation 4.3 holds for some simple link-types. As mentioned earlier, due to Knotplot limiting the maximum span of link-identification, this evidence is limited to simple link-types. Consider $\log(\mathbb{P}_{\mathbb{T},s}(L)/\mathbb{P}_{\mathbb{T},s}(0_1^2))$ for some link-type L.

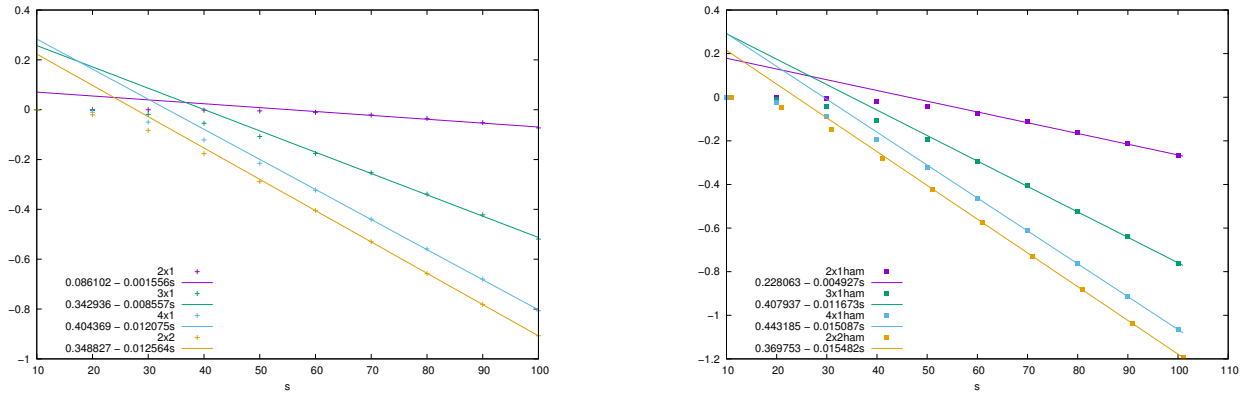

(a) **(b)**

Figure 4.12: Plots of (a) $\log(\mathbb{P}_{\mathbb{T},s}(0_1^2)/\mathbb{P}_{\mathbb{T},s}(Lk=0))$ and (b) $\log(\mathbb{P}^{\mathrm{H}}_{\mathbb{T},s}(0_1^2)/\mathbb{P}^{\mathrm{H}}_{\mathbb{T},s}(Lk=0))$ against s (span) for tube sizes $2\times 1, 3\times 1, 4\times 1$, and 2×2, together with linear best fits (for $s \geq 80$).

If Equation 4.3 holds, then

$$\log \frac{\mathbb{P}_{\mathbb{T},s}(L)}{\mathbb{P}_{\mathbb{T},s}(0_1^2)} \sim C + s\log\frac{\omega_{\mathbb{T}}(L)}{\omega_{\mathbb{T}}(0_1^2)} + (f_{\mathrm{knot}}(L)+g(L'))\log s, \qquad \text{as} \quad s\to\infty, \tag{4.6}$$

and for Hamiltonian 2SAPs,

$$\log \frac{\mathbb{P}^{\mathrm{H}}_{\mathbb{T},s}(L)}{\mathbb{P}^{\mathrm{H}}_{\mathbb{T},s}(0_1^2)} \sim C^{\mathrm{H}} + s\log\frac{\omega^{\mathrm{H}}_{\mathbb{T}}(L)}{\omega_{\mathbb{T}}(0_1^2)^{\mathrm{H}}} + (f_{\mathrm{knot}}(L)+g(L'))\log s, \qquad \text{as} \quad s\to\infty, \tag{4.7}$$

where $C = B_{\mathbb{T},L}/B_{\mathbb{T},0_1^2}$ and $C^{\mathrm{H}} = B^{\mathrm{H}}_{\mathbb{T},L}/B^{\mathrm{H}}_{\mathbb{T},0_1^2}$.

This log ratio is plotted in Figure 4.13 for the prime non-split links (a) $L=2_1^2$ and (b) $L=4_1^2$, along with non-linear fits to the above form (for $s\geq 60$). Note that $u(2_1^2)=1$, and $u(4_1^2)=2$, so if $g(L')=u(L')$, then the coefficient of $\log(s)$ is expected to be 1 in (a) and 2 in (b). Note that the log ratio $\log(\mathbb{P}_{\mathbb{T},s}(4_1^2)/\mathbb{P}_{\mathbb{T},s}(2_1^2))$ was also plotted (not shown) with the same non-linear fit and the coefficient of $\log(s)$ was close to 1. Also, as mentioned in the previous section, it is expected that $\omega_{\mathbb{T},L}=\omega_{\mathbb{T}}(0_1^2)$ (and $\omega^{\mathrm{H}}_{\mathbb{T},L}=\omega^{\mathrm{H}}_{\mathbb{T}}(0_1^2)$), so the coefficient of s is expected to be zero for any L.

From Figure 4.13, one can see that the coefficients of s are small, but they are statistically different than zero in most cases. It is expected that as larger span 2SAPs are sampled, these coefficient will go to zero. In (a) most of the coefficients of $\log(s)$ are close to one, indicating that the entropic exponent increases by one from the unlink to the 2_1^2 link. In (b) most of the coefficients of $\log(s)$ are close to two, indicating the possibility that the entropic exponent

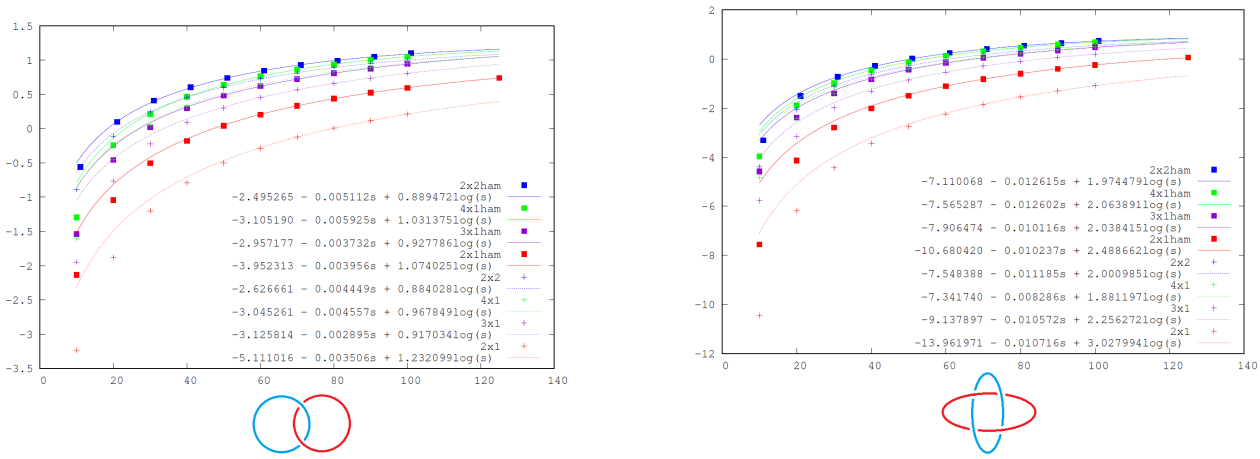

(a) **(b)**

Figure 4.13: Plots of the ratios (a) $\log \mathbb{P}_{\mathbb{T},s}(2_1^2)/\mathbb{P}_{\mathbb{T},s}(0_1^2)$ and (b) $\log \mathbb{P}_{\mathbb{T},s}(4_1^2)/\mathbb{P}_{\mathbb{T},s}(0_1^2)$, along with non-linear fits ($s \geq 40$).

increases by two from the unlink to the 4_1^2 link. Note that for the 2×1 cases in (b), the coefficients of $\log(s)$ are not so close to two–it is believed that this is due to a lack of larger span sampling which is, especially needed in the 2×1 tube since links are less likely.

Note that this evidence suggests the exponent increases by one (two) when comparing the unlink to the 2_1^2 (4_1^2). Although $u(2_1^2) = 1$ and $u(4_1^2) = 2$, there may be other link characteristics affecting the exponent. Also, one cannot rule out the possibility that with larger span samples, the 4_1^2 exponent estimates could get closer to 1, for example.

Next we examine the entropic exponent when a prime knot factor is added. Due to the small tube sizes, not many samples contained a prime knot factor; in fact, in the 2×1 tube, both components of a 2SAP must be unknotted [5]. The only systems where a sufficient amount of prime knot factors were observed (over 0.01% of samples) were the 4×1 and 2×2 Hamiltonian cases. For these cases, in Figure 4.14, the log ratio

$$\log \frac{\mathbb{P}^{\mathrm{H}}_{\mathbb{T},s}(0_1^2 \# 3_1)}{\mathbb{P}_{\mathbb{T},s}(0_1^2)}$$

is plotted in (a) and the log ratio

$$\log \frac{\mathbb{P}^{\mathrm{H}}_{\mathbb{T},s}(2_1^2 \# 3_1)}{\mathbb{P}_{\mathbb{T},s}(2_1^2)}$$

is plotted in (b). From the non-linear fits, the coefficients of $\log(s)$ are close to 1 as expected, since both of these link-types are adding a single knot factor.

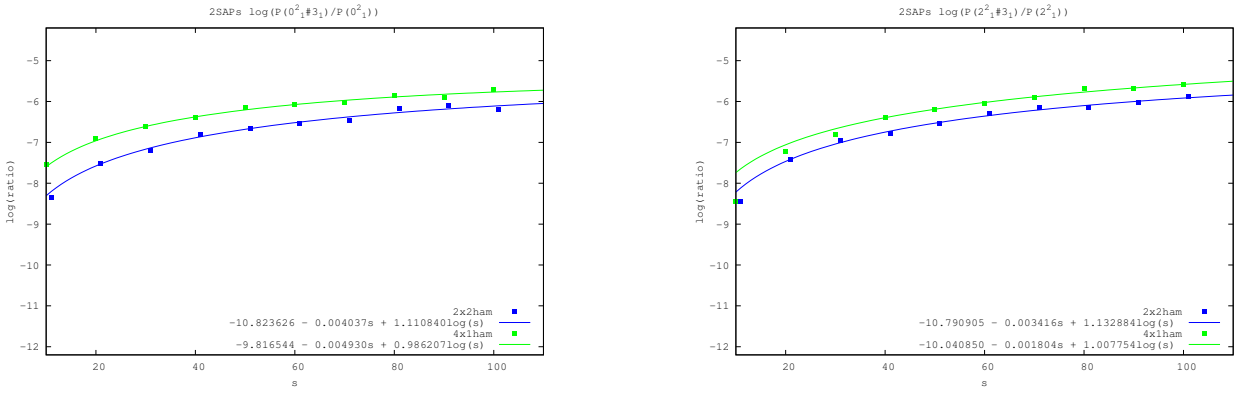

(a) **(b)**

Figure 4.14: Plots of the log ratios (a) $\log(\mathbb{P}_{\mathbb{T},s}(0_1^2\#3_1)/\mathbb{P}_{\mathbb{T},s}(0_1^2))$ and (b) $\log(\mathbb{P}_{\mathbb{T},s}(2_1^2\#3_1)/\mathbb{P}_{\mathbb{T},s}(2_1^2))$, along with non-linear fits ($s \geq 60$).

The Whitehead link (5_1^2), pictured in Figure 4.15 (a), has an unlinking number of one; however, our data for estimating the exponent for the Whitehead link (see Figure 4.15(b)) indicates that the exponent goes up by more than one. The theory in the previous section says that for the 2×1 tube, the Whitehead link cannot grow faster exponentially than the unlink, and if it grows at the same exponential rate as the unlink, the entropic critical exponent cannot go up by more than 1. Figure 4.15(b) indicates that the the Whitehead link is not growing slower than the unlink (ratio is increasing), so likely it does grow at the same exponential rate. The Whitehead's exponent estimates (coefficients of $\log(s)$) are all ≥ 2.77. This indicates that at least for the 2×1 tube, larger span data must make the exponent estimate go to one (or lower). Also for other tube sizes and other link-types, we cannot rule out that their exponent estimates go down to one eventually (or even zero).

Note that if we look back at the polygon Monte Carlo exponent analysis from Section 3.4, the log-log plots in Figures 3.6 and 3.7 did not start to look linear until around span 400. The same is true in [12] where the knotting in the 2×1 and 3×1 tube sizes are studied for very large span. So for 2SAPs, although there is some preliminary evidence that the critical exponent may increase by unlinking number (for 2_1^2 and 4_1^2), larger span samples of 2SAPs are needed to further study the hypotheses about the asymptotics of the number of fixed link-type 2SAPs. It is possible that the unlinking number only plays a role at shorter spans and the exponent only increases by one for each (link or knot) factor in L (with $g(0_1^2) = 0, g(L') = 1$). Thus the results here for shorter spans should be taken as

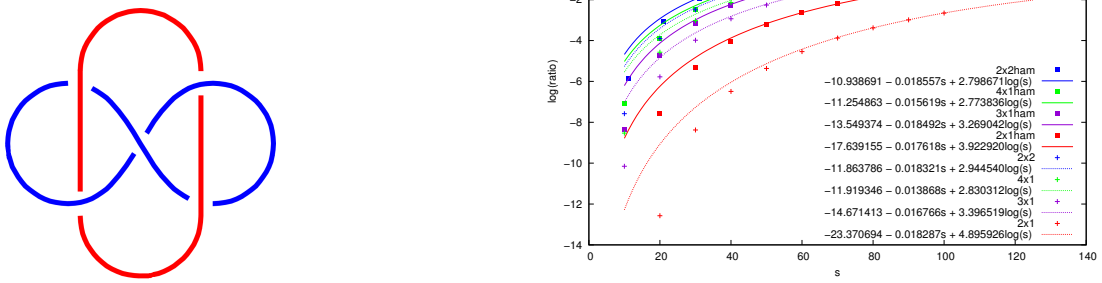

(a) **(b)**

Figure 4.15: In (a) a diagram of the Whitehead link (5_1^2). In (b) a plot of the log ratio: $\log \mathbb{P}_{\mathbb{T},s}(5_1^2)/\mathbb{P}_{\mathbb{T},s}(0_1^2)$ along with non-linear fits ($s \geq 60$).

preliminary and there are open questions remaining.

4.5.3 Grouping by unlinking number and link factor

In this subsection, we further examine the possibility that the entropic exponent relies on unlinking number. Recall that Knotplot limits the link identification to link-types with a minimal crossing number (MCN) of ≤ 9. Additionally, the unlinking numbers are only known for link-types with MCN ≤ 9 [31] (as far as we know). Let L^* be a 2SAP with no knot factors, MCN ≤ 9, and unlinking number $u(L^*)$. Let $\mathbb{P}_{\mathbb{T},s}(u(L^*) = i)$ be the probability that a 2SAP with no knot factors and MCN ≤ 9 has unlinking number i. Using Equation 4.6, if we assume $g(L') = u(L')$ and $\omega_{\mathbb{T}}(L) = \omega_{\mathbb{T}}(0_1^2)$, then since the number of link-types with MCN ≤ 9 is a constant, we have the conjectured asymptotic form:

$$\log \frac{\mathbb{P}_{\mathbb{T},s}(u(L^*) = i)}{\mathbb{P}_{\mathbb{T},s}(0_1^2)} \sim C + u(L^*) \log s, \qquad \text{as} \quad s \to \infty.$$

The log-log plots of this ratio for $i = 1, 2, 3, 4$ are in Figures 4.16 (all) and 4.17 (Hamiltonian). Notice that the slopes of the best-fit lines for $u(L^*) = i$ are somewhat close to i for $i = 1, 2$. However, for $i = 2, 3, 4$, the slopes are less than i (except for the 2×1 tube), and notice the slopes are decreasing with span. This indicates that the exponent may be less than the unlinking number for unlinking numbers 2, 3, 4, and one can hypothesize that if larger spans were sampled, the slopes could be going to one.

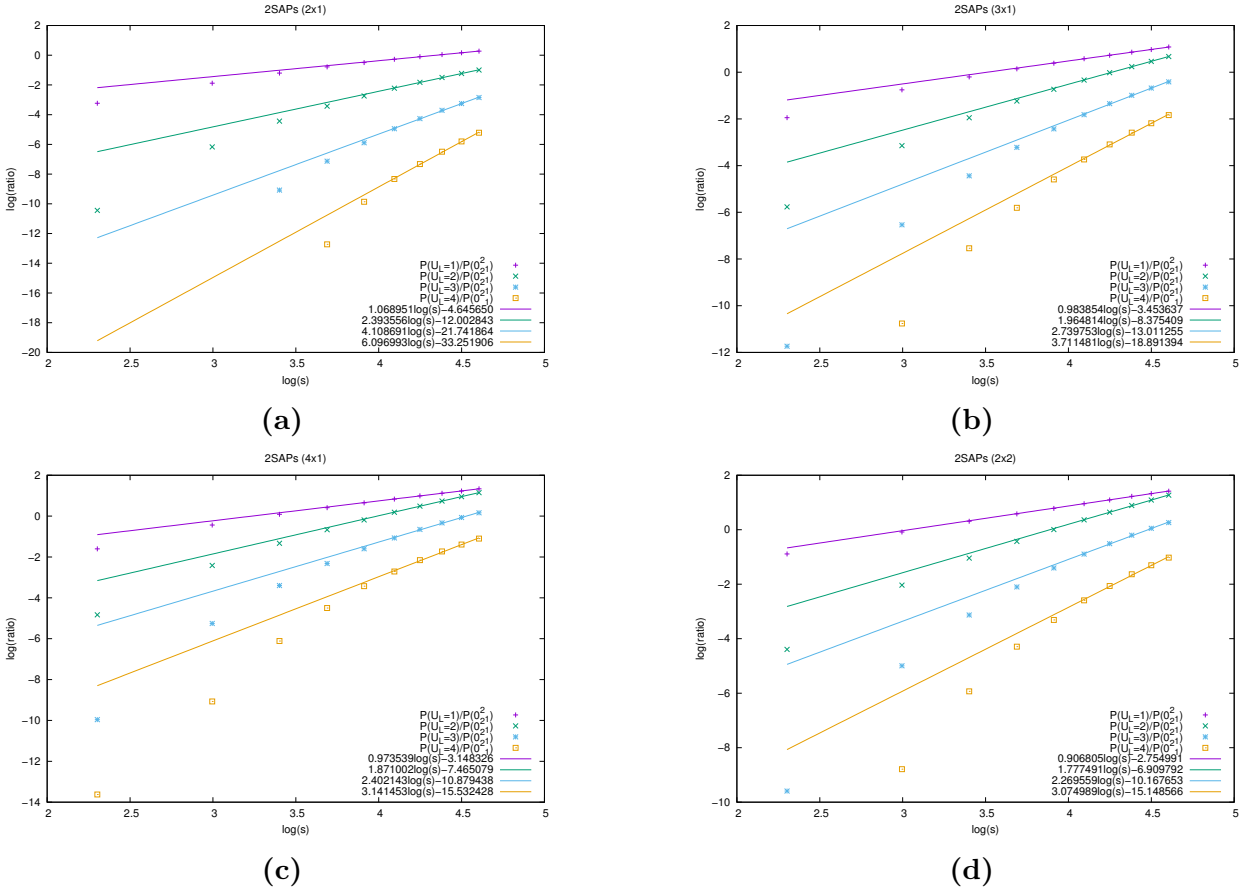

Figure 4.16: Log-log plots of $\log(\mathbb{P}_{\mathbb{T},s}(u(L^*))/\mathbb{P}_{\mathbb{T},s}(0_1^2))$ against $\log(s)$ for $u(L^*) = 1, 2, 3, 4$, together with straight line fits for spans $s \geq 60$, for tube sizes (a) 2×1, (b) 3×1, (c) 4×1, and (d) 2×2.

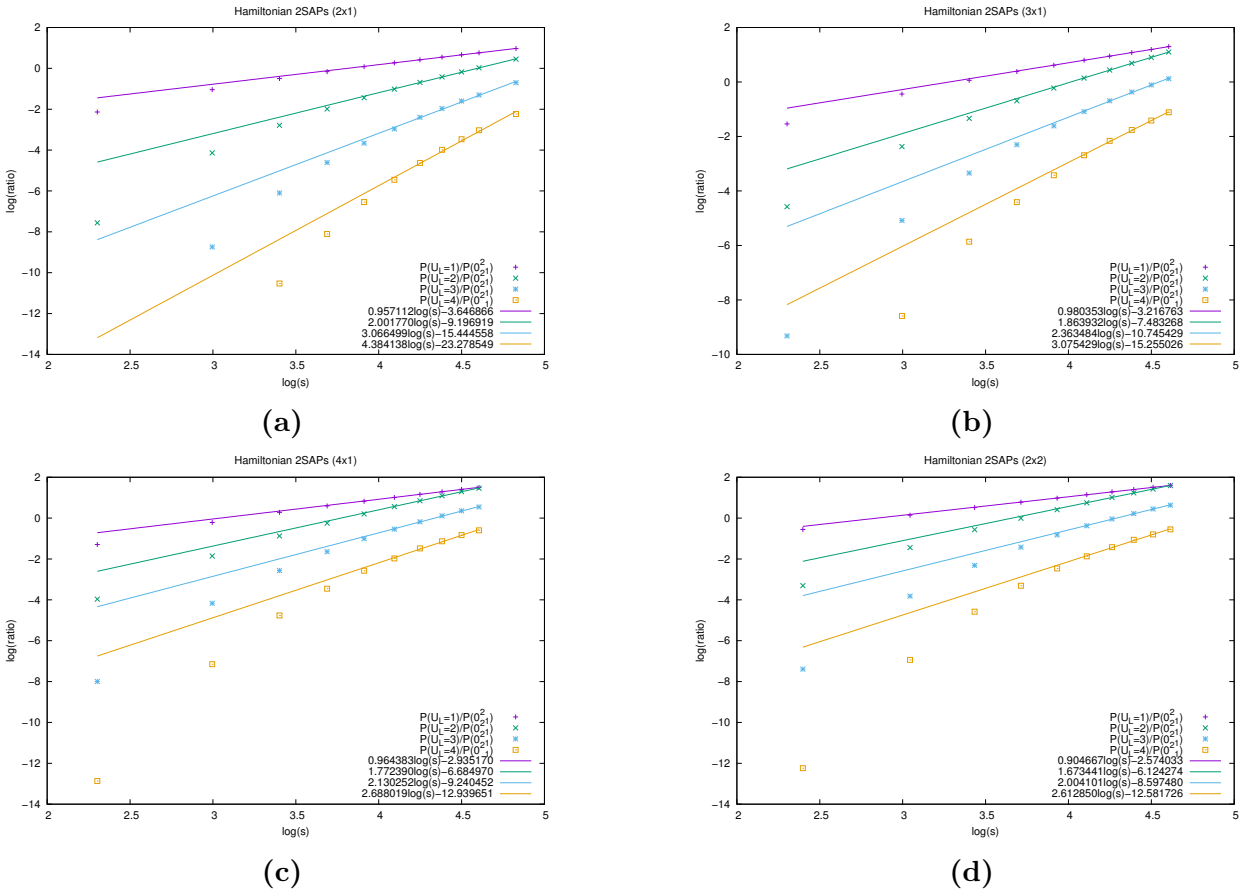

Figure 4.17: Log-log plots of $\log(\mathbb{P}^{\mathrm{H}}_{\mathbb{T},s}(L^*,0,0))/\mathbb{P}^{\mathrm{H}}_{\mathbb{T},s}(0^2_1))$ against $\log(s)$ for $u(L^*) = 1,2,3,4$, together with straight line fits for spans $s \geq 60$, for tube sizes (a) 2×1, (b) 3×1, (c) 4×1, and (d) 2×2.

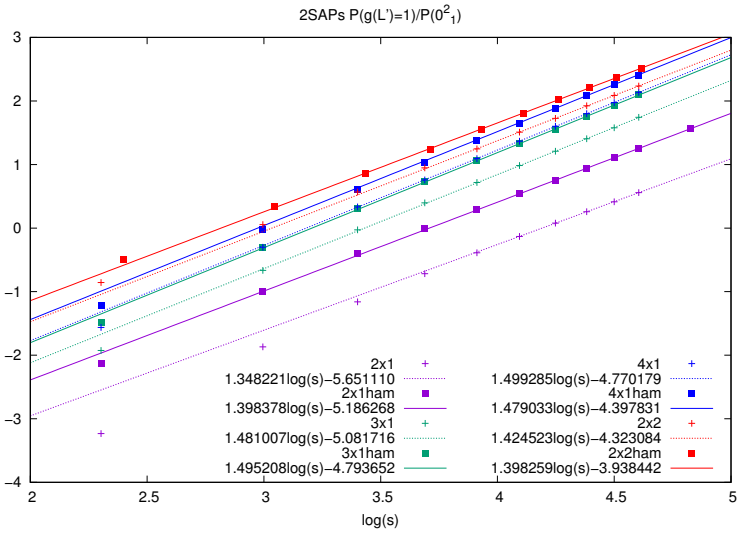

Figure 4.18: Log-log plot of $P(f_{\text{link}}(L^*) = 1)/P(0_1^2)$

To explore the possibility that $g(L') = f_{\text{link}}(L)$, the number of link-factors in L (i.e. $g(0_1^2) = 0, g(L') = 1$), we group all the prime non-split links with MCN ≤ 9. Figure 4.18 contains a plot of the log ratio $\log\left[P(f_{\text{link}}(L^*) = 1)/P(0_1^2)\right]$ against $\log(s)$. Notice that all of the best-fit lines ($s \geq 60$) have slopes > 1, but larger spans are needed to see if the slopes indeed go down to one.

Overall, the Monte Carlo results presented in this section provide some preliminary evidence that the asymptotic form for the number of span-s 2SAPs with link-type L is

$$q_{\mathbb{T}}(s; L) \sim B_{\mathbb{T},L}\omega_{\mathbb{T}}(L)^s s^{f_{\text{knot}}(L)+g(L')}, \qquad \text{as} \quad s \to \infty,$$

and we hypothesize that $g(L')$ is either the unlinking number of L' ($g(L') = u(L')$) or the number of link factors in L ($g(L') = f_{\text{link}}(L)$).

We provide some small span evidence that for $L = 2_1^2$ and $L = 4_1^2$, our data indicates that the exponent increases according to unlinking number. However, this may be due to only having small span data and is not indicative of the asymptotics of $q_{\mathbb{T}}(s; L)$. We also provide limited evidence (4×1 and 2×2 Hamiltonian cases) that the exponent also increases according to number the of knot factors. We then show that if we group by unlinking number, the exponent estimates seem to be too small, and the estimates are decreasing further as span increases, indicating that perhaps it is not the unlinking number in the exponent. If we group

all of the links with link factor one together, the estimates for the exponent seem too large (> 1).

To summarize, some preliminary small span data leads us to inconclusive results about the entropic exponent, but the work done is still useful for further examining the entropic exponent. The issue for obtaining larger span results does not lie within generating larger span 2SAPs; the current issue is instead identifying the link-type of larger span 2SAPs. As mentioned back in Section 2.4.3, the "slicing method", which is used to first simplify then identify long span polygons, cannot be applied directly to 2SAPs due to each 2SAP having at least four edges in each section. However, there is still potential to "simplify" a 2SAP without changing its link-type (via BFACF moves) to not only reduce its span, but also open up the possibility of performing slicing on the individual polygons in a 2SAP. This is left as future work.

4.6 Summary

In this chapter, novel 2SAP transfer matrices were created for small tube sizes. Using these generated transfer matrices, exponential growth rates of 2SAPs are calculated. To study the entanglement complexity of 2SAPs, the transfer matrices were also used to actually generate 2SAPs. Exact sets of 2SAPs were generated for small spans, and linking numbers were calculated directly from the transfer matrices. For larger spans, the result from [6] was reviewed, which showed that a pattern exists which, when followed by itself, guarantees a link. It was then shown that this pattern fits inside the 3×1 tube, which proved the result from [6] that all but exponentially few sufficiently long 2SAPs are linked (for $L + M \geq 4$). Next, it was explained why the existence of the growth rate for unlinks has not yet been proven, and the growth rate for untangled unlinks was discussed. Then, an asymptotic form for the number of fixed link-type 2SAPs was conjectured, with the possibility that the entropic exponent depends on the unlinking number. To further examine the asymptotics of linking, Monte Carlo sampling was used to obtain independent uniform random samples of 2SAPs. Using these samples, some preliminary evidence was provided for the aforementioned asymptotic form, and it was discussed why larger span samples are needed to draw further

conclusions.

5 CONCLUSIONS AND FUTURE WORK

5.1 Review

In this thesis, transfer matrices are used as a tool to examine and characterize the entanglement complexity of self-avoiding polygons in tubes. For small tube sizes, novel transfer matrices are created for both SAPs and 2SAPs, in small tube sizes. Exponential growth rates for the number of SAPs and 2SAPs are calculated directly from these transfer matrices. To study the entanglement complexity of SAPs and 2SAPs, full SAPs and 2SAPs are generated via transfer matrices. Exact enumeration results are obtained for small spans, and a novel Monte Carlo sampling technique is developed to obtain independent, uniform, random samples with large span. Using the generated SAPs, an estimate of the growth rate of unknots is calculated, and evidence is provided which supports a conjectured asymptotic form for the number of span-s polygons in $\mathbb{T}$ with knot-type K:

$$p_{\mathbb{T}}(s;K) \sim D_{\mathbb{T},K}\nu_{\mathbb{T},0_1}^{s}s^{f_K}, \qquad \text{as} \quad s \to \infty.$$

This indicates that the knotted parts of long polygons occur in a relatively localized manner, and the entropic exponent depends only on the number of factors in a knot-type K. This also is believed to be true for SAPs without a tube constraint, based on numerical evidence [68]. Evidence from this thesis also indicates that the span of the knotted parts of the polygons don't grow significantly with polygon size, which is different than the unconfined case, where evidence indicates that the size of knot factor patterns increases with polygon size [39]. Additionally, two modes of knot patterns are observed (as seen during pore translocation of knotted DNA rings [59]), and evidence indicates that the non-local mode dominates for small tube sizes.

Using the generated 2SAPs, evidence is provided which supports a conjectured asymptotic

form for the number of span-s 2SAPs in $\mathbb{T}$ with link-type L:

$$q_{\mathbb{T}}(s;L) \sim B_{\mathbb{T},L}\omega_{\mathbb{T},L}^{s}s^{f_{\text{knot}}(L)+g(L')}, \qquad \text{as} \quad s \to \infty,$$

where L' is the prime link factor of L. Some preliminary evidence is provided that indicates $g(L')$ may either be the unlinking number of L' ($g(L') = u(L')$) or the number of link factors in L ($g(L') = f_{\text{link}}(L)$). However, it is determined that larger span samples of 2SAPs are needed for further conclusions.

5.2 Conclusions

It is determined that in small tube sizes, the knotting or linking probability of polymers increases as the size of the polymer increases. Also, tightly formed polymers (modelled by Hamiltonian SAPs/2SAPs) have higher knotting and linking probabilities, which is consistent with unconfined collapsed SAPs having a higher knotting probability than non-collapsed SAPs [69]. When the cross-sectional area of a tube remains constant, evidence obtained indicates that knotting and linking is more likely in a more symmetrical tube as opposed to a more narrow, flat tube.

Evidence obtained from generated polygons also indicates that long polymers confined in tubular environments occur in a relatively localized manner; that is, knotting occurs as a sequence of knotted factors. This is supported by evidence that the entropic critical exponent increases by one for each knot factor in the knot-type. Similar evidence is obtained for the knotted part of 2SAPs. For the SAP study, preliminary evidence indicates that the average spans of the knot factor patterns are not growing with polygon size. Also, two modes of knot patterns are observed, and evidence indicates that the so-called non-local type is dominant in small tube sizes. Evidence for the characteristics of 2SAPs is less conclusive, but its study has opened up many questions of interest for future study.

5.3 Future Work

Although an improvement from previous works, transfer matrices have been limited to the tube sizes of 3×2 and 5×1 for SAPs, and 2×2 and 4×1 for 2SAPs. There is still potential

to create transfer matrices for larger tube sizes, but it is expected to require a significant improvement regarding memory requirements. The advantage of using transfer matrices to generate polygons is that completely independent samples can be obtained directly from the desired Boltzmann distribution. However, the signifcant draw back is that the transfer matrix must first be computed and held in memory during computation. For larger tube sizes, another different sampling algorithm (e.g. PERM [24], Wang-Landau [33], multiple Markov Chain [62]) which does not require a transfer matrix could be applied. If polygons from larger tube sizes are able to be generated, it would be interesting to see how the probabilities of the two modes of knot patterns changes, and if there's a tube size where local knot patterns begin to dominate.

By using the programs created during my Ph.D., larger span SAPs and 2SAPs can be generated. The transition probabilites can also be tweaked to sample from different desired Boltzmann distributions. The work during this thesis has already created a large database of random independent uniform samples of SAPs and 2SAPs in small tube sizes, with large spans (see Tables C.1, C.2, C.3, and C.4 for all of the cases). These samples can be used to explore other questions of interest about polymers, such as the effect enzymes have when acting on DNA.

There are also still many open questions regarding the linking of 2SAPs. Knotplot limits the link-identification of two component links to only 9 crossings, and a lack of a "slicing method" (described in Section 2.4.3) for 2SAPs limits the results to lower spans. This limits the conclusions which can be drawn about the asymptotics of 2SAPs. Future work here includes identifying the link-type of longer span 2SAPs, perhaps by first simplifying the 2SAP by slicing an individual polygon in the 2SAP (isolating a knotted factor). There is also potential to divide 2SAPs at its 4-sections to create two 2-string tangles and use that to explore the complexity of the unlink or other link-types. Also regarding 2SAPs, (as mentioned in Section 4.4) there are open questions involving the exponential growth rates of untangled unlinks and 2SAPs with various linking number and unlinking number.

References

[1] C. Adams. *The knot book: an elementary introduction to the mathematical theory of knots*. American Mathematical Soc., 2004.

[2] S.E. Alm and S. Janson. Random self-avoiding walks on one-dimensional lattices. *Stochastic Models*, 6(2):169–212, 1990.

[3] J. Arsuaga, M. Vázquez, S. Trigueros, and J. Roca. Knotting probability of DNA molecules confined in restricted volumes: DNA knotting in phage capsids. *Proceedings of the National Academy of Sciences*, 99(8):5373–5377, 2002.

[4] M. Atapour. *Topological entanglement complexity of systems of polygons and walks in tubes*. PhD thesis, University of Saskatchewan, 2008.

[5] M. Atapour, N. R. Beaton, J. W. Eng, K. Ishihara, K. Shimokawa, C. E. Soteros, and M. Vazquez. Unknotting operations on 4-plat diagrams and the entanglement statistics of polygons in a lattice tube. In preparation.

[6] M. Atapour, C.E. Soteros, C. Ernst, and S.G. Whittington. The linking probability for 2-component links which span a lattice tube. *Journal of Knot Theory and Its Ramifications*, 19(1):27–54, 2010.

[7] M. Atapour, C.E. Soteros, and S.G. Whittington. Stretched polygons in a lattice tube. *Journal of Physics A: Mathematical and Theoretical*, 42(32):322002, 2009.

[8] E. Beamish, V. Tabard-Cossa, and M. Godin. Identifying structure in short dna scaffolds using solid-state nanopores. *ACS sensors*, 2(12):1814–1820, 2017.

[9] N.R. Beaton. The critical pulling force for self-avoiding walks. *Journal of Physics A: Mathematical and Theoretical*, 48:16FT03, 2015.

[10] N.R. Beaton, J.W. Eng, K. Ishihara, K. Shimokawa, and C.E. Soteros. Characterising knotting properties of polymers in nanochannels. *Soft matter*, 14(28):5775–5785, 2018.

[11] N.R. Beaton, J.W. Eng, and C.E. Soteros. Asymptotics of polygons in restricted geometries subjected to a force. *Journal of Physics A: Mathematical and Theoretical*, 49:424002, 2016.

[12] N.R. Beaton, J.W. Eng, and C.E. Soteros. Knotting statistics for polygons in lattice tubes. *Journal of Physics A: Mathematical and Theoretical*, 2019.

[13] N.R. Beaton, A.J. Guttmann, I. Jensen, and G.F. Lawler. Compressed self-avoiding walks, bridges, and polygons. *Journal of Physics A: Mathematical and Theoretical*, 48:454001, 2015.

[14] D. Buck. DNA topology. *Applications of knot theory (Proc. Sympos. Appl. Math., 66, Amer. Math. Soc., 2009)*, pages 47–79, 2009.

[15] M. Caraglio, E. Orlandini, and S.G. Whittington. Translocation of links through a pore: effects of link complexity and size. *Journal of Statistical Mechanics: Theory and Experiment*, 2020(4):043203, 2020.

[16] N. Clisby, R. Liang, and G. Slade. Self-avoiding walk enumeration via the lace expansion. *Journal of Physics A: Mathematical and Theoretical*, 40(36):10973, 2007.

[17] P.R. Cromwell. *Knots and links*. Cambridge University Press, 2004.

[18] M. Delbruck. Mathematical problems in the biological sciences. In *Proc. Symp. Appl. Math.*, volume 14, page 55, 1962.

[19] J. Emert and C. Ernst. N-string tangles. *Journal of knot theory and its ramifications*, 9(08):987–1004, 2000.

[20] J.W. Eng. Self-avoiding polygons in (L, M)-tubes. Master's thesis, University of Saskatchewan, 2014.

[21] O. Farago, Y. Kantor, and M. Kardar. Pulling knotted polymers. *EPL (Europhysics Letters)*, 60(1):53, 2002.

[22] P.J. Flory. The configuration of real polymer chains. *The Journal of Chemical Physics*, 17(3):303–310, 1949.

[23] H.L. Frisch and E. Wasserman. Chemical topology. *Journal of the American Chemical Society*, 83(18):3789–3795, 1961.

[24] P. Grassberger. Pruned-enriched rosenbluth method: Simulations of θ polymers of chain length up to 1 000 000. *Physical Review E*, 56(3):3682, 1997.

[25] L. Huang and D.E. Makarov. The rate constant of polymer reversal inside a pore. *The Journal of Chemical Physics*, 128(11):114903, 2008.

[26] D. Ioffe and Y. Velenik. The statistical mechanics of stretched polymers. *Brazilian Journal of Probability and Statistics*, 24:279–299, 2010.

[27] K. Ishihara, M. Pouokam, A. Suzuki, R. Scharein, M. Vazquez, J. Arsuaga, and K. Shimokawa. Bounds for minimum step number of knots confined to tubes in the simple cubic lattice. *Journal of Physics A: Mathematical and Theoretical*, 50:215601, 2017.

[28] A. Kloczkowski and R.L. Jernigan. Transfer matrix method for enumeration and generation of compact self-avoiding walks. I. square lattices. *The Journal of Chemical Physics*, 109(12):5134–5146, 1998.

[29] A. Kloczkowski and R.L. Jernigan. Transfer matrix method for enumeration and generation of compact self-avoiding walks. II. cubic lattice. *The Journal of Chemical Physics*, 109(12):5147–5159, 1998.

[30] K. Kodama. Knot. http://www.artsci.kyushu-u.ac.jp/ sumi/C/knot/.

[31] P. Kohn. Unlinking two component links. *Osaka Journal of Mathematics*, 30(4):741–752, 1993.

[32] A. Krawczyk, A.L. Owczarek, T. Prellberg, and A. Rechnitzer. Pulling absorbing and collapsing polymers from a surface. *Journal of Statistical Mechanics–Theory and Experiment*, page page P05008, 2005.

[33] D.P. Landau, S. Tsai, and M. Exler. A new approach to Monte Carlo simulations in statistical physics: Wang-landau sampling. *American Journal of Physics*, 72(10):1294–1302, 2004.

[34] D. Marenduzzo, C. Micheletti, and E. Orlandini. Biopolymer organization upon confinement. *Journal of Physics: Condensed Matter*, 22(28):283102, 2010.

[35] D. Marenduzzo, E. Orlandini, A. Stasiak, D.W. Sumners, L. Tubiana, and C. Micheletti. DNA-DNA interactions in bacteriophage capsids are responsible for the observed DNA knotting. *Proceedings of the National Academy of Sciences of the United States of America*, 106:22269–22274, 2009.

[36] C. Micheletti, D. Marenduzzo, and E. Orlandini. Polymers with spatial or topological constraints: Theoretical and computational results. *Physics Reports*, 504(1):1–73, 2011.

[37] C. Micheletti, D. Marenduzzo, E. Orlandini, and D.W. Summers. Knotting of random ring polymers in confined spaces. *The Journal of Chemical Physics*, 124(6):064903, 2006.

[38] C. Micheletti and E. Orlandini. Knotting and metric scaling properties of DNA confined in nano-channels: a monte carlo study. *Soft Matter*, 8(42):10959–10968, 2012.

[39] E. Orlandini. Statics and dynamics of DNA knotting. *Journal of Physics A: Mathematical and Theoretical*, 51(5):053001, 2017.

[40] E. Orlandini, E.J. Janse Van Rensburg, M.C. Tesi, and S.G. Whittington. Random linking of lattice polygons. *Journal of Physics A: Mathematical and General*, 27(2):335, 1994.

[41] E. Orlandini and S.G. Whittington. Statistical topology of closed curves: Some applications in polymer physics. *Reviews of modern physics*, 79(2):611, 2007.

[42] W.J.C. Orr. Statistical treatment of polymer solutions at infinite dilution. *Transactions of the Faraday Society*, 43:12–27, 1947.

[43] N. Pippenger. Knots in random walks. *Discrete Applied Mathematics*, 25(3):273 – 278, 1989.

[44] C. Plesa, D. Verschueren, S. Pud, J. van der Torre, J.W. Ruitenberg, M.J. Witteveen, M.P. Jonsson, A.Y. Grosberg, Y. Rabin, and C. Dekker. Direct observation of DNA knots using a solid-state nanopore. *Nature Nanotechnology*, 11:1093–1097, 2016.

[45] V.V. Rybenkov, N.R. Cozzarelli, and A.V. Vologodskii. Probability of DNA knotting and the effective diameter of the DNA double helix. *Proceedings of the National Academy of Sciences*, 90(11):5307–5311, 1993.

[46] V.V. Rybenkov, C. Ullsperger, A.V. Vologodskii, and N.R. Cozzarelli. Simplification of dna topology below equilibrium values by type ii topoisomerases. *Science*, 277(5326):690–693, 1997.

[47] A.F. Sauer-Budge, J.A. Nyamwanda, D.K. Lubensky, and D. Branton. Unzipping kinetics of double-stranded DNA in a nanopore. *Physical Review Letters*, 90(23):238101, 2003.

[48] H.H. Schaefer. *Banach lattices*. Springer, 1974.

[49] R. Scharein. The knotplot site. http://knotplot.com.

[50] R. Scharein, K. Ishihara, J. Arsuaga, Y. Diao, K. Shimokawa, and M. Vazquez. Bounds for the minimum step number of knots in the simple cubic lattice. *Journal of Physics A: Mathematical and Theoretical*, 42:275006, 2009.

[51] S.Y. Shaw and J.C. Wang. Knotting of a DNA chain during ring closure. *Science*, 260(5107):533–536, 1993.

[52] S.Y. Shaw and J.C. Wang. DNA knot formation in aqueous solutions. *Journal of Knot Theory and its Ramifications*, 3(03):287–298, 1994.

[53] K. Shimokawa. private communication.

[54] C.E. Soteros. Knots in graphs in subsets of $\mathbb{Z}^3$. In *Topology and geometry in polymer science*, pages 101–133. Springer, 1998.

[55] C.E. Soteros and S.G. Whittington. Lattice models of branched polymers: Effects of geometrical constraints. *Journal of Physics A: Mathematical and General*, 22(24):5259, 1989.

[56] R.P. Stanley. What is enumerative combinatorics? In *Enumerative combinatorics*, pages 1–63. Springer, 1986.

[57] M.J. Steele. *Probability theory and combinatorial optimization*. SIAM, 1997.

[58] R. Stolz, M. Yoshida, R. Brasher, M. Flanner, K. Ishihara, D.J. Sherratt, K. Shimokawa, and M. Vazquez. Pathways of DNA unlinking: A story of stepwise simplification. *Scientific reports*, 7(1):1–11, 2017.

[59] A. Suma and C. Micheletti. Pore translocation of knotted DNA rings. *Proceedings of the National Academy of Sciences of the United States of America*, 114:E2991–E2997, 2017.

[60] D.W. Sumners and S.G. Whittington. Knots in self-avoiding walks. *Journal of Physics A: Mathematical and General*, 21(7):1689, 1988.

[61] M.C. Tesi, E.J. Janse Van Rensburg, E. Orlandini, and S.G. Whittington. Interacting self-avoiding walks and polygons in three dimensions. *Journal of Physics A: Mathematical and General*, 29(10):2451, 1996.

[62] M.C. Tesi, E.J. Janse Van Rensburg, E. Orlandini, and S.G. Whittington. Monte carlo study of the interacting self-avoiding walk model in three dimensions. *Journal of statistical physics*, 82(1-2):155–181, 1996.

[63] M.C. Tesi, E.J. Janse Van Rensburg, E. Orlandini, and S.G. Whittington. Topological entanglement complexity of polymer chains in confined geometries. In *Topology and Geometry in Polymer Science*, pages 135–157. Springer, 1998.

[64] C.J. Thompson. *Mathematical statistical mechanics*. Princeton University Press, 2015.

[65] L. Tubiana, E. Orlandini, and C. Micheletti. Probing the entanglement and locating knots in ring polymers: a comparative study of different arc closure schemes. *Progress of Theoretical Physics Supplement*, 191:192–204, 2011.

[66] E. J. Janse Van Rensburg, E. Orlandini, M.C. Tesi, and S.G. Whittington. Knotting in stretched polygons. *Journal of Physics A: Mathematical and Theoretical*, 41:015003, 2008.

[67] E.J. Janse van Rensburg. The statistical mechanics of interacting walks, polygons, animals and vesicles. *Oxford Lecture Series in Mathematics and its Applications*, 18, 2000.

[68] E.J. Janse Van Rensburg. Thoughts on lattice knot statistics. *Journal of mathematical chemistry*, 45(1):7, 2009.

[69] E.J. Janse Van Rensburg and S.G. Whittington. The knot probability in lattice polygons. *Journal of Physics A: Mathematical and General*, 23(15):3573, 1990.

[70] E.J. Janse Van Rensburg and S.G. Whittington. The BFACF algorithm and knotted polygons. *Journal of Physics A: Mathematical and General*, 24:5553–5567, 1991.

[71] C. Vanderzande. *Lattice models of polymers*, volume 11. Cambridge University Press, 1998.

[72] S.A. Wasserman and N.R. Cozzarelli. Biochemical topology: applications to DNA recombination and replication. *Science*, 232(4753):951–960, 1986.

[73] E.T. Whittaker and G. Robinson. *The calculus of observations: an introduction to numerical analysis*. Dover Publications, 1967.

[74] S.G. Whittington. Statistical mechanics of polymer solutions and polymer adsorption. *Adv. Chem. Phys*, 51(1), 1982.

[75] W. Wickner and R. Schekman. Protein translocation across biological membranes. *science*, 310(5753):1452–1456, 2005.

[76] T. Williams and C. Kelley. Gnuplot. www.gnuplot.info.

[77] R.J. Wood and M.J. O'Neill. An always convergent method for finding the spectral radius of an irreducible non-negative matrix. *ANZIAM Journal*, 45:474–485, 2003.

[78] M. Zwolak and M. Di Ventra. Colloquium: Physical approaches to DNA sequencing and detection. *Reviews of Modern Physics*, 80(1):141, 2008.

APPENDIX A

COMPUTATIONAL RESOURCES

Table A.1 The approximate amount of resources required to create the transfer matrices for SAPs in each of the above cases. Cases larger than the 2×2 tube were run on Compute Canada's Graham and Cedar clusters. The amount of time required for generating each set of sampled SAPs at different spans is also available upon request.

Type	Tube	CPU Time (dd:hh:mm)	RAM
SAP	2x1	00:00:02	<1 GB
SAP	3x1	00:00:11	<1 GB
SAP	2x2	00:00:24	<1 GB
SAP	4x1	00:04:00	5 GB
SAP	5x1	05:22:52	350 GB
SAP	3x2	06:21:35	400 GB
Ham. SAP	2x1	00:00:02	<1 GB
Ham. SAP	3x1	00:00:05	<1 GB
Ham. SAP	2x2	00:00:07	<1 GB
Ham. SAP	4x1	00:01:00	2 GB
Ham. SAP	5x1	02:01:13	110 GB
Ham. SAP	3x2	02:06:30	150 GB

Table A.2 The approximate amount of resources required to create the transfer matrices for 2SAPs in each of the above cases. All of these cases were run on the University of Saskatchewan Math+Stats Department's local computers. The amount of time required for generating each set of sampled 2SAPs at different spans is also available upon request.

Type	Tube	CPU Time (dd:hh:mm)
2SAP	2x1	00:00:01
2SAP	3x1	00:00:06
2SAP	2x2	00:00:58
2SAP	4x1	00:13:19
Ham. 2SAP	2x1	00:00:01
Ham. 2SAP	3x1	00:00:04
Ham. 2SAP	2x2	00:00:14
Ham. 2SAP	4x1	00:04:59

APPENDIX B

LINKING NUMBER RESULTS

Table B.1 Exact 2SAP linking number results (absolute value).

Tube	Span	# of 2SAPs	1	2	3
1×1	all	2	0	0	0
2×1	1	72	0	0	0
2×1	2	623	0	0	0
2×1	3	5,609	8	0	0
2×1	4	51,046	198	0	0
2×1	5	467,109	3,458	0	0
2×1	6	4,288,906	50,953	0	0
2×1	7	39,482,621	680,230	16	0
2×1	8	364,275,071	8,511,359	796	0
2×1	9	3,367,542,877	101,738,596	27,958	0
2×1	10	31,187,474,516	1,175,382,854	715,465	0
2×1	11	289,312,967,970	13,226,489,847	14,802,872	32
3×1	1	1,334	0	0	0
3×1	2	77,030	72	0	0
3×1	3	4,622,536	33,464	2	0
3×1	4	281,352,953	5,021,040	2,878	0
3×1	5	17,280,501,131	543,421,628	972,273	0

Table B.2 Exact Hamiltonian 2SAP linking number results (absolute value).

Tube	Span	# of 2SAPs	1	2	3	4
1×1	all	2	0	0	0	0
2×1	1	21	0	0	0	0
2×1	2	91	0	0	0	0
2×1	3	537	8	0	0	0
2×1	4	2,623	46	0	0	0
2×1	5	14,809	542	0	0	0
2×1	6	75,966	3,258	0	0	0
2×1	7	419,979	26,083	16	0	0
2×1	8	2,213,901	160,470	156	0	0
2×1	9	12,127,972	1,104,425	3,164	0	0
2×1	10	65,030,655	6,779,625	29,406	0	0
2×1	11	355,727,584	43,386,541	314,410	32	0
2×1	12	1,925,130,971	263,245,172	2,587,674	440	0
2×1	13	10,703,569,500	1,618,797,619	189,980,091	12,936	0
2×1	14	57,387,975,128	9,691,389,431	164,433,536	168,236	0
3×1	1	139	0	0	0	0
3×1	2	2,782	18	0	0	0
3×1	3	65,121	988	2	0	0
3×1	4	1,451,096	47,490	228	0	0
3×1	5	33,755,040	1,740,206	17,639	0	0
3×1	6	780,310,655	58,322,308	926,894	158	0
3×1	7	18,307,336,975	1,806,293,005	41,571,171	41,800	4

Table B.3 The linking numbers of the sampled 2SAPs (absolute value)

Tube	Span	Total	0	1	2	3	4	5	6	7	8	9	10	11
2x1	10	1,000,000	962,058	37,914	28	0	0	0	0	0	0	0	0	0
2x1	20	1,000,000	866,301	131,892	1,807	0	0	0	0	0	0	0	0	0
2x1	30	1,000,000	761,587	229,308	9,018	87	0	0	0	0	0	0	0	0
2x1	40	1,000,000	672,914	304,723	21,823	538	2	0	0	0	0	0	0	0
2x1	50	1,000,000	598,596	361,383	38,338	1,651	31	1	0	0	0	0	0	0
2x1	60	1,000,000	538,710	399,712	57,666	3,782	129	1	0	0	0	0	0	0
2x1	70	1,000,000	490,712	425,617	76,618	6,726	319	8	0	0	0	0	0	0
2x1	80	1,000,000	451,496	441,571	95,548	10,697	671	17	0	0	0	0	0	0
2x1	90	1,000,000	419,015	451,323	113,022	15,357	1,236	47	0	0	0	0	0	0
2x1	100	1,000,000	391,335	456,050	129,363	21,058	2,070	115	9	0	0	0	0	0
3x1	10	1,000,000	872,712	124,550	2,731	7	0	0	0	0	0	0	0	0
3x1	20	1,000,000	662,577	308,049	28,403	957	14	0	0	0	0	0	0	0
3x1	30	1,000,000	516,714	405,865	71,165	5,978	272	6	0	0	0	0	0	0
3x1	40	1,000,000	424,516	444,761	113,403	16,022	1,243	54	1	0	0	0	0	0
3x1	50	1,000,000	364,840	453,877	148,632	28,795	3,570	272	14	0	0	0	0	0
3x1	60	1,000,000	322,909	448,142	177,033	43,814	7,197	831	71	3	0	0	0	0
3x1	70	1,000,000	293,318	435,401	198,043	59,231	12,133	1,699	162	13	0	0	0	0
3x1	80	1,000,000	271,322	421,996	212,318	72,812	17,812	3,250	445	40	5	0	0	0
3x1	90	1,000,000	252,433	408,589	222,253	86,378	24,341	5,023	858	114	10	1	0	0
3x1	100	1,000,000	237,672	394,634	229,968	97,839	30,754	7,450	1,454	205	23	1	0	0
4x1	10	1,000,000	826,902	166,465	6,593	39	1	0	0	0	0	0	0	0
4x1	20	1,000,000	580,668	365,256	51,011	2,998	66	1	0	0	0	0	0	0
4x1	30	1,000,000	438,831	439,028	107,203	13,951	947	40	0	0	0	0	0	0
4x1	40	1,000,000	359,736	451,562	153,361	31,186	3,839	302	13	1	0	0	0	0
4x1	50	1,000,000	309,485	443,123	186,470	50,431	9,191	1,206	84	10	0	0	0	0
4x1	60	1,000,000	275,945	426,124	209,435	69,184	16,174	2,755	355	26	2	0	0	0
4x1	70	1,000,000	251,526	408,172	222,702	86,770	24,613	5,269	833	100	11	4	0	0
4x1	80	1,000,000	233,506	390,143	231,758	101,225	33,172	8,316	1,590	268	19	3	0	0
4x1	90	1,000,000	218,632	373,959	236,492	113,376	41,985	12,098	2,858	511	76	12	1	0
4x1	100	1,000,000	206,056	358,524	239,430	123,839	50,506	16,321	4,206	947	149	19	3	0
2x2	10	1,000,000	702,480	288,777	8,695	48	0	0	0	0	0	0	0	0
2x2	20	1,000,000	496,121	437,486	63,022	3,293	75	3	0	0	0	0	0	0
2x2	30	1,000,000	392,725	467,492	122,954	15,779	1,004	45	1	0	0	0	0	0
2x2	40	1,000,000	332,698	460,932	167,762	34,037	4,230	323	18	0	0	0	0	0
2x2	50	1,000,000	295,874	441,534	197,006	54,797	9,605	1,085	95	4	0	0	0	0
2x2	60	1,000,000	265,956	423,678	216,571	73,802	16,930	2,712	320	31	0	0	0	0
2x2	70	1,000,000	245,928	403,419	228,778	90,350	25,423	5,225	786	83	8	0	0	0
2x2	80	1,000,000	228,441	387,538	234,489	104,557	34,427	8,663	1,630	222	29	3	0	1
2x2	90	1,000,000	215,223	370,879	239,110	116,267	42,814	12,388	2,776	464	73	5	1	0
2x2	100	1,000,000	203,984	356,323	240,315	126,077	51,554	16,530	4,178	880	131	21	7	0

Table B.4 The linking numbers of the sampled Hamiltonian 2SAPs (absolute value)

Tube	Span	Total	0	1	2	3	4	5	6	7	8	9	10	11
2x1	10	1,000,000	893,752	105,782	466	0	0	0	0	0	0	0	0	0
2x1	20	1,000,000	730,879	257,350	11,654	117	0	0	0	0	0	0	0	0
2x1	30	1,000,000	600,605	361,330	36,705	1,344	16	0	0	0	0	0	0	0
2x1	40	1,000,000	508,470	418,319	68,095	4,962	152	2	0	0	0	0	0	0
2x1	50	1,000,000	442,948	446,476	98,973	10,949	624	29	1	0	0	0	0	0
2x1	60	1,000,000	394,617	456,691	128,073	18,919	1,620	78	2	0	0	0	0	0
2x1	70	1,000,000	358,252	457,658	151,496	28,996	3,325	260	13	0	0	0	0	0
2x1	80	1,000,000	329,775	453,847	170,964	39,160	5,645	566	42	1	0	0	0	0
2x1	90	1,000,000	306,867	444,994	188,277	50,019	8,711	1,045	79	8	0	0	0	0
2x1	100	1,000,000	289,248	434,475	201,635	60,294	12,429	1,727	182	10	0	0	0	0
3x1	10	1,000,000	816,509	175,021	8,397	73	0	0	0	0	0	0	0	0
3x1	20	1,000,000	578,959	364,073	53,300	3,558	107	3	0	0	0	0	0	0
3x1	30	1,000,000	441,615	434,348	107,872	14,873	1,234	54	4	0	0	0	0	0
3x1	40	1,000,000	361,226	448,969	152,824	32,357	4,208	392	24	0	0	0	0	0
3x1	50	1,000,000	311,331	441,035	185,622	51,176	9,439	1,289	100	8	0	0	0	0
3x1	60	1,000,000	277,083	424,578	208,283	69,887	16,728	3,023	378	38	2	0	0	0
3x1	70	1,000,000	252,880	407,455	221,940	86,474	24,867	5,352	908	117	7	0	0	0
3x1	80	1,000,000	234,707	389,911	230,431	101,262	33,004	8,574	1,790	276	39	6	0	0
3x1	90	1,000,000	219,938	373,907	235,607	112,910	41,598	12,460	2,919	561	90	9	1	0
3x1	100	1,000,000	206,279	359,906	238,280	122,866	50,286	16,745	4,462	960	185	26	5	0
4x1	10	1,000,000	773,358	211,725	14,656	259	2	0	0	0	0	0	0	0
4x1	20	1,000,000	515,910	398,367	77,519	7,789	404	11	0	0	0	0	0	0
4x1	30	1,000,000	384,940	444,796	139,946	26,875	3,203	231	9	0	0	0	0	0
4x1	40	1,000,000	315,528	439,708	183,978	50,139	9,314	1,216	113	4	0	0	0	0
4x1	50	1,000,000	273,089	420,770	210,721	73,207	18,372	3,316	478	40	7	0	0	0
4x1	60	1,000,000	244,043	398,964	226,995	93,149	28,599	6,757	1,283	186	21	3	0	0
4x1	70	1,000,000	222,740	378,880	234,852	109,371	39,721	11,308	2,583	475	59	9	2	0
4x1	80	1,000,000	207,156	359,402	238,919	122,675	49,884	16,417	4,346	976	187	32	6	0
4x1	90	1,000,000	193,350	344,020	238,973	133,075	59,672	22,014	6,685	1,768	362	70	9	2
4x1	100	1,000,000	184,145	328,735	237,486	140,651	68,404	27,635	9,400	2,717	681	124	20	2
2x2	11	1,000,000	621,936	354,908	22,775	379	2	0	0	0	0	0	0	0
2x2	21	1,000,000	434,787	459,702	96,016	9,074	413	8	0	0	0	0	0	0
2x2	31	1,000,000	345,469	463,213	158,311	29,421	3,330	248	8	0	0	0	0	0
2x2	41	1,000,000	294,893	443,815	196,411	54,054	9,612	1,115	94	6	0	0	0	0
2x2	51	1,000,000	261,666	419,437	219,515	76,945	18,803	3,204	398	30	2	0	0	0
2x2	61	1,000,000	237,312	396,570	232,601	96,828	28,957	6,520	1,054	145	13	0	0	0
2x2	71	1,000,000	219,220	376,858	238,236	112,010	39,856	11,095	2,257	411	48	8	0	1
2x2	81	1,000,000	205,208	358,278	241,216	123,942	50,399	15,936	4,039	850	112	15	5	0
2x2	91	1,000,000	193,625	342,925	240,882	134,048	59,234	21,265	6,143	1,536	285	45	12	0
2x2	101	1,000,000	183,375	329,446	238,985	141,098	68,365	26,985	8,719	2,365	550	100	11	1

APPENDIX C

MONTE CARLO RESULTS

Table C.1 Summary of the generated Monte Carlo SAPs. Knot-types are only listed for the prime knots: $3_1, 4_1, 5_1, 5_2, 6_1, 6_2, 6_3$, but obviously many more prime and composite knot-types were observed. The notation of the header "cF" refers to the number of knot-types with c factors. The header "KNOTTED" just reports the number of knotted SAPs.

Tube	Span	Total	3_1	4_1	5_1	5_2	6_1	6_2	6_3	1F	2F	3F	4F	5F	6F	7F	8F	9F	10F	11F	12F	13F	KNOTTED
2x2	50	1,000,000	18,904	483	41	45	1	2	1	19,478	158	4	0	0	0	0	0	0	0	0	0	0	19,640
2x2	100	1,000,000	38,686	1,040	51	90	3	1	1	39,872	755	12	0	0	0	0	0	0	0	0	0	0	40,639
2x2	150	1,000,000	57,761	1,550	98	132	12	2	3	59,599	1,829	33	0	0	0	0	0	0	0	0	0	0	61,461
2x2	200	1,000,000	75,310	2,127	158	193	5	11	1	77,807	3,215	73	1	0	0	0	0	0	0	0	0	0	81,096
2x2	250	1,000,000	93,469	2,510	160	200	16	6	2	96,363	4,954	155	3	0	0	0	0	0	0	0	0	0	101,475
2x2	300	1,000,000	109,865	3,021	223	274	8	9	3	113,409	7,009	268	8	0	0	0	0	0	0	0	0	0	120,694
2x2	350	1,000,000	125,634	3,434	246	304	12	6	4	129,641	9,785	469	14	0	0	0	0	0	0	0	0	0	139,909
2x2	400	1,000,000	140,629	3,835	264	312	7	10	4	145,054	12,094	635	28	0	0	0	0	0	0	0	0	0	157,811
2x2	450	1,000,000	154,704	4,245	350	366	9	8	6	159,695	15,397	922	54	3	0	0	0	0	0	0	0	0	176,071
2x2	500	1,000,000	168,404	4,599	316	409	13	11	4	173,761	18,575	1,244	65	4	0	0	0	0	0	0	0	0	193,649
2x2	550	1,000,000	181,734	4,929	345	423	16	11	4	187,466	22,034	1,680	112	1	0	0	0	0	0	0	0	0	211,293
2x2	600	1,000,000	193,744	5,230	377	460	22	14	5	199,857	25,595	2,129	130	1	1	0	0	0	0	0	0	0	227,713
2x2	700	1,000,000	216,349	6,070	455	509	16	20	5	223,138	33,640	3,362	233	24	2	0	0	0	0	0	0	0	260,399
2x2	800	1,000,000	237,358	6,609	447	539	32	16	4	245,011	42,250	4,860	399	27	3	0	0	0	0	0	0	0	292,550
2x2	900	1,000,000	255,550	7,115	487	585	24	16	7	263,788	51,106	6,447	644	47	3	0	0	0	0	0	0	0	322,035
2x2	1000	1,000,000	272,670	7,703	516	616	38	10	5	281,567	60,518	8,792	885	71	8	1	0	0	0	0	0	0	351,842
2x2	1200	886,852	266,458	7,191	508	609	30	12	9	274,824	71,166	12,092	1,580	155	9	0	0	0	0	0	0	0	359,826
4x1	50	1,000,000	26,565	757	80	79	6	0	1	27,488	352	2	0	0	0	0	0	0	0	0	0	0	27,842
4x1	100	1,000,000	53,168	1,573	195	175	10	7	2	55,133	1,498	23	0	0	0	0	0	0	0	0	0	0	56,654
4x1	150	1,000,000	78,472	2,271	306	239	12	9	2	81,313	3,309	100	1	0	0	0	0	0	0	0	0	0	84,723
4x1	200	1,000,000	102,258	2,968	359	306	20	19	1	105,935	6,079	211	2	0	0	0	0	0	0	0	0	0	112,227
4x1	250	1,000,000	124,796	3,628	437	377	25	20	6	129,295	9,519	440	8	0	0	0	0	0	0	0	0	0	139,262
4x1	300	1,000,000	145,815	4,294	492	454	21	28	6	151,109	13,201	738	38	0	0	0	0	0	0	0	0	0	165,086
4x1	350	1,000,000	166,124	4,901	546	539	25	27	9	172,181	17,661	1,196	59	1	0	0	0	0	0	0	0	0	191,098
4x1	400	1,000,000	183,422	5,410	592	551	39	30	5	190,060	22,444	1,808	101	3	0	0	0	0	0	0	0	0	214,416
4x1	450	984,538	197,620	5,910	693	597	41	39	14	204,924	27,074	2,434	157	11	1	0	0	0	0	0	0	0	234,601
4x1	500	1,000,000	216,890	6,401	728	682	39	30	3	224,791	33,438	3,224	251	5	1	1	0	0	0	0	0	0	261,711
4x1	550	1,000,000	230,202	6,870	805	731	44	25	4	238,698	38,868	4,199	354	27	0	0	0	0	0	0	0	0	282,146
4x1	600	968,519	235,726	7,187	823	753	41	41	11	244,593	43,973	5,179	449	24	2	0	0	0	0	0	0	0	294,220
4x1	700	1,000,000	268,404	8,140	941	830	45	39	7	278,418	58,046	8,018	828	64	3	0	0	0	0	0	0	0	345,377
4x1	800	1,000,000	288,087	8,818	974	843	68	37	13	298,864	71,893	11,200	1,294	148	14	0	0	0	0	0	0	0	383,413
4x1	900	1,000,000	305,855	9,104	1,062	963	62	33	10	317,106	86,000	15,401	2,092	205	17	3	0	0	0	0	0	0	420,824
4x1	1000	1,000,000	319,931	9,411	1,100	961	53	40	13	331,521	99,650	19,931	2,945	360	31	4	0	0	0	0	0	0	454,442
4x1	1200	1,000,000	339,912	10,278	1,129	1,160	60	59	8	352,620	127,252	30,549	5,591	818	82	10	0	0	0	0	0	0	516,922
5x1	50	1,000,000	57,942	3,053	407	432	26	33	9	61,913	1,655	22	0	0	0	0	0	0	0	0	0	0	63,590
5x1	100	1,000,000	111,487	6,284	829	874	67	77	23	119,675	7,311	257	2	0	0	0	0	0	0	0	0	0	127,245
5x1	150	1,000,000	157,841	8,857	1,157	1,341	116	108	39	169,509	16,391	976	45	1	0	0	0	0	0	0	0	0	186,922
5x1	200	1,000,000	197,905	10,938	1,426	1,649	148	119	29	212,281	28,155	2,403	136	6	1	0	0	0	0	0	0	0	242,982
5x1	250	1,000,000	230,711	12,739	1,659	1,917	155	124	49	247,440	41,777	4,391	362	15	1	0	0	0	0	0	0	0	293,986
5x1	300	1,000,000	258,069	14,683	1,872	2,296	195	156	73	277,430	56,717	7,531	669	55	1	1	0	0	0	0	0	0	342,404
5x1	350	1,000,000	278,412	15,676	2,025	2,418	217	160	65	299,070	71,558	11,271	1,189	104	10	0	0	0	0	0	0	0	383,202
5x1	400	1,000,000	297,426	16,838	2,204	2,564	219	193	65	319,612	87,974	15,561	2,077	212	14	2	0	0	0	0	0	0	425,452
5x1	450	726,131	228,375	13,039	1,716	1,934	158	129	54	245,502	76,652	15,487	2,334	255	16	0	0	0	0	0	0	0	340,246
5x1	500	1,000,000	325,978	18,644	2,395	2,856	231	200	71	350,508	121,577	27,485	4,501	648	70	10	0	0	0	0	0	0	504,799
5x1	600	1,000,000	340,167	19,411	2,501	3,014	253	215	70	365,755	152,623	42,212	8,320	1,279	177	22	0	0	0	0	0	0	570,388
3x2	50	1,000,000	85,301	5,197	689	865	101	51	22	92,268	3,821	73	1	0	0	0	0	0	0	0	0	0	96,163
3x2	100	1,000,000	157,166	9,993	1,415	1,785	139	103	50	170,729	16,462	970	39	0	0	0	0	0	0	0	0	0	188,200
3x2	150	1,000,000	215,029	13,503	1,908	2,461	224	179	62	233,488	35,352	3,238	245	8	0	0	0	0	0	0	0	0	272,331
3x2	200	1,000,000	258,705	16,525	2,200	3,006	300	199	86	281,200	57,849	7,738	642	63	4	0	0	0	0	0	0	0	347,496
3x2	250	1,000,000	291,339	18,586	2,646	3,380	304	205	87	316,756	82,034	13,460	1,586	151	9	2	0	0	0	0	0	0	413,998
3x2	300	1,000,000	314,007	19,970	2,771	3,651	335	249	100	341,286	107,282	21,754	3,176	370	34	0	0	0	0	0	0	0	473,902
3x2	350	1,000,000	328,941	21,046	2,797	3,884	366	278	115	357,636	132,666	31,924	5,658	732	67	6	0	0	0	0	0	0	528,689
3x2	400	1,000,000	338,010	21,666	2,920	3,867	367	270	120	367,457	155,634	42,996	8,622	1,401	164	19	5	0	0	0	0	0	576,298
3x2	450	1,000,000	341,670	21,676	2,990	3,941	356	268	117	371,249	177,642	55,736	12,756	2,297	316	37	6	0	0	0	0	0	620,039
3x2	500	1,000,000	341,725	21,516	3,006	3,885	353	275	109	371,119	197,806	68,800	17,681	3,625	633	75	7	1	1	0	0	0	659,748
3x2	550	1,000,000	336,700	21,611	2,830	3,831	351	242	105	365,890	214,791	82,652	23,427	5,255	959	148	15	3	1	0	0	0	693,141
3x2	600	1,000,000	329,355	21,294	2,901	3,721	331	248	103	358,194	230,258	97,298	30,416	7,461	1,540	233	41	5	1	0	0	0	725,447

Table C.2 Summary of the generated Hamiltonian Monte Carlo SAPs. Knot-types are only listed for the prime knots: $3_1, 4_1, 5_1, 5_2, 6_1, 6_2, 6_3$, but obviously many more prime and composite knot-types were observed. The notation of the header "cF" refers to the number of knot-types with c factors. The header "KNOTTED" just reports the number of knotted SAPs.

Tube	Span	Total	3_1	4_1	5_1	5_2	6_1	6_2	6_3	1F	2F	3F	4F	5F	6F	7F	8F	9F	10F	11F	12F	13F	KNOTTED
2x2	51	1,000,000	60,871	3,079	344	409	41	16	14	64,791	1,865	34	1	0	0	0	0	0	0	0	0	0	66,691
2x2	101	1,000,000	116,169	5,894	658	905	58	48	14	123,793	8,007	312	6	0	0	0	0	0	0	0	0	0	132,118
2x2	151	1,000,000	163,848	8,222	951	1,240	86	72	24	174,486	17,594	1,070	39	0	0	0	0	0	0	0	0	0	193,189
2x2	201	1,000,000	203,132	10,357	1,190	1,547	122	69	33	216,493	29,911	2,700	176	6	0	0	0	0	0	0	0	0	249,286
2x2	251	1,000,000	236,997	12,192	1,474	1,831	119	103	37	252,801	44,248	5,025	362	21	1	0	0	0	0	0	0	0	302,458
2x2	301	1,000,000	266,012	13,716	1,566	1,976	150	107	42	283,642	59,274	8,062	805	78	1	0	0	0	0	0	0	0	351,862
2x2	351	1,000,000	288,165	15,184	1,727	2,207	173	125	47	307,333	75,868	12,284	1,470	135	10	0	0	0	0	0	0	0	397,100
2x2	401	1,000,000	306,414	15,871	1,825	2,338	148	135	55	326,881	92,980	17,019	2,392	221	20	1	0	0	0	0	0	0	439,514
2x2	451	1,000,000	320,051	16,538	1,930	2,525	173	156	65	341,509	109,915	23,223	3,591	417	43	7	1	0	0	0	0	0	478,706
2x2	501	1,000,000	331,014	17,302	2,034	2,503	177	143	70	353,330	126,017	29,674	5,046	695	82	9	0	0	0	0	0	0	514,853
2x2	551	1,000,000	339,602	17,441	2,014	2,532	206	178	67	362,135	142,284	36,803	7,030	1,100	127	15	1	0	0	0	0	0	549,495
2x2	601	1,000,000	342,725	17,732	2,086	2,684	253	159	64	365,730	158,472	44,759	9,463	1,504	198	34	4	0	0	0	0	0	580,164
2x2	701	1,000,000	346,965	17,909	2,129	2,738	190	137	59	370,251	186,302	61,636	15,165	2,871	416	68	9	0	0	0	0	0	636,718
2x2	801	1,000,000	343,170	17,601	2,027	2,701	184	140	63	365,962	212,014	80,526	22,766	5,021	879	144	19	4	0	0	0	0	687,335
2x2	901	1,000,000	333,869	17,244	1,940	2,606	186	153	60	356,152	232,024	99,737	31,469	8,024	1,688	302	34	7	1	1	0	0	729,439
2x2	1001	1,000,000	320,864	16,828	1,894	2,654	176	138	61	342,702	247,699	118,671	41,869	11,917	2,772	535	114	6	1	0	0	0	766,286
2x2	1201	1,000,000	287,481	14,690	1,720	2,344	157	122	48	306,633	268,051	154,122	65,396	22,501	6,475	1,514	309	54	10	1	0	0	825,066
4x1	50	1,000,000	75,576	3,921	850	678	80	43	20	81,202	2,854	58	0	0	0	0	0	0	0	0	0	0	84,114
4x1	100	1,000,000	142,481	7,409	1,535	1,332	140	92	31	153,099	12,594	646	18	2	0	0	0	0	0	0	0	0	166,359
4x1	150	1,000,000	195,791	10,161	2,270	1,897	198	146	49	210,641	27,207	2,343	120	3	0	0	0	0	0	0	0	0	240,314
4x1	200	1,000,000	239,492	12,764	2,740	2,385	250	179	52	258,005	45,703	5,224	417	20	0	0	0	0	0	0	0	0	309,369
4x1	250	1,000,000	273,495	14,187	3,107	2,689	286	205	68	294,208	66,140	9,623	990	75	3	0	0	0	0	0	0	0	371,039
4x1	300	1,000,000	298,918	16,093	3,438	2,992	285	214	65	322,206	88,094	15,412	1,932	190	15	0	0	0	0	0	0	0	427,849
4x1	350	1,000,000	317,197	17,033	3,664	3,122	332	243	68	341,893	109,132	22,543	3,396	431	40	3	0	0	0	0	0	0	477,438
4x1	400	1,000,000	330,527	17,674	3,719	3,412	354	266	75	356,262	131,330	31,305	5,398	712	77	7F	1	0	0	0	0	0	525,085
4x1	450	1,000,000	339,983	17,883	3,996	3,429	363	261	77	366,213	151,193	41,070	8,233	1,270	159	19	1	0	0	0	0	0	568,158
4x1	500	1,000,000	343,820	18,510	4,031	3,477	364	278	79	370,761	170,624	51,885	11,355	1,946	301	28	3	0	0	0	0	0	606,903
4x1	550	1,000,000	342,599	18,132	3,960	3,452	351	245	86	369,078	188,977	62,793	15,280	2,948	468	56	14	1	1	0	0	0	639,616
4x1	600	1,000,000	341,418	18,255	4,002	3,545	382	254	65	368,152	205,860	74,796	20,666	4,221	761	84	9	2	0	0	0	0	674,551
4x1	700	1,000,000	331,016	17,404	3,648	3,363	350	266	64	356,326	232,514	99,673	31,548	7,818	1,640	295	38	3	2	0	0	0	729,857
4x1	800	1,000,000	313,388	16,593	3,648	3,251	339	241	69	337,728	252,002	123,782	45,363	13,163	3,039	663	109	14	3	1	0	0	775,867
4x1	900	1,000,000	291,629	15,603	3,315	3,026	284	227	75	314,388	265,461	147,309	60,616	19,808	5,342	1,162	207	39	11	1	0	0	814,344
4x1	1000	1,000,000	269,276	14,687	3,157	2,784	307	197	63	290,663	271,657	167,389	77,118	28,096	8,491	2,133	500	76	9	2	0	0	846,134
4x1	1200	1,000,000	222,654	11,758	2,607	2,259	250	181	46	239,905	269,722	200,032	111,530	48,857	17,385	5,366	1,491	343	75	16	4	4	894,730
5x1	50	1,000,000	124,376	10,123	2,278	2,502	343	250	98	140,362	9,071	249	2	0	0	0	0	0	0	0	0	0	149,684
5x1	100	1,000,000	215,228	17,924	4,082	4,396	641	436	153	243,701	37,193	3,180	187	4	0	0	0	0	0	0	0	0	284,265
5x1	150	1,000,000	274,805	23,015	5,258	5,678	749	612	223	311,534	74,537	10,725	1,054	58	3	0	0	0	0	0	0	0	397,911
5x1	200	1,000,000	309,658	25,863	5,977	6,466	924	679	244	351,172	114,907	23,299	3,256	331	20	3	1	0	0	0	0	0	492,989
5x1	250	1,000,000	325,923	27,533	6,303	6,896	952	722	279	370,136	154,490	40,222	7,437	1,051	96	6	0	0	0	0	0	0	573,438
5x1	300	1,000,000	330,962	27,619	6,460	6,940	999	727	266	375,523	188,908	60,933	13,988	2,423	342	28	4	0	0	0	0	0	642,149
5x1	350	1,000,000	325,274	27,272	6,261	7,004	999	731	253	369,307	218,350	82,800	22,797	4,713	807	125	9	0	0	0	0	0	698,908
5x1	400	1,000,000	313,707	26,249	6,087	6,628	884	683	268	356,065	240,941	105,719	33,910	7,982	1,632	234	33	3	2	0	0	0	746,521
5x1	450	1,000,000	296,219	24,590	5,863	6,339	871	632	234	336,123	258,799	128,398	46,721	13,153	2,928	539	66	15	0	0	0	0	786,742
5x1	500	980,000	271,492	23,044	5,277	5,903	787	599	231	308,697	264,148	146,861	59,399	18,798	4,957	1,061	186	31	5	0	0	0	804,143
5x1	550	812,534	207,423	17,599	4,089	4,504	599	454	186	235,808	224,844	137,714	61,790	21,804	6,254	1,442	308	54	8	0	0	0	690,026
5x1	600	722,033	170,498	14,246	3,380	3,707	477	368	141	193,656	198,998	134,506	66,756	25,660	7,993	2,128	474	92	12	0	0	0	630,275
3x2	50	1,000,000	164,903	15,150	3,019	3,911	494	388	152	188,737	188,114	776	17	0	0	0	0	0	0	0	0	0	377,644
3x2	100	1,000,000	265,084	24,991	4,980	6,496	856	657	251	304,833	67,775	8,416	687	42	1	0	0	0	0	0	0	0	381,754
3x2	150	1,000,000	312,845	29,622	5,932	7,877	1,044	795	350	360,362	125,923	26,867	3,888	427	27	0	0	0	0	0	0	0	517,494
3x2	200	1,000,000	326,557	31,257	6,237	8,419	1,056	849	361	376,719	179,449	53,441	11,296	1,720	215	19	2	0	0	0	0	0	622,861
3x2	250	1,000,000	320,010	30,372	6,123	7,938	1,097	855	392	368,846	223,709	85,139	23,226	4,546	783	100	8	0	0	0	0	0	706,357
3x2	300	1,000,000	301,492	28,478	5,793	7,715	1,000	775	322	347,438	252,515	118,396	33,970	10,317	2,134	321	41	4	0	0	0	0	765,136
3x2	350	1,000,000	273,298	26,210	5,249	6,992	876	729	315	315,509	271,120	150,190	60,006	18,566	4,609	909	150	31	1	1	0	0	821,092
3x2	400	1,000,000	244,547	23,537	4,689	6,323	798	656	286	282,435	278,258	176,779	82,248	29,665	8,611	2,062	385	73	9	0	0	0	860,525
3x2	450	1,000,000	214,902	20,538	4,231	5,604	758	595	251	248,280	276,155	198,226	105,592	43,243	14,407	3,985	923	184	38	5	0	0	891,038
3x2	500	1,000,000	186,399	17,994	3,610	4,673	614	473	200	215,177	265,913	216,305	127,745	58,400	22,180	6,930	1,842	426	91	18	2	0	915,029
3x2	550	1,000,000	160,205	14,964	3,044	3,963	531	427	195	184,333	252,697	226,403	147,705	75,828	31,581	11,040	3,311	820	177	37	5	1	933,938
3x2	600	1,000,000	136,868	13,175	2,666	3,512	438	361	163	158,159	235,119	230,012	164,464	93,689	42,738	16,378	5,396	1,577	402	106	17	1	948,058

Table C.3 Summary of the generated Monte Carlo 2SAPs. Note that not all link-types observed are shown in the table.

Tube	Span	Total	0_1^2	2_1^2	4_1^2	5_1^2	6_1^2	6_2^2	6_3^2	7_1^2	7_2^2	7_3^2	7_4^2	7_5^2	7_6^2	7_7^2	7_8^2	8_1^2	8_2^2	8_3^2	8_4^2	8_5^2	8_6^2	8_7^2	8_8^2	8_{10}^2	8_{11}^2	8_{12}^2	8_{15}^2	8_{16}^2
2x1	10	1000000	962058	37914	28	0	0	0	0	0	0	0	0	0	0	0	0	0	0	0	0	0	0	0	0	0	0	0	0	0
2x1	20	1000000	866298	131892	1807	3	0	0	0	0	0	0	0	0	0	0	0	0	0	0	0	0	0	0	0	0	0	0	0	0
2x1	30	1000000	761411	229308	9008	175	65	22	10	0	0	1	0	0	0	0	0	0	0	0	0	0	0	0	0	0	0	0	0	0
2x1	40	1000000	671882	304708	21745	1023	393	145	78	10	5	9	0	0	0	0	0	2	0	0	0	0	0	0	0	0	0	0	0	0
2x1	50	1000000	595785	361259	38073	2785	1139	506	262	78	46	25	0	0	0	0	0	17	13	6	1	0	2	0	0	0	0	0	0	0
2x1	60	1000000	532907	399295	56814	5689	2475	1278	824	258	152	111	0	0	0	0	0	66	56	14	7	14	19	4	0	0	0	0	0	0
2x1	70	1000000	480463	424559	74828	9948	4121	2472	1729	629	386	276	0	0	0	0	0	159	113	90	44	41	40	18	8	0	0	0	0	0
2x1	80	1000000	436023	439334	92500	14852	6359	4061	2870	1217	868	527	0	0	0	0	0	317	269	164	76	106	88	41	30	0	0	0	0	0
2x1	90	1000000	397778	447428	108299	20088	8864	5918	4343	2125	1455	923	0	0	0	0	0	478	579	339	143	208	191	74	62	0	0	0	0	0
2x1	100	1000000	363715	449773	122394	25625	11804	8193	6251	3238	2351	1505	0	0	0	0	0	740	979	580	255	411	300	178	114	0	0	0	0	0
3x1	10	1000000	872678	124550	2731	34	4	3	0	0	0	0	0	0	0	0	0	0	0	0	0	0	0	0	0	0	0	0	0	0
3x1	20	1000000	660513	307970	28234	2049	635	319	169	47	31	15	0	0	0	0	0	7	7	1	0	2	0	1	0	0	0	0	0	0
3x1	30	1000000	507047	404817	69645	9422	3847	2024	1463	629	378	225	0	0	0	0	0	126	114	60	30	45	19	15	13	0	0	0	0	0
3x1	40	1000000	402022	440341	108277	21360	9131	6163	4649	2303	1744	980	0	0	0	0	0	518	521	383	169	312	214	122	87	0	0	0	0	0
3x1	50	1000000	327625	442724	137978	34118	15229	11308	9022	5386	4241	2397	0	0	0	0	0	1219	1575	1126	528	946	603	388	325	0	0	0	0	0
3x1	60	1000000	270886	426872	158449	46022	21871	17029	14482	9640	7757	4269	0	0	0	0	0	2214	3125	2339	1121	1990	1215	841	726	0	0	0	0	0
3x1	70	1000000	227766	401945	170868	55410	27998	22214	19123	13992	11554	6579	0	0	0	0	0	3357	5127	4005	1866	3529	2125	1526	1314	0	0	0	0	0
3x1	80	1000000	193356	374826	175301	63023	32207	26705	23727	18440	15578	8627	0	0	0	0	0	4623	7098	5714	2814	5124	3158	2259	1972	0	0	0	0	0
3x1	90	1000000	165565	346404	175754	66655	36197	30082	26941	22578	19511	10415	0	0	0	0	0	5745	9187	7840	3699	6932	3905	3125	2758	0	0	0	0	0
3x1	100	1000000	141425	317458	172326	70166	38586	33146	29928	25949	22950	12475	0	0	0	0	0	6805	11188	9393	4558	8489	4884	3902	3614	0	0	0	0	0
4x1	10	1000000	826710	166463	6589	163	29	10	4	0	0	0	0	0	0	0	0	0	1	0	0	0	0	0	0	0	0	0	0	0
4x1	20	1000000	574589	364830	50274	5935	1918	1051	718	255	151	98	0	0	0	0	0	35	25	18	6	11	10	2	4	0	0	0	0	0
4x1	30	1000000	417557	434825	102707	20254	7999	5353	4151	2182	1638	822	2	0	0	1	1	356	435	311	135	271	159	110	95	0	0	0	0	0
4x1	40	1000000	318720	438352	141072	37553	16454	12205	10251	6278	4968	2642	0	0	0	1	2	1198	1693	1249	658	1067	697	489	415	0	0	0	0	0
4x1	50	1000000	249530	415410	163843	51919	24185	19411	16830	11832	10045	5357	0	3	0	8	3	2687	3909	3071	1513	2743	1543	1229	1038	0	0	0	0	0
4x1	60	1000000	199760	380005	174053	62332	30718	25722	23129	17957	15533	8096	1	2	0	5	2	4213	6426	5396	2660	4811	2759	2261	2022	0	1	1	0	0
4x1	70	1000000	162059	342974	174243	68428	35281	30596	27469	22859	20623	10772	2	4	0	3	5	5729	9309	8036	3727	7341	3978	3329	2988	0	0	0	0	0
4x1	80	1000000	133512	306553	169749	71362	38224	33633	30570	27076	24468	12977	4	0	0	4	4	6981	11693	10270	5017	9368	5173	4242	3910	0	0	0	0	0
4x1	90	1000000	110797	271800	160920	71692	39980	35183	32582	30216	27605	14145	2	1	0	5	5	7964	13795	12032	5824	10998	6191	5159	4827	0	1	3	0	0
4x1	100	1000000	91961	239545	150849	70200	39881	35656	33138	32095	29795	15432	3	4	0	9	7	8787	15087	13727	6702	12663	6861	5940	5610	0	1	5	0	0
2x2	10	1000000	702109	288777	8684	359	28	20	11	0	0	0	0	0	0	0	0	0	0	0	0	0	0	0	0	0	0	0	0	0
2x2	20	1000000	486152	436805	61572	9801	1741	1507	1429	354	272	153	0	0	0	2	1	20	38	22	16	22	12	12	10	0	0	0	0	0
2x2	30	1000000	361423	461515	115625	29760	7614	7252	6826	2737	2580	1333	2	0	0	1	1	251	466	485	241	396	254	203	182	0	0	0	0	0
2x2	40	1000000	278939	442732	150623	48841	15400	14978	14424	7649	7347	3803	5	3	0	4	3	1030	1892	1690	890	1684	856	814	739	0	0	2	0	0
2x2	50	1000000	221744	405824	167837	63805	23245	22529	21823	13489	13456	7039	0	1	0	4	5	2076	4041	3977	1969	3784	1967	1799	1768	0	2	0	0	0
2x2	60	1000000	177401	367229	173487	71567	29206	28378	27700	19927	19431	9929	5	6	0	6	5	3457	6624	6442	3201	6434	3348	3030	2974	0	3	1	0	0
2x2	70	1000000	144778	326385	171317	76278	33187	32666	31960	24563	24260	12544	6	3	0	1	8	4770	9164	9098	4415	8684	4467	4457	4153	0	1	4	0	0
2x2	80	1000000	118320	289557	163341	76976	35527	34839	34225	28863	28358	14423	4	4	0	5	9	5818	11571	11318	5721	11117	5657	5471	5310	0	2	5	0	0
2x2	90	1000000	98495	254984	153787	75306	36525	35919	35276	31270	30957	15856	2	5	0	8	3	6767	13406	13100	6575	12927	6612	6191	6219	0	2	5	0	0
2x2	100	1000000	82338	223510	142946	72376	36575	36119	35389	32757	32434	16475	8	4	0	5	8	7503	14768	14458	7314	13910	7184	7064	6906	0	2	3	0	0

Table C.4 Summary of the generated Hamiltonian Monte Carlo 2SAPs. Note that not all link-types observed are shown in the table.

Tube	Span	Total	0_1^2	2_1^2	4_1^2	5_1^2	6_1^2	6_2^2	6_3^2	7_1^2	7_2^2	7_3^2	7_4^2	7_5^2	7_6^2	7_7^2	7_8^2	8_1^2	8_2^2	8_3^2	8_4^2	8_5^2	8_6^2	8_7^2	8_8^2	8_{10}^2	8_{11}^2	8_{12}^2	8_{15}^2	8_{16}^2
2x1	10	1000000	893752	105782	466	0	0	0	0	0	0	0	0	0	0	0	0	0	0	0	0	0	0	0	0	0	0	0	0	0
2x1	20	1000000	730502	257350	11644	377	92	25	10	0	0	0	0	0	0	0	0	0	0	0	0	0	0	0	0	0	0	0	0	0
2x1	30	1000000	597679	361251	36426	2899	912	429	277	51	28	27	0	0	0	0	0	8	6	2	2	1	1	0	0	0	0	0	0	0
2x1	40	1000000	499686	417639	66874	8597	3194	1706	1181	406	259	179	0	0	0	0	0	75	64	32	12	30	22	6	3	0	0	0	0	0
2x1	50	1000000	425463	443896	95581	16837	6391	4257	3236	1394	1034	582	0	0	0	0	0	265	280	154	68	140	77	49	47	0	0	0	0	0
2x1	60	1000000	366718	450886	121457	26312	10488	7550	6000	2972	2269	1376	0	0	0	0	0	611	731	486	231	359	274	181	125	0	0	0	0	0
2x1	70	1000000	319910	446792	140396	35164	15499	11343	9580	5341	4223	2585	0	0	0	0	0	1125	1492	1111	512	900	547	325	279	0	0	0	0	0
2x1	80	1000000	280788	436148	154636	44002	19871	15438	13236	8207	6673	3762	0	0	0	0	0	1867	2474	1919	858	1567	1049	644	588	0	0	0	0	0
2x1	90	1000000	247862	419438	166156	51397	24275	19434	16926	11111	9395	5419	0	0	0	0	0	2572	3789	3012	1371	2514	1530	1056	906	0	0	0	0	0
2x1	100	1000000	220920	399881	172956	57969	28015	23103	20433	14213	12386	6829	0	0	0	0	0	3417	5214	4138	2068	3525	2192	1540	1367	0	0	0	0	0
2x1	125	1000000	167005	350127	176626	67935	35386	30462	27132	21971	19290	10728	0	0	0	0	0	5515	8745	7451	3608	6746	3923	2984	2621	0	0	0	0	0
3x1	10	1000000	816319	175020	8391	188	62	11	6	1	0	0	0	0	0	0	0	0	0	0	0	0	0	0	0	0	0	0	0	0
3x1	20	1000000	573781	363680	52686	5062	2347	1173	597	240	139	106	0	0	0	0	0	49	49	25	9	13	12	4	3	0	0	0	0	0
3x1	30	1000000	422805	430719	103747	17838	8921	5385	3716	1998	1340	838	0	0	0	0	0	487	557	301	156	247	170	79	47	0	0	0	0	0
3x1	40	1000000	324397	437035	141809	33461	17492	12292	9187	5925	4410	2544	0	0	0	0	1	1454	1917	1280	570	1046	629	373	289	0	0	0	0	0
3x1	50	1000000	256349	415894	164913	47384	25616	19294	15386	11226	8956	5179	1	0	0	2	1	2903	4063	2950	1385	2419	1527	969	817	0	0	0	0	0
3x1	60	1000000	205991	383035	175319	57924	32163	25620	21470	16863	13753	7928	0	0	0	1	1	4521	6840	5289	2609	4368	2644	1817	1559	0	0	0	0	0
3x1	70	1000000	168566	347994	176365	64816	36990	30289	26057	21990	18653	10291	1	1	0	2	3	6262	9455	7666	3695	6392	3989	2798	2474	0	2	0	0	0
3x1	80	1000000	138930	312165	172402	68723	40078	33705	29101	26423	22737	12515	1	0	0	0	1	7306	11804	9796	4778	8554	5040	3751	3269	0	0	0	0	0
3x1	90	1000000	115951	278366	164446	69651	41182	35272	31292	29338	25909	14083	2	0	0	0	0	8509	13945	11662	5751	10552	6058	4671	4059	0	0	0	0	0
3x1	100	1000000	96197	247741	154459	68474	41447	35873	32413	31582	27825	15177	0	0	0	0	5	9292	15605	13322	6720	11908	6855	5381	4913	0	1	0	0	0
4x1	10	1000000	772304	211666	14624	638	195	63	30	7	6	0	0	0	0	1	1	1	1	1	0	0	0	0	0	0	0	0	0	0
4x1	20	1000000	504576	396550	75686	10451	4882	2744	1690	904	534	316	3	2	0	11	7	168	184	87	43	72	52	18	22	1	0	0	0	1
4x1	30	1000000	352616	434887	130996	29295	15063	9923	7484	4765	3444	1951	7	5	0	32	39	1189	1389	948	420	768	466	295	242	0	2	1	0	0
4x1	40	1000000	259911	413793	163209	47678	25124	18702	15196	11218	8874	4886	15	22	0	39	27	2874	3966	2867	1358	2455	1477	1024	865	0	6	7	0	0
4x1	50	1000000	197647	374165	174916	60206	33065	26154	22212	18132	15072	8307	28	31	1	64	52	4898	7381	5773	2754	4985	3015	2084	1830	0	11	15	0	0
4x1	60	1000000	153579	329116	174731	66545	38228	31542	27577	23984	20702	11286	26	32	2	76	50	6595	10426	8667	4212	7454	4436	3367	2995	0	15	17	0	1
4x1	70	1000000	120836	286378	166509	68975	40752	34156	30379	28766	25007	13458	38	29	0	69	60	8399	13400	11144	5541	10028	5693	4512	4065	0	26	23	0	0
4x1	80	1000000	96463	246036	154489	68031	41179	35491	32094	31077	27908	15193	49	40	0	74	63	9355	15145	13081	6479	11943	6718	5335	5007	0	25	25	1	1
4x1	90	1000000	77566	212347	139600	64620	40407	35170	32104	32681	29443	15695	34	41	2	64	67	9765	16692	14722	7206	13160	7450	6107	5606	0	24	18	0	0
4x1	100	1000000	63379	181167	124985	60842	38178	33700	31176	32749	30071	15932	43	49	1	78	61	9998	17254	15315	7477	14147	7736	6476	5870	0	21	35	0	0
2x2	11	1000000	619961	354797	22652	1819	243	134	114	17	15	4	0	0	0	5	6	2	0	0	0	1	1	1	0	0	0	0	0	0
2x2	21	1000000	414217	456815	92054	19623	4602	4152	3755	1248	1176	620	7	4	0	15	25	124	201	156	74	151	82	54	65	0	2	3	1	0
2x2	31	1000000	297668	448573	143761	43701	13661	12910	12482	6172	5802	3073	17	16	0	38	56	844	1533	1393	659	1229	697	545	519	0	5	4	0	0
2x2	41	1000000	222849	408408	167596	61671	23073	22158	21480	13524	13112	6745	24	27	1	49	77	2210	3983	3826	1914	3712	1932	1758	1636	0	9	14	1	1
2x2	51	1000000	171255	358957	173528	71681	30060	29353	28498	20880	20128	10350	43	29	1	68	78	3841	7284	6979	3421	6528	3551	3263	3121	0	19	17	1	1
2x2	61	1000000	133430	311016	169569	75575	34578	33554	33131	26467	25643	13204	35	46	1	66	77	5373	10077	10128	4983	9715	4969	4766	4550	2	20	22	2	0
2x2	71	1000000	105675	267298	158342	75516	36523	35598	34994	30501	29889	15108	40	60	0	91	63	6385	12745	12091	6231	12284	6092	5938	5733	0	19	27	1	0
2x2	81	1000000	84963	229434	145406	72571	36510	35729	35252	32391	31438	16193	45	49	0	68	89	7545	14682	13983	7059	13726	7214	6569	6644	0	22	23	0	0
2x2	91	1000000	68536	195538	130691	67881	35740	34869	34256	33026	32631	16621	47	50	0	71	78	7856	15329	15308	7585	14697	7420	7323	7131	0	30	28	1	0
2x2	101	1000000	55483	167246	115877	62549	33670	33017	32292	32762	31949	16325	40	32	0	63	61	8012	16076	15439	7824	15307	7909	7526	7262	0	29	30	0	1